Detection and Study of the 2.22 MeV Emission Line in the Sun Deuterium Formation Process

Omar Alejandro Lezama Gallegos

División de Ciencias e Ingenierías

Campus León

Universidad de Guanajuato

A thesis submitted in partial fulfillment for the degree of

Master in Physics

Thesis advisor: Dr. Julián Félix Valdez

September 18, 2023

Once again, to my family

Abstract

The formation of deuterium in the Sun is one of the events that take place all the time as a result of various processes. In particular, the fusion of a neutron with a hydrogen atom nucleus (proton) results in the creation of a deuterium atom nucleus and the emission of a gamma ray with a very characteristic energy of 2.22 MeV. By detecting these gamma rays on Earth we can infer that the deuterium was produced in the Sun and thus obtain direct information about its production in this source.

We have planned, designed, simulated - in GEANT4 -, constructed and characterized a gamma ray detector to study this 2.22 MeV line and its emission process.

According to our simulation, we can use two veto detectors (using scintillating materials) and a water-based detector to select gammas from the cosmic ray fluxes, taking into account specific materials and their finishing; constraints in coincidence events, flight times, spatial and angular distributions and some specific properties of the produced light by the incidence of different primary sources.

We concluded that we had detected the 2.22 MeV gamma ray emission line, considering the agreement between the results of the Monte Carlo simulation and those of the direct measurement in the laboratory with our original detector.

Keywords: Deuterium, gamma ray, detection, simulation, photons

Acknowledgments

Once again, I want to first thank my parents for their unconditional love and the support they have always given me; for showing me every day how to be a better person and for being my greatest inspiration, now more than ever. Also to my beloved siblings, much of what I am and have achieved has been only because of you, I always carry with me your enthusiasm and warmth. And, of course, Mara, we could never have made it through the pandemic without you, we all owe you.

I am especially grateful to my advisor, Dr. Julian Felix for having thought of me for the realization of this project, for the weekly talks, the suggested references, for his advice in the congresses, seminars and presentations. I also thank the members of the evaluation committee, whom I deeply admire, for agreeing to be part of this final stage of my work. Your time and advice are invaluable.

I would like to express my most sincere gratitude to my friend Mimí Moreno, your support and accompaniment during this journey were the engines both to advance and to enjoy this path we chose, I appreciate the time we shared and all the talks we had. Special mentions to Jaimo, Jarona, Álvaro, Diego and Yeyo for being my greatest tokens of friendship after so many years.

Finally, I can't find the words to thank Ro for giving me the last push I needed to finish my project. This time we have shared has been the most valuable thing in my life and I trust that the best is yet to come, I love you.

Contents

List of Figures

List of Tables

Chapter 1

Introduction

This document is a compendium of the Master in Physics degree thesis work developed in the Elementary Particles Laboratory of the División de Ciencias e Ingenierías of the University of Guanajuato [1]. This work is dedicated to the study of the interactions of cosmic rays with matter, in order to build a gamma ray detector, with which we will measure the flux of different particles but we will have enough evidence to separate the corresponding flux of gamma rays with very characteristic energy.

This work has three main parts:

Firstly, the planning and design of the gamma ray detector to base the simulation and construction of the detector.

Secondly, the simulation of the proposed experimental setup in which we will study the properties of the particles produced, by the passage of primary particles, to make sure that this detector will work according with our purposes, and study the phasespace where the particles are produced with higher probabilty.

Thirdly, the construction of the experimental setup and the measurement of the gamma rays flux to compare with the results of the simulation and the previous studies carried out by other laboratories.

The basic concepts for understanding this work and its results are explained in Chapter 2, where we talk about cosmic rays, gamma rays, and gamma ray detection techniques. We also talk about solar activity, nuclear fusion, and the results of nuclear fusion processes in the Sun.

In Chapter 3 we dedicate ourselves to explaining each one of the required components of the experimental system. We show the designs we made before simulating and building the entire experimental setup. We specify the materials, sizes, and functions of each part of the detector.

In Chapter 4 we present all the information related to the simulation, this is one of the two most important chapters in the whole thesis. We start with an explanation

of Geant4, the simulation software we used; then we talk about the libraries and general features of each simulation we made to introduce our preliminary test, in which we obtained our first results about the materials we were going to use to build the experimental setup. Once we are done with this preliminary part, we will present the final version of the simulation, in which we simulate the whole experimental setup taking into account sizes, materials, primary incident particles, and different criteria to study the properties of the produced particles due to the interaction of the primary particles with the detection media. We present the simulation results, which we will directly compare with the measurement results obtained in the laboratory using the constructed experimental setup. Thus, this section is a precursor to the construction of the experimental setup but it is also analogous in the sense that the final result of the measurements we perform on the software will be directly comparable to those in the laboratory.

In Chapter 5 we detail the entire construction process including the individual detectors, power sources, data acquisition system, and the final considerations for the assembling of the entire experimental setup. We show photographs of each part of the experimental setup at different stages of the construction.

In Chapter 6 we show the results of the tests we carried out to make sure that each part of the experimental setup was working properly. We show photographs of the characteristic signals produced in the PMT by the passage of cosmic rays, we show pictures of the different configurations of the experimental setup during the tests. This is the chapter before the results, so it was very important to do the right tests to make sure that the signals we detected were due to the passage of cosmic rays and not from other sources. We also present here the result of the characterization process.

In the Chapter 7 we briefly explain how we can measure the total particle fluxes in the laboratory considering the results of the simulation. The main goal of this chapter is to explain how we have partially calibrated the spherical detector, so that we can verify that the detected signals are due to photons produced inside of the sphere and we can relate the electrical amplitudes of the PMT signals to the number of photons that produced the signal.

In Chapter 8 we present the results obtained from the experimental setup. We explain the conditions under which the data were taken, the time of data collection, the correlation of the experimental setup with the results of the simulation, and, finally, the direct comparison between the results of the simulation and the experimental setup we constructed.

In Chapter 9 we present a discussion of the conclusions drawn from the data analysis of the results in Chapter 8, we explain the correlation between the measurement

we made in the laboratory and the results of the simulation of the experimental setup. Here is where we present all the evidence we have gathered to conclude that we have detected 2.22 MeV gamma rays and that this radiation comes from the Sun.

In Appendix A.1 we show the relevant technical details of the scintillator materials we used in our detectors.

In Appendix A.2 we summarize the main features of the Photomultiplier Tubes (PMTs) we used to detect the produced photons in the experimental setup.

In the Appendix A.3 we explain how we measure the errors of each of the measurements reported in this work.

In the Appendix A.4 we give summary and the links to the data sheets of each of the voltage sources used.

In Appendix A.5 we detail the characteristics and configuration of the oscilloscope we used and the main features of other measurement instruments.

Chapter 2

Fundamental Concepts

In this chapter, we discuss the minimum concepts necessary to understand this work, cosmic rays and gamma rays, their detection methods, the gamma ray production process, and the coincidence validation method to select events of interest.

2.1 Cosmic Rays

High-energy particles, known as cosmic rays, are constantly hitting the Earth. They have direct information from sources very distant from Earth, so we make observations to study them and understand all the information related to their production, propagation, and their sources. [2].

Cosmic rays are electrically charged or electrically neutral, they originate in outer space and travel close to the speed of light; about 89% of the nuclei are hydrogen (protons), 10% are helium nuclei and about 1% are heavier nuclei [3]; there are also photons of diferent wavelength, neutrinos, and perhaps unknown particles.

Heavier elements are also included in Cosmic Rays, but they are only produced in violent conditions such as supernovae.

We have classified cosmic rays into three types:

- **Primary:** those that are accelerated by astrophysical sources.
- **Secondary:** those that are the result of the interaction of the primaries with interstellar gases.
- **Tertiary**: those that are produced by the interaction of secondary cosmic rays with the atmosphere, and these are the ones that reach the Earth's surface in abundance [4].

In Figure 2.1 we show a way to illustrate the production of secondary particles formed by the interaction of primary cosmic rays with the particles in the atmosphere, reaching the Earth's surface.

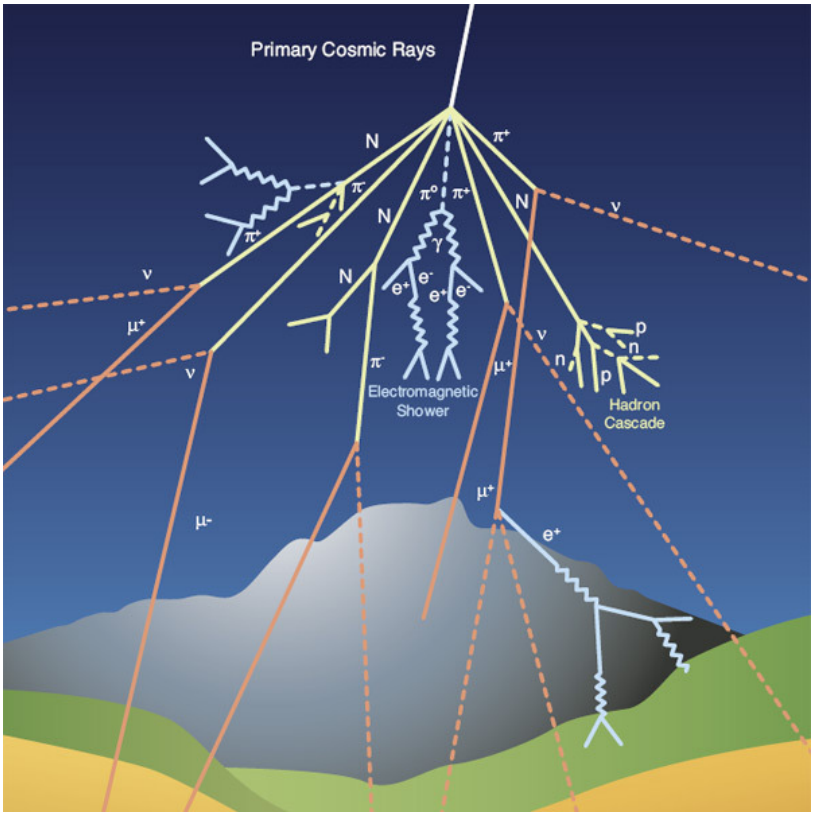

Figure 2.1: Secondary particles production from primary cosmic rays. [5].

Cosmic rays come from outside the solar system, except for particles associated with solar flares and CMEs (Coronal Mass Ejections), which are also uncharged particles. As mentioned earlier, cosmic rays are electrically charged, so their paths can be deflected by magnetic and electric fields. By the time these particles reach Earth they have already been deflected by the galactic, solar system and Earth magnetic fields [6]. For those that have no electric charge, the path to Earth is straightforward, like photons and neutrinos.

Pions are electrically charged particles produced by the collision of cosmic rays with atomic nuclei in the Earth atmosphere. Pions can decay into muons, which are the most abundant electrically charged particles at sea level on Earth, so we have a high probability that the particles detected in the laboratory are mostly muons[4]. Muons are produced in the atmosphere and lose about 2 GeV through ionization before reaching the Earth's surface. Like many fundamental particles, muons do not

interact strongly with matter, but as they pass through matter they they leave a trace of energy that we can detect [5].

In Figure 2.2 we show the cosmic ray flux as a function of energy, including the flux of high-energy and low-energy cosmic rays; and the flux of extra-galactic cosmic rays. High-energy cosmic rays are produced only under violent conditions and occur only once every few years, while low energy rays have a greater flux measured on Earth.

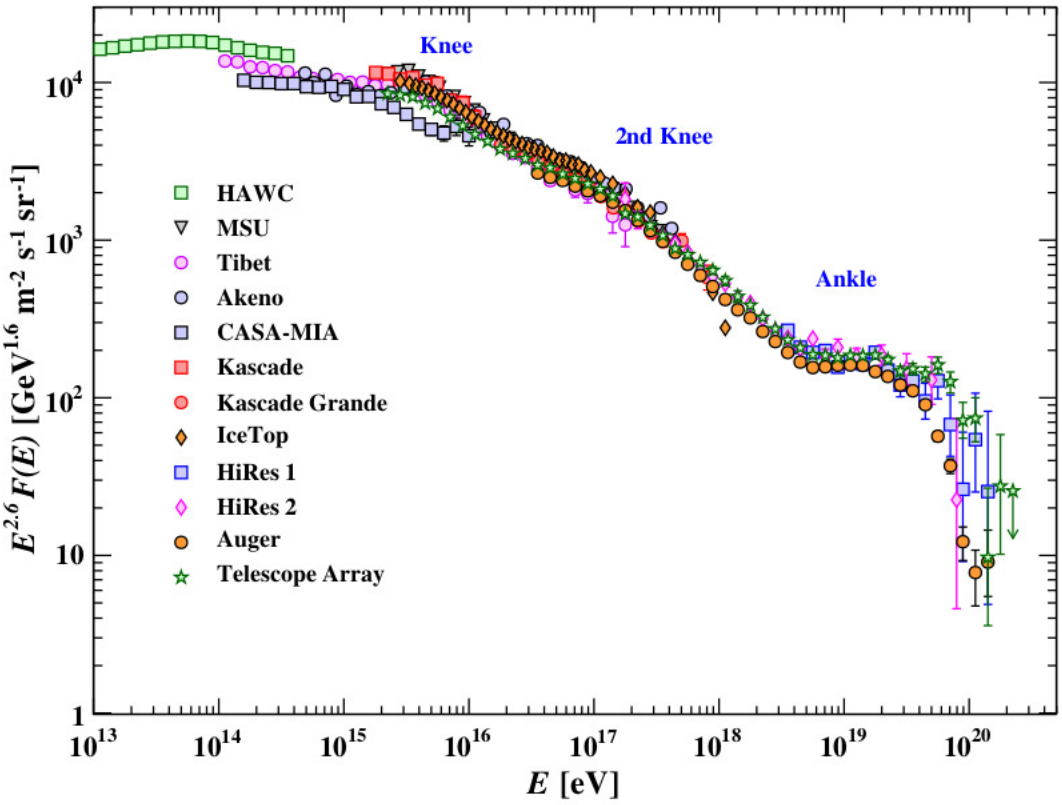

Figure 2.2: Cosmic ray spectra measured on Earth [4].

The study of cosmic rays is fundamental for obtaining information about their origin and composition. Depending on what we are studying we can measure different physical properties of the cosmic rays such as their flux as a function of altitude, latitude, and longitude; the average lifetime of the particles, the time of flight, and even the energies of the incident particles in order to classify them and characterize them for different purposes.

Now that we know the general properties of the cosmic rays, we need to explain now how we can use these properties to detect the deposited energy of these particles in matter.

2.1.1 Cosmic Ray Detection

Today there are only two types of cosmic ray detection, ion detection, and photon detection. Ultimately, we use PhotoMultiplier Tubes (PMTs) to turn photon detection into ion detection, so, that for each photon, we release an electron (electrically negative ion), which we then amplify to measurable levels with conventional instruments.

Ion Detection

This method consists on using the energy deposited by the particles in the materials to ionize them. The number of ions produced depends on the material and these ions are attracted to collectors by applying an intense electric field.

Gases or liquids are usually used for detection, but we have concluded that we can also use metals to detect cosmic rays. In Figure 2.3 it is possible to observe the ionization energies of different materials. As we can see, using metals for cosmic ray detection has some advantages, including that their ionization energy is lower than that of noble gases, they are easier to manipulate, and they require less maintenance than liquids and gases,

In Figure 2.4 we can see all the components we need to detect ions. It is called an ionization detector because the incident particles ionize the material and the released electrons are pulled by the electric field towards one of the collectors, these electrons are stored in a capacitor and released through an electrical resistance connected to the ground, which is where we measure the electrical signal. The other collector is connected to the ground through a resistor to compensate for the electrons drawn to the collector, so the material becomes electrically neutral again until a new particle hits it and the previous process is repeated. In the block diagram of Figure 2.4 we summarizes this process.

Photon Detection

This is the type of detector we have used in this work.

In this type of detector, photons are the detection channel. Two main components are required, a scintillator material and a photomultiplier. When a particle passes

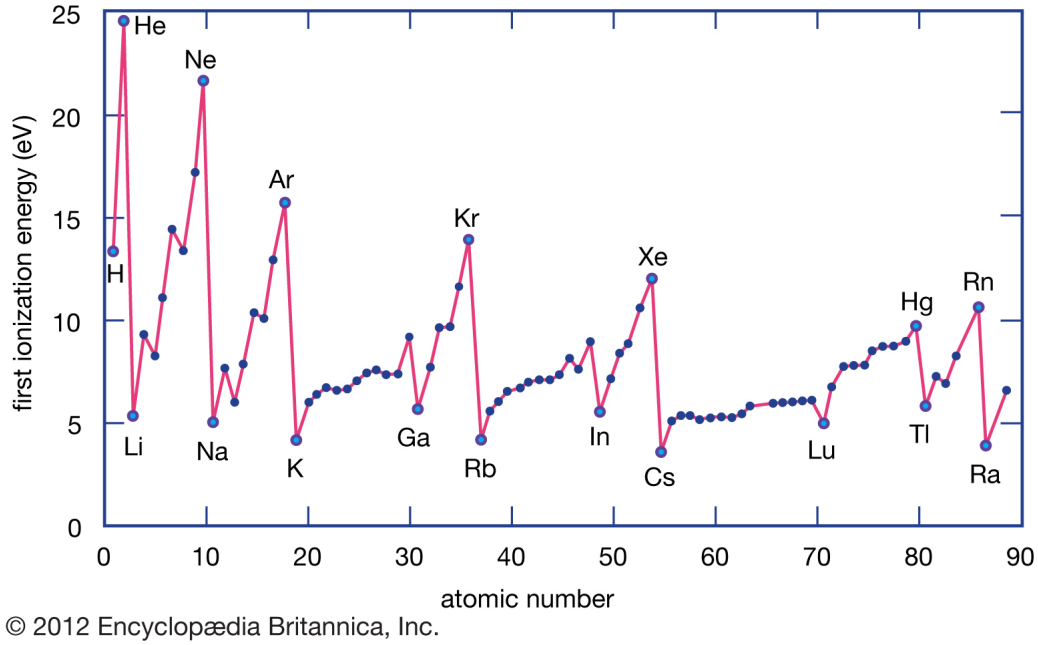

Figure 2.3: Ionization energy for different elements [8].

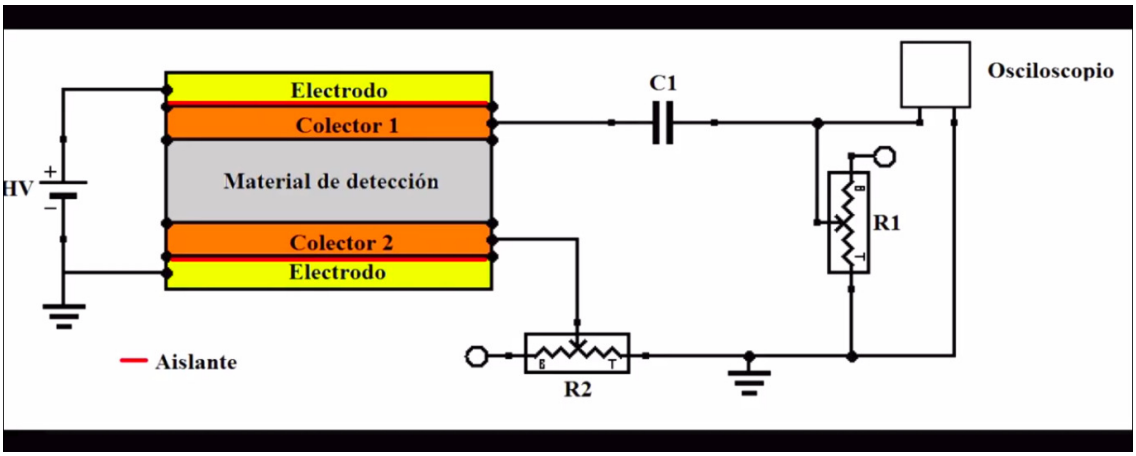

Figure 2.4: Block diagram of the ionization radiation detection method [9].

through a scintillator material it deposits energy in it, the deposited energy is released by photons, returning the scintillator material to its initial state. The photons emitted by the scintillator plastic are collected by a PMT.

There are different types of photomultipliers that vary in the range of wavelengths they detect and the effectiveness of the detections, i.e. they detect certain wavelengths better than others. Similarly, scintillating materials vary according to the wavelengths they emit. Both materials have different specifications depending on the manufac-

turer, such as signal rise time, signal fall time, response time, etc.

It is important to isolate the scintillator material from natural light to avoid photon production from sources other than cosmic rays. This is the most convenient method to perform because it requires fewer components than ion detection, and the amount of available scintillation materials is huge. The main problem is to find a scintillation material and a PMT with similar properties.

Coincidence Method

This is a method to validate signals in the detectors as the signal of interest, for example, cosmic rays or other signatures; in this way we validate the passage of electrically charged particles under study. We need at least two detectors to use the coincidence method proposed by Nobel laureate Walther Bothe [11].

Suppose we have 3 detectors, 2 that detect photons produced in a scintillator material (veto detectors) and one that detects photons produced in water by cosmic rays. The water-based detector will be placed between the veto detectors. We will have signals in each of the detectors, possibly due to the passage of cosmic rays. The validation condition is as follows: if within the same time window, we have a signal in the upper veto detector and we have a signal in the lower veto detector, then, we validate the signal in the water-based detector, if any. In the Table 2.1 we summarize the criteria to follow to validate by coincidences, where V_1 and V_2 are the veto detectors and D is the water-based detector. The number 1 indicates that there was a signal in the detector and 0 is the absence of a signal.

V_1	V_2	D	Out
1	1	1	1
1	1	0	0
1	0	1	0
0	1	1	0
1	0	0	0
0	1	0	0
0	0	1	0
0	0	0	0

Table 2.1: Truth table for coincidence validation for 3 detectors.

Using the same analogy we can use the coincidence method for 2 or more detectors.

As we can see, the use of the veto detectors is to confirm simultaneous signals as cosmic rays passing through. Cosmic rays deposit energy on various detection media, so we must expect to detect photons produced by this energy deposition. But we cannot wait forever to have a signal in all three detectors. This energy deposition and photon production are very fast events, so we have to set a time window to consider that these signals to be simultaneous and then, we say they were produced by the same source: a cosmic ray.

Cosmic rays are not the only particles that arrive on Earth by astrophysical sources, we also have electromagnetic radiation, which interacts differently than charged particles, although its energy range is very wide. We need to know the main differences between cosmic rays and electromagnetic radiation to determine their effects on matter.

2.2 Gamma Rays

Gamma rays are the most energetic form of electromagnetic radiation. The universe is essentially transparent to propagating gamma rays and since they have no electrical charge they cannot be deflected by magnetic fields.

Some of the most common forms of gamma ray production are particle-nucleon interactions, nuclear gamma ray lines, relativistic interactions (Bremsstrahlung radiation, Compton scattering, Synchrotron radiation, etc.), electron-positron annihilation, among others [12].

The sources of gamma rays are varied, they can be produced inside the solar system, where the Sun is the main source that produces them, or they can be produced outside the solar system in the so-called galactic and extragalactic sources. To date, all sources of gamma rays outside the galaxy are unknown.

2.2.1 Gamma Rays Detection

The electromagnetic spectrum of visible light has a wavelength between 400 nm and 700 nm. According to Planck's proposal, the energy of light can be expressed by the following relation

$$E = h\nu = h\frac{c}{\lambda}.$$

Since the gamma photon produced during the Deuterium formation has a characteristic energy of 2.22 MeV, we can determine that it has a wavelength of 5.6×10^{-13} m.

To observe a gamma ray, we need a detection medium to study the products of its interactions with matter. In the Elementary Particle laboratory, we only have

photomultipliers that detect light in the visible light range, so the aim is to make gamma rays produce photons in that range, from their interactions with the detection medium.

Gamma rays are detected by observing the effects they have on the matter:

- Photoelectric effect.
- Compton effect.
- Pair production.

The type of dominant interaction depends on the energy of the incident gamma ray. Figure 2.5 summarizes this information.

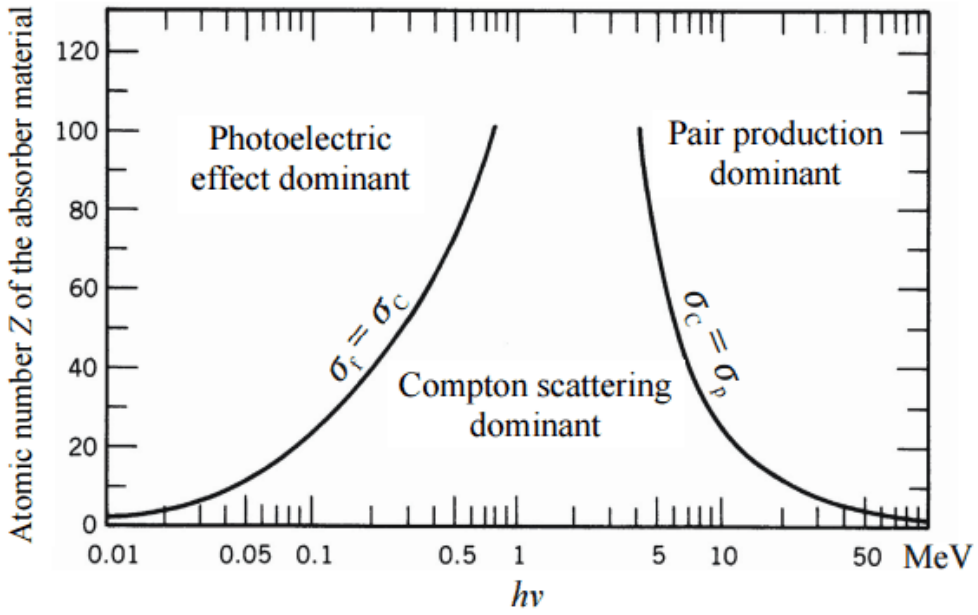

Figure 2.5: Gamma rays interaction with matter as a function of energy [13].

For our convenience, here is a small glossary of the dominant interactions.

- **Compton Effect:** When a photon collides with an electron it transfers some of its energy by scattering it, while the resulting photon has less energy [14].
- **Cherenkov Effect:** When an electrically charged particle moves through a medium faster than the speed of light in that medium, photons are emited by the medium.

  In the case of water, it is enough for a particle to travel at more than 3/4 of the speed of light (in a vacuum) for Cherenkov radiation to exist [15].

- **Bremsstrahlung radiation:** Radiation produced by free electrons that are deflected in electric fields by charged particles and by the nuclei of atoms [12].
- **Photoelectric Effect:** Occurs when a photon is completely absorbed in a collision and emits an electron to which it has transferred all its energy [16].

Some of the challenges in detecting 2.22 MeV gamma rays are

- The flux is small [17].
- They are high energy radiation, requiring the construction of very large detectors, such as Super-Kamiokande [18].
- They are dimmed by the Earth's atmosphere, so the detectors must be placed as high as possible [12].
- Because of the low flux, it's necessary to take data over long periods.

With our proposal we try to solve some of these problems, starting with the size of the detector, which is super small compared to those like the Super Kamiokande or the HAWC experiment. We have also used simple materials as media detectors, so the ease of getting them and being able to change them is also a big advantage to consider.

Regarding the flux and the altitude of the data acquisition, these are aspects to keep in mind when taking data.

2.3 Solar Activity

We know and study solar activity by observing the solar cycle, which affects the activity on the surface of the Sun. Sunspots are dark regions that appear on the solar surface and they form in places where magnetic fields are particularly strong, preventing some of the heat inside the Sun from reaching the surface. Solar activity is related to the number of sunspots, the more sunspots there are on the Sun, the more solar activity there is. [19, 20].

We need to mention two main events in the Sun: Solar Flares, and Coronal Mass Ejections (*CMEs*).

Magnetic field lines around sunspots are constantly rearranging themselves, causing an explosion of energy known as a solar flare. A **solar flare** is the release of energy and particles (electrically charged and electrically uncharged) into space, if this radiation reaches the Earth with great intensity it can even interfere with the telecommunications of the planet [20]. On the other hand, (*CMEs*) are the ejection

of large amounts of plasma and magnetic field from the solar corona. When a solar flare occurs we can't immediately tell if it was a *CME*, but by monitoring the flow of protons, electrons, and other particles we can determine if a *CME* has occurred and if it is headed toward Earth [21].
Since the particles emitted during a solar flare or a *CME* are electrically charged particles, not all of them reach the Earth because the Earth's magnetic field deflects them in the direction of the magnetic tail(see Fig.2.6). However, the magnetic field cannot deflect all of them, as the magnetic field lines reorganize some particles get trapped in the magnetosphere and eventually hit the Earth's surface [22]. When solar activity is not very intense, the amount of particles that reach the Earth is moderate, but when it is continuous and intense there is a greater amount of particles that reach the Earth's surface. Without the Earth's magnetic field, there would be no life on Earth as we know it.

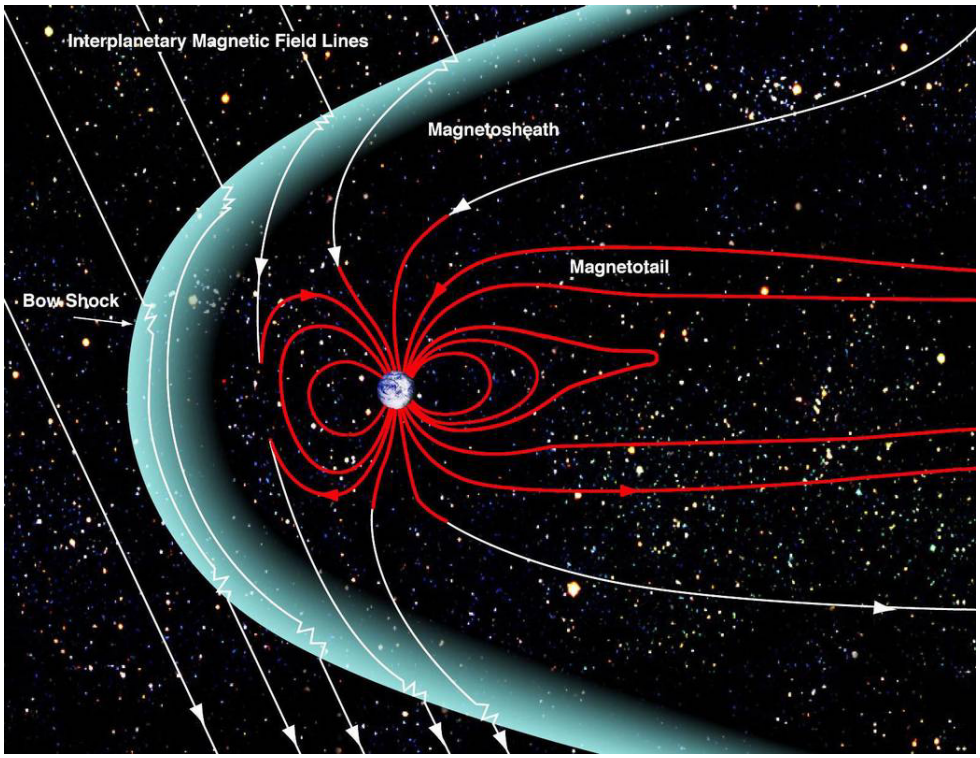

Figure 2.6: Terrestrial Magnetosphere. [22].

2.3.1 Nuclear Fusion in the Sun

Nuclear fusion is a reaction in which two light nuclei combine to form a heavier one. This process releases energy because the weight of the heavy nucleus is less than the

sum of the weights of the lighter nuclei.

For example, in the Sun, hydrogen nuclei fuse to form helium, releasing in the process a large amount of energy in the form of electromagnetic radiation that reaches the Earth's surface and is perceived as light and heat [23].

For a fusion reaction to occur, it is necessary to achieve high levels of energy that allow the nuclei to approach each other at very short distances, where the force of nuclear attraction overcomes the forces of electrostatic repulsion, in the case of equal charges.

Essentially, there are four requirements for nuclear fusion reaction to occur.

1. **High temperatures:** to produce plasma, which consists of free electrons and ionized atoms.
2. **Intense electromagnetic fields:** to confine and control the plasma at high temperatures.
3. **Strong gravitational field:** to apply high pressure to the nuclei.
4. **High plasma density:** so that the nuclei are close together, leading to fusion reactions.

2.4 Deuterium

Neutron production in the Sun is as follows

$$p^+ + e^- \Longrightarrow n + \nu_e$$

The detection of the neutrino associated with the electron is evidence that this reaction took place in the Sun.

So, these neutrons can

1. Escape from the sun.
2. Decay into other particles.
3. Interact in nuclear collisions.
4. **Be captured in Hydrogen or Helium.**

The capture of a neutron by Hydrogen produces a gamma ray of characteristic energy: 2.22 MeV [24].

The emission process of this gamma ray is

$$n + p \Longrightarrow D + \gamma$$

where γ is a 2.22 MeV gamma ray.

As we can see in Figure 2.5, for this 2.22 MeV gamma ray the main form of interaction is the Compton effect, so the visible light production from gamma rays is as shown in Figure 2.7.

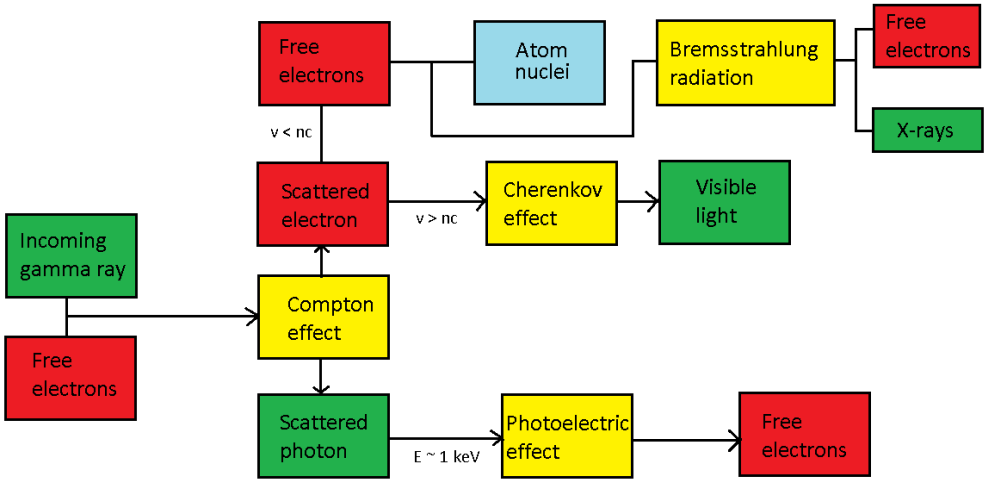

Figure 2.7: Production of visible light by the Compton effect due to the interaction between a gamma ray and free electrons.

2.5 Previous works on 2.22 MeV gamma rays detection

It is necessary to know previous works related to ours. With this, we can know what has been done, what is left to do, different techniques used, and maybe, read about different considerations to have in case we haven't considered them yet.

There are not that many papers related to the detection of this specific line emission of 2.22 MeV gamma rays. Also, most of the literature is old, so we will discuss each paper from oldest to newest.

Limit on the Continuous Solar Flux of the 2.22-MeV Neutron-Proton Capture Gamma Ray (1967)

They are one of the few to report a measured value for the upper limit on the continuous flux of 2.22 MeV gamma rays, which is

$$Flux = 0.005 \frac{photon}{cm^2 s}.$$

The value was obtained by measuring during two different phases of the solar cycle, one in 1962 (measured from the Ranger-3 experiment) and another one in 1967 (the one we describe in this section).

They used a 3 in. $\times$ 3 in. gamma ray spectrometer, using CsI(Tl) as detector medium [17].

Interplanetary particle observations associated with solar flare gamma-ray line emission (1981)

Their work consisted of evaluating the total number of energetic particles that must have interacted in the sun to produce the observed gamma rays produced during the solar flare on June 7 (1980).

The data they analyzed were taken from observations made by the Solar Maximum Mission (SMM) spacecraft [25].

A High-Resolution Measurement of the 2.223 MeV Neutron Capture Line in a Solar Flare (1982)

They analyzed the 2.223 MeV with high resolution, and identified a line feature of 2.2248 ± 0.0010 MeV.

Using the HEAO 3 high-resolution gamma ray spectrometer they analyzed the 40 seconds solar flare that occurred on 1979 November 9. The experimental setup consists of four high-resolution germanium detectors and five CSI shield detectors, covering an energy range from 100 KeV to above 5 MeV, where the 2.223 emission line is included.
The flux they measured, 130 seconds after the start of the flare, was

$$Flux = 0.29 \pm 0.07 \frac{photons}{cm^2 s}.$$

They were also clear when comparing the production models and the quantitative data from the observations [26].

The Time History of 2.22 Mev Line Emission in Solar Flares (1983)

The authors studied the time dependence of 2.22 MeV line emission using observations from the Solar Maximum Mission (SMM) gamma ray spectrometer.

Specifically, they analyzed data taken from the June 3 (1982) solar flare .

Their goals were to determine a decay time constant for the production of 2.22 MeV gamma rays to derive the density at which neutrons are captured, and to estimate the ^{3}He/H ratio [24].

Ratios of the Fluence of 2.22 MeV Gamma-Ray Line to the Fluence of 4.44 MeV Gamma-Ray Line in Solar Flares (1985)

Using observations from the Hinotori satellite in April 1981 and June 1982, they measured the ratio of 2.22 MeV gamma rays to 4.44 MeV gamma rays.

The 2.22 MeV line results from neutron capture on protons, the 4.44 MeV line results from the nuclear de-excitation of carbon. They present the results of measuring these ratios for disk flares and limb flares [27].

A Search for the 2.223 MeV Neutron Capture Gamma-Ray line from the Directions of Cygnus and the Galactic Center (1991)

The authors used data collected by the Gamma Ray Spectrometer (GRS) of the Solar Maximum Mission between 1980 and 1989 to find evidence for the 2.22 MeV gamma ray emission line. Specifically, when the black hole candidates Cygnus X-l and the Galactic Center were passed through the GRS aperture. This means that there was a lot of particle production during these events and the Sun is not the source of this emission line, so there are also papers where scientists considered detecting the 2.22 MeV emission line with sources outside the solar system.

When analyzing the data, they set limits on the emission line to analyze only the energy range they were interested in, due to the source they are studying, they mention that the production of this emission line depends on the strength of the gravitational field of the black hole because this will affect the number of neutrons that will scape. They also mention that the presence of a cool material will affect this production because it will affect the decay time of the neutrons, so if the capture of a proton occurs before the neutron decay we will have the expected emission line [28].

Solar Atmospheric Abundances and Energy Content in Flare-Accelerated Ions from Gamma-Ray Spectroscopy (1995)

Using data from 19 solar flares to study elemental abundances in the solar atmosphere, but only 9 of these flares had data available from the 2.22 MeV gamma ray emission line. Even though if this emission line was not their main interest, they present results on the rate between the 2.22 MeV and 4.44 MeV fluxes, because each of these emission lines is related to certain elements, so by comparing these two they could estimate the concentration of certain elements in the solar atmosphere.

They analyzed only the data from the SMM and made calculations of the fluence of different de-excitation lines [29].

Absorption of 2.22 MeV solar flare gamma-rays and determining of the solar plasma density altitude profile (1999)

This is an update of previous paper by the same authors in which they present the results of a model they created to calculate the time profile of the 2.223 MeV gamma rays produced during the solar flares, only this time they also considered the solar plasma density altitude profile.

The experimental data were taken from the 22 March (1991) solar flare by the PHEBUS instrument on the GRANAT observatory, so the authors only analyzed the recorded data in order to create a time profile for the 2.223 MeV gamma rays produced during the solar flare [30].

Detectability and characteristics of the 2.223 MeV line emission from nearby X-ray binaries (2002)

The authors present an update of a previous model to describe the production of the 2.22 MeV gamma ray emission line. This model was made to study X-ray binary systems, so they studied several binary sources and then, compared their results with those of gamma rays spectrometers.
Once again it has been made a study of the 2.22 MeV gamma rays whose sources are outside the solar system, but in this case, they correct a previous model to determine where this emission line happens and what factors can affect its production [31].

Comments on previous works

As we can see, previous works related to the detection and study of 2.223 MeV gamma rays consists of only one of two parts: modeling the flux of particles or measuring them with a detector. When they analyzed data or modeled the flux of particles, they used data collected by satellites, sometimes during solar flares, so they didn't

measure, they just analyzed.

One of the drawbacks of the literature is that it is old. This line of study had its peak around the 70s and 80s then, scientists started to lose interest. So, it would be risky to take all of this information as relevant for our work. We have to be very careful in the way we work because as a new proposal we have to consider more aspects. One time that could be considered when comparing with previous results is to consider the stage of the solar cycle at that time, it could give us a reference for comparing our results depending on the time we take our data.

The technique to detect 2.22 MeV gammas we use here is original, none of the previously mentioned papers reports it. It is based on the scattering of electrons by incident photons (2.22 MeV gammas), and in the detection of the photons produced on water by the passage of scattered high speed electrons by Cherenkov effect.

This work we present is composed of two main parts, the simulation of the detector we propose and then, the measurement of the particles using the detector we constructed in the laboratory, so we have simulation and laboratory results to compare and make sure we understand the way particles interact with matter and so, we can detect these gamma rays we are looking for.

This proposal that we are making is completely new, so we need to simulate it first in order to verify that it will work under certain circumstances. And then, we can construct our detector to compare the laboratory results with simulation results. If both results agree, we can conclude that we have understood the physical process we are studying.

Chapter 3

Planing and Design

Given the forms of interaction of gamma rays and charged particles with matter, we construct 3 photon detectors, 2 of them based on solid scintillator plastic material and the third on water.

In this Chapter we describe the planning of the project as well as the considerations we made to measure different parameters of interest in the experimental setup; with them we determine the best PMTs position in the detectors and the criteria to discriminate the photons produced by the passage of each of the primary particles we study.

We also show and detail the designs we made for each of the three detectors in the experimental setup as well as the structure to hold the whole system. The designs were created using the Sketch Up platform [34].
We specify dimensions and materials.

3.1 General Objectives

Our main goal is to detect the Deuterium production from the Sun in our experimental setup by detecting photons produced by the passing 2.22 MeV gamma ray. We need to implement the coincidence method to identify the detected particles as produced by muons or gamma rays. It is also necessary to think and evaluate what other conditions will be useful to distinguish the photons produced by the two primary particles, but these considerations will be explained in later Chapters.

We'll have 3 detectors: one is water-based (spherical detector) and the other two are veto detectors. The operating principle is very simple: gamma rays produce signals only in the spherical detector, while charged particles produce signals in all three detectors. This condition is our hypothesis, we need to verify this by simulating the experimental setup to then, compare it with the laboratory results.

We use the simulation software Geant4 to simulate the components of our experimental system to get information about the way particles interact with matter in order to detect them properly. We explain this part in the Chapter 4.

The experimental setup consists of a metal spherical shell filled with water (the detector medium) and two veto detectors that use a scintillator material to emit photons when a charged particle passes through. As we explained earlier, if the interactions of the particles with the water cause an electron to be shot with a speed greater than the speed of light in the medium, then Cherenkov photons will be produced.

Each detector will have at least one Photomultiplier Tube (PMT) like the one shown in Fig. 3.1. This device has a photon detection range between 270 nm and 650 nm, with its detection peak at 350 nm (purple color). In the simulation, it is important to define each one of the optical and electrical properties of the materials used, such as the refractive index, surface finish, density, scintillation rate, etc. Incomplete definition of these properties can lead to poor execution of the physical libraries, resulting in simulation results that do not to match laboratory observations.

Figure 3.1: Photomultiplier Tube (PMT) used in the experimental setup.

We also use the design software SketchUp to draw each one of the components of the experimental setup with their corresponding dimensions.

3.2 Experimental system components

The elements of the experimental setup are the following:

- **Spherical Detector**
  - Steel Sphere
  - Water
  - 1 valve

  - At least 1 PMT

- **Veto Detector**
  - Aluminum box
  - Scintillator material
  - PMT

- **Aluminum Structure**

We explain the design of each one of these components in detail.

3.3 Veto Detectors

The 2 veto detectors will be used to distinguish the signals produced by the passing of charged particles (such as muons) from the signals produced by the passing of neutral charged particles (such as gamma rays). We will use two veto detectors, one above and one below the spherical detector.

Each side of the veto detectors measures 34 cm and their height is 0.5 cm. Each box of the veto detectors has a base, a lid, and 4 pieces that make up the side walls of the detector. The lid and the base measure 34 cm x 34 cm and are 1 mm thickness. 2 of the 4 side panels are 34 cm x 2 cm, and the other two are 30 cm x 2 cm. Both types of side panels are 3.4 mm wide.

There are evenly spaced perforations along the edge of the lid and base, evenly spaced for a total of 20 evenly spaced holes. The long side panels have 6 holes each, while the short side panels have only 4 holes each. When assembled, these 4 side panels will cover the edge of the lid and base, and these holes will be used to secure the pieces with screws.

In Figure 3.2a we appreciate the bottom view of the veto detector, while in Figure 3.2b we observe the top view of this detector. The only difference is the hole in the lid where we will place the 16 cm long PMT. The hole for the PMT has a diameter of 36 mm.
In Figure 3.2c we show the assembled veto detector and its coupled PMT.

To attach the PMT to the veto we will use a support like the one in Figure 3.3. These parts are 3D printed and have a height of 5.5 cm. The base is 0.5 cm high and has a diameter of 7.6 cm. The perforation on the side of the cylinder is for a strap to hold the PMT to the support. The inner diameter of the cylinder is 36 mm, we considered a 1 mm advantage for a good fit of the PMT to this piece. The walls of the support are 0.5 cm wide.

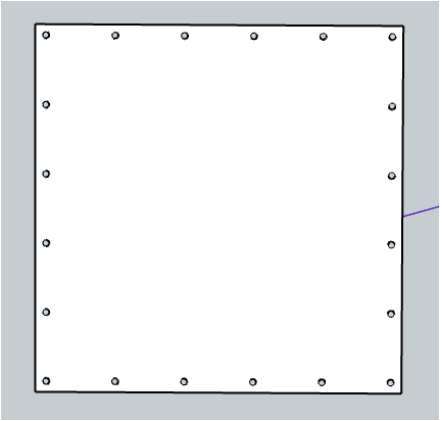

(a) Bottom view.

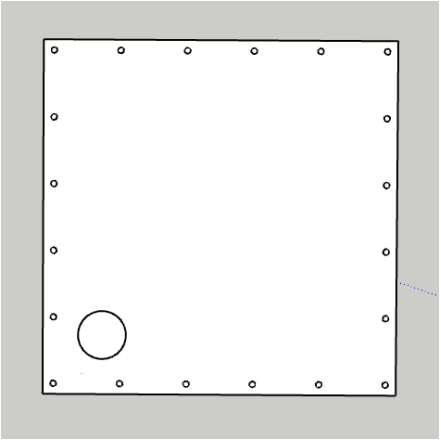

(b) Top view.

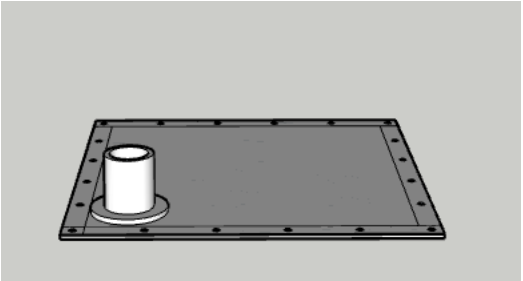

(c) Veto with PMT support.

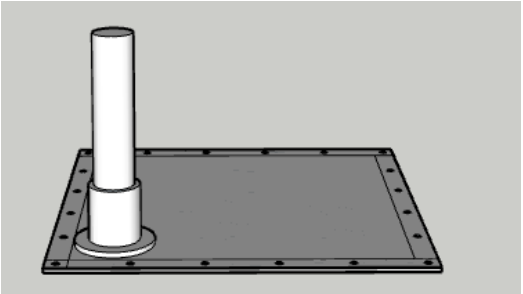

(d) Veto with coupled PMT.

Figure 3.2: Veto detector design.

3.4 Spherical Detector

This detector uses water as the detection medium, the sphere is filled with water through the valve at the top. This detector will be used in conjunction with the vetoes to distinguish the photons produced by charged particles from those produced by gamma rays.

The spherical detector has a diameter of 30 cm and the cross-section of the PMTs has a circumference of 35 mm diameter.

In Figure 3.4a we see the top view of the hemisphere, which has a square frame made of 4 aluminum rods, each 30 cm long. This frame is used to attach the sphere to the main aluminum structure.

Using two pieces like the ones in Figure 3.4b we can form the whole sphere (see Figure 3.4c), so we need to weld both hemispheres and press both frames together

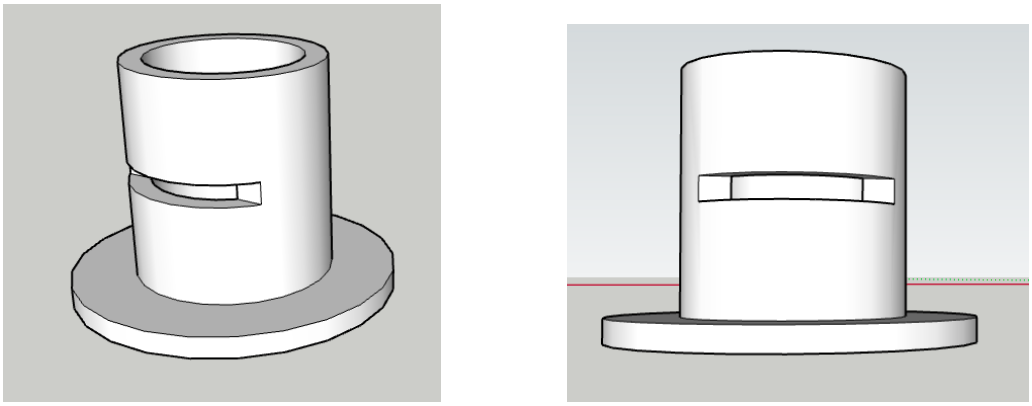

(a) (b)

Figure 3.3: Design of the support to fix the PMT to the veto.

join both parts.

The coupling of the PMT to the sphere is done via supports like the one in Figure 3.4d. The outer diameter is 95 mm and the pieces have an approximate height of 6 cm. We can also see a gap in the cylinder, this one is used to hold the PMT to the support with a strap. When we make the coupling , we will cover it with aluminum tape to reduce the noise in the measurement.

Using the supports, the sphere detector will look like in Figure 3.5. With the aluminum frame, this part will be easy to couple to the main structure. The PMTs are placed to 0^o and 45^o from the vertical axis. These parts are also 3D printed and have a width of 0.5 cm.

3.5 Aluminum Structure

The aluminum structure will have a height of 60 cm to accommodate the two veto detectors and the sphere detector with its PMTs.

The list of materials and their dimensions is as follows:

- Four 60 cm long aluminum rods
- Eighteen 30 cm long aluminum rods.
- Four 6 cm long aluminum rods.
- Two 35.5 cm long aluminum rods.
- 6 corner pieces.

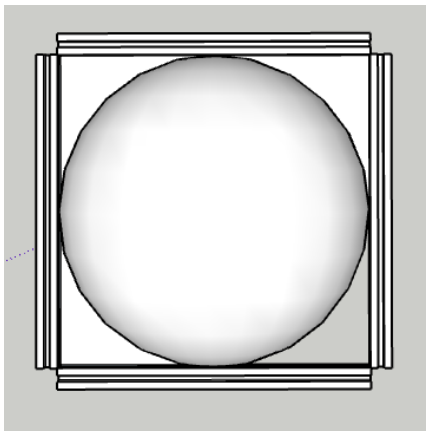

(a) Top view.

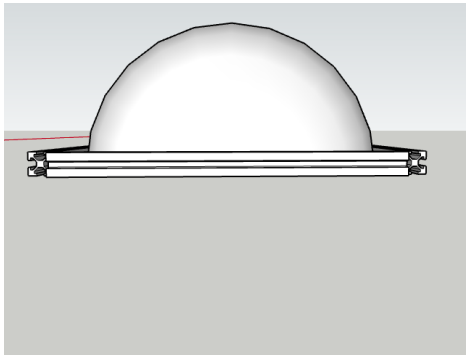

(b) Semisphere top view.

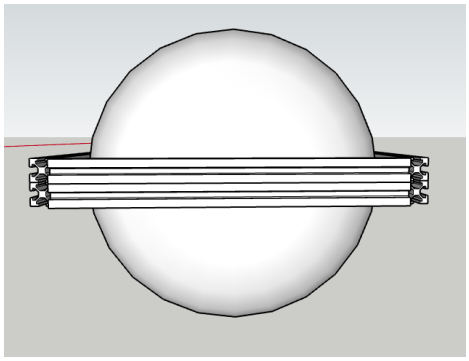

(c) Sphere frontal view.

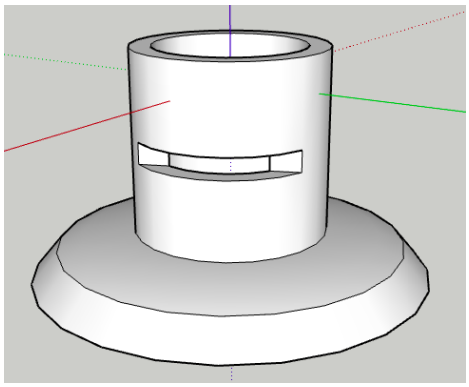

(d) PMT support.

Figure 3.4: Spherical detector design.

- 22 L-shaped connectors.

The main structure has 4 long pieces 60 cm long and 4 short pieces 30 cm long. Each side of the cross-section of these aluminum bars measures 2 cm, the shape of this piece is shown in Figure 3.6.

The connection of each one of these pieces is made in the corner with connectors. The main structure has 8 aluminum bars with 4 corner connectors and 16 L-shaped connectors, the result is observed in 3.7a.

At the top and bottom of the structure, we place the veto detectors with their PMTs pointing inside the structure, in this way, we limit the height of the experimental setup, which is about 61 cm including the vetoes. With the vetoes added, the design looks like in Figure 3.7b.

Now we add the spherical detector, it has a metal frame to fit into the main structure. The sphere is made up of 2 hemispheres bounded by the equator, each one of the hemispheres (top and bottom) has a metal frame made up of 30 cm long

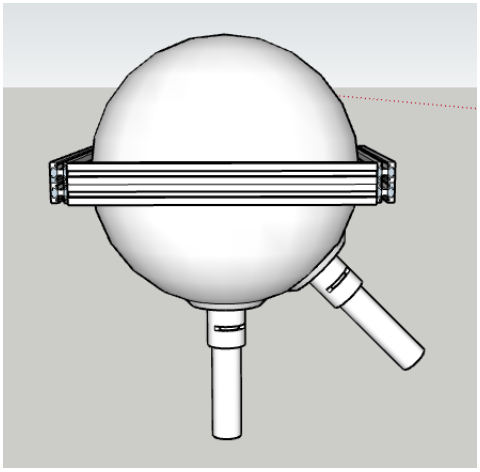

Figure 3.5: Sphere design with aluminum frame and coupled PMTs.

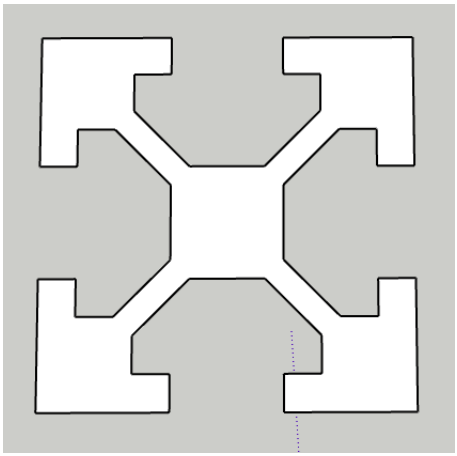

Figure 3.6: Cross section of aluminum bar.

aluminum bars. These parts are connected by L-shaped connectors. The coupling between the two hemispheres is made with screws in the metal frames. In addition, the sphere is welded at the equator. The coupling between the sphere and the main structure will also be made with L-shaped connectors. The whole experimental setup, including all 3 detectors held by the aluminum structure looks as shown in Figure 3.7c.

Finally, we note in 3.7c that one of the PMTs protrudes from the main structure, so we need to add a side structure to protect this device. Furthermore, this attached structure will hold the electronic card with which we will obtain the signals from the PMTs to then send them to the Data Acquisition System (DAS). The final design is the one shown in 3.7d.

This side structure consists of four 6 cm rods, two 30 cm rods and two 35.5 cm rods. We will also need two more corner pieces and 6 more L-shaped connectors to

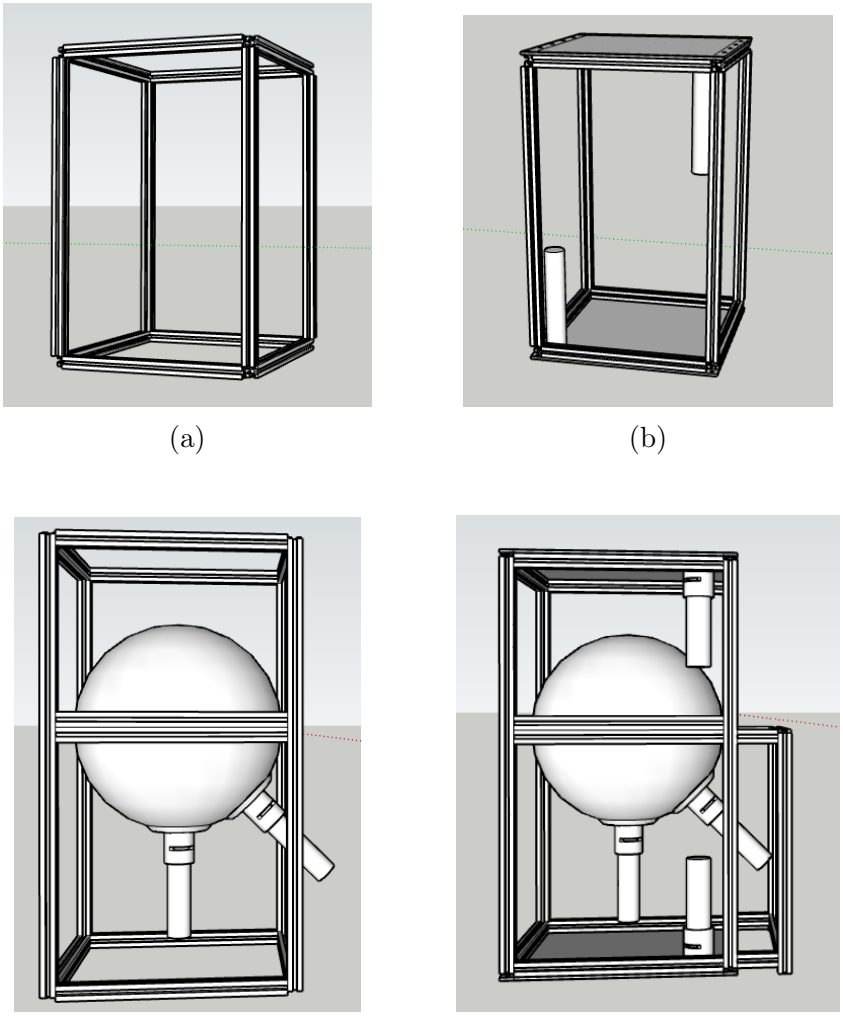

(a) (b)

(c) (d)

Figure 3.7: Main aluminum structure design.

connect this structure to the main structure.

The distance between the PMT of the sphere and the cover of the top veto is 10 cm, so we have enough space to adjust the connecting wires of these devices.

Chapter 4

Simulation

In this Chapter we will talk about the simulation of the experimental setup we made in *Geant4*, developed by CERN [35]. The results of the simulation are directly related to the construction because in this phase we verify that the considerations made were appropriate to guarantee a good performance of the experimental setup once the construction is done.

The simulation is a powerful tool to predict the dynamics of the photons produced in the detectors, since we cannot solve analytically the equations of motion of these particles in the detection medium. This allows us to decide what conditions are necessary to maximize the probability of detecting the particles we are interested in and that the materials and configurations of the experimental setup are appropriate to achieve our main goal.

All graphs were created using *Root*, developed by CERN [36].

4.1 Introduction

With the simulation, we were able to measure different properties of the optical photons produced by the interaction of the primary particles (muons and gamma rays) with the detection medium: angular and spatial distribution, energy, wavelength, polarization, etc.

Measuring the spatial and angular distributions is useful to determine the best position of the PMTs in the sphere detector to ensure the detection of as many photons as possible.

In the veto detectors, we don't have as much freedom to place the PMTs due to the dimensional constraints of the experimental setup, according to the design, the PMT bodies must face inward at the main structure, so the placement of these devices

must not interfere with the sphere detector or its PMTs.

In the simulation, we can define and modify the reflective properties of the materials covering the detection media so we can determine how convenient it is to polish the inside of the metal shells to allow more photons to reach the PMTs or if it's more convenient to define an absorbing surface to increase the detection speed.

Studying of the energy and wavelength of the photons detected is used to ensure that the photons are within the detection range of the PMTs. Another of the main utility of the simulation is to measure the detection efficiency for different veto conditions, for each of the two primary particles we are considering and for each of the different angles of the PMT around the vertical axis.

4.2 Physics Libraries

In *Geant4* we include two Physics Libraries: the Standard Electromagnetic Library and the Optical Library. These two libraries are the basic ones for performing events involving optical processes and the interaction of charged particles with matter. Next, we will discuss about the main features of these libraries and the considerations to be made when defining the physical properties of the experimental setup.

4.2.1 Standard Electromagnetic Library

This library defines the following electromagnetic processes.

- Compton Scattering.
- Photoelectric Effect.
- Rayleigh Scattering.
- Livermore Photoelectric Model.
- Coulomb Scattering.
- Ionization.
- Bremsstrahlung Radiation.

Of these processes, it is convenient to remeber the two most important ones in our simulation.

Compton Scattering occurs when a photon collides with an electron and transfers some of its energy by scattering it, while the resulting photon will now has less energy.

On the other hand, the Cherenokv effect occurs when a particle in a medium travels faster than the speed of the light in that medium, resulting in the emission of light.

Gamma rays could interact with a detection medium via the Compton effect, resulting in the scattering of an electron and the deviation of the gamma ray, which now has less energy due to the energy transfer to the scattered electron. If this electron has enough energy, it could produce photons via the Cherenkov effect. The energy trigger to produce the Cherenkov effect depends on the detection medium, in the water this energy trigger is 175 keV.

The other processes are not relevant at this time due to the energy range of the primary particles of interest.

4.2.2 Optical Library

This library defines the next set of optical processes.

- Optical Photons Absorption.
- Rayleigh Scattering.
- Mie Scattering.
- Wavelength Shifting.
- Scintillation.
- Cherenkov.

The Cherenkov effect is defined in both optical and standard electromagnetic libraries. The relevance of the rest of the optical processes depends on the optical properties of the materials we are working with in the simulation.

Is required to define the next physical properties:

- Absorption.
- Refractive Index.
- Scintillation Speed.
- Sincillation Emission Spectra.
- Scintillation Efficiency.
- Response Time.
- Production Rate.

While we have a greater amount of defined properties to each one of the materials used, the results of the simulation will be more accurate than the results we would get in the lab, so it's important to have a greater amount of available information of each of the materials.

Since we will be working with materials with scintillation properties we also need to consider the special characteristics of these materials. Scintillation materials are characterized by two-time components: one fast and one slow. The relative amplitude between the two components depends on the material, if both quantities are known we can predict the number of photons produced as a function of time

$$N = Ae^{-t/\tau_f} + Be^{-t/\tau_s}.$$

The emission of these materials are optical photons, which can be produced via the Cherenkov effect or by Compton Scattering. The forms of interaction of these photons with matter are defined in Rayleigh scattering, absorption, Mie scattering, and boundary processes.

4.3 Particle Detection Methods

In the simulation, we have two forms of particle detection, the use of which depends on the information we want to obtain from the optical photons. Both methods will be described below.

4.3.1 Tracking

This method consists of tracking each of the primary and secondary particles created in the simulation, so that it is possible to access all the information related to their creation, such as the point of creation, the direction of propagation, the energy creation, and, in the case of optical photons, their wavelengths, among others.

With this method, we can count the number of particles produced, count scattering events that have occurred, count optical photons produced by a form of production, measure detection efficiency, etc.

4.3.2 Sensitive Detectors

This method is the closest to what we have in a laboratory system, we define a geometry in the simulation and we give it the property of being a sensitive detector. With these geometries, we detect all the particles that reach it and we can extract information from them. The advantage of this method is that we can predict which

regions are more likely to detect these particles.

With this method, we can place detection planes, measure properties of the produced optical photons, implement veto conditions, and measure angular and spatial distribution, among others.

4.4 Geant 4 Classes

The simulation in Geant4 is carried out through the implementation of different text files, each one of them fulfilling, and specific function and the communication between the classes is essential to be able to measure the specific properties of interest.

In the following, we will explain the most relevant details of the classes used. First, we will talk about the global classes, those that are used in all programs, and then, some classes that are used to measure more specific properties.

Before that, it's important to mention some definitions that will be useful when explaining some features of these classes.

- **Step:** is the information of each secondary particle produced by the shot of a primary particle.
- **Event:** is known as everything that happens due to the shot of a primary particle, i.e. the set of *steps* of all secondary particles produced make up an event. Once all the interactions have ceased, the next primary particle is shot, leading to the next event.
- **Run:** is the set of all *events* produced during the execution of the program.

4.4.1 *Generator Action*

This is the class where we define the primary particles to be shot and their energy. Depending on the physics libraries used we can access a larger number of available particles. In our simulations, we have only shot muons and gamma rays. The average energy of muons at sea level on Earth is 4 GeV, while the energy of the gamma ray emitted during Deuterium production is 2.22 MeV. These are the energies at which we shot the primary particles in the simulation.

We also define the shot point of the particles, the direction of propagation, and even the properties of polarization, momentum, etc. For this simulation, we only change the identity of the particles, the direction of propagation, the point of origin, and the energy of the shot. The rest of the more specific properties are left by as they are.

4.4.2 *Construction*

This class communicates directly with the *Detector* and *Stepping* classes. Here is where we define all geometries and materials that will appear on the visual interface of Geant4.

There is a volume known as *Mother Volume*, which is the world we are working in the simulation. Inside this volume is where all the programmed events will take place, so the rest of the defined volumes will be declared inside this one. Just like the rest of the objects in the simulation, the *Mother Volume* has some properties, for example, it can be a cube of certain dimensions filled with air.

Each defined object needs a definition and 2 different types of volumes to specify its main characteristics. In the definition we choose the shape of the figure, for example, cube, sphere, cylinder, etc. The *logical volume* is the one in which we specify the material this object is made of and its location relative to the *Mother Volume*. The *physical volume* is the one in which we specify the rotation and/or displacement of the object relative to its geometric center and we declare if the volume is the *Mother Volume* or if this volume is inside the *Mother Volume*, which is the volume where all the simulation will take place.

As we have said before, it is necessary to define the physical properties of these materials, such as refractive index, reflectivity, etc. In this class is where we make all the definitions of these properties and we can also create our materials if we know their chemical formula as well as the concentration of each of the elements present.

Finally, in this class is where we define the *Scoring Volumes* and *Sensitive Detectors*. The former are used in the *Stepping* class while the latter are used in the *Detector* class. Basically, these volumes are the ones we will use to count the particles that reach them. This is like defining our PMTs in the simulation, so we will detect all photons that reach them.

4.4.3 *Action*

This class is where we implement classes that will communicate through a hierarchical level, here we also define the primary particle generator.

Basically, the communication is bottom-up between the classes *Stepping*, *Event*, and *Run*. Later, we will explain the communication of the classes in more detail.

4.4.4 *Stacking*

This class is only necessary if we are not using *Sensitive Detector* or *Scoring Volumes*, i.e. it is only used if we are working with the *Tracking* detection method. Here, each particle is assigned an ID and all its information is stored and labeled from the moment it is created. This class communicates directly with the *Stepping* class, so it is important to understand the hierarchy of the class in order to study the properties of the particles individually, per event, and for the whole run.

In the case of working with the other detection method, we can omit this class keeping in mind the hierarchical communication between classes, which we will explain in detail later.

4.4.5 *Detector*

This class has no hierarchical communication with the other classes. Here we can get all the information about the particles that have interacted with the *Sensitive Detectors*. If we don't need communication between classes, for example, to count detected particles per event of a set of events, then this is the only class we need to get information about each particle individually.

We can print in the terminal the information of interest of the detected particles (position where they were detected, energy, polarization, wavelength, momentum, etc.) or send them directly to *root* files to graph these properties.

This class is very useful and fast if we want to observe distributions of any physical property of interest, but it's not useful to measure the properties of the produced particles for each shot of primary particles (event). We can plot or print the information photon by photon but we can't distinguish the properties per event.

4.4.6 *Stepping*

This class is essentially the same as the *Detector* class with the main difference that here in *Stepping* we define *Scoring Volumes*, not *Sensitive Detectors*. The properties of an object in the simulation can be measured with both methods and the exit of the program must not change depending on the class we use.

The advantage of *Stepping* over *Detector* is when we are interested in measuring the properties of a set of particles per event and not individually. *Stepping* has direct communication with *Event*, it can send information from each particle to this superior class in such a way that at the end we will obtain the information of this set of secondary particles produced by the shot of one or more primary particles.

4.4.7 *Event*

In this class, we store all the information sent by *Stepping*, per event. Once in *Event*, we can, for example, count the total number of particles that were detected in each of the 3 detectors (in our setup) due to the shot of each primary particle.

Analogous to the communication between *Stepping* and *Event*, *Event* has the same communication with *Run*, only that in the latter we could obtain the set of information of all the particles produced by all the events in the simulation.

4.4.8 *Run*

This class stores all the information sent by *Event*, i.e. when all the events are finished is when we can access this class to decide what to do with the information of all the particles produced. For example, we can count the total number of photons detected in all the 3 detectors during the whole simulation. When running the simulation we have shot a finite number of primary particles, when all these particles are shot then we can access *Run* to measure the properties of interest from all the secondary particles.

Basically, we limit ourselves to counting the total number of photons detected per event and for the entire run of the simulation.

4.4.9 Communication between Classes

Communication between classes is as shown in the next diagram (see 4.1). The transfer of information is always from left to right. Once we are in a different hierarchy level of the classes we can't go back to a lower hierarchy level, so we must always make sure to send enough information to the higher hierarchies so that we can use it later, depending on the conditions we implement in the program.

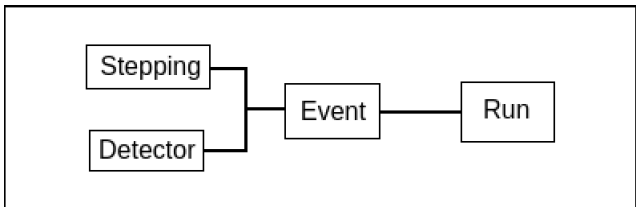

Figure 4.1: Communication between classes.

Material	Composition	Density (g/cm^3)	n
Air	O, N	0.00129	1.0
Water	H, O	1.0	1.3
Aluminum	Al	2.7	1.2
Aerogel	SiO_2, H_2O, C	0.2	1.5

Table 4.1: General properties of the materials defined in the simulation.

4.5 Experimental system

Now is time to describe each of the components within the simulation. Essentially we have three detectors, one using water as the detector medium and the other two based on scintillator material. Each detector has its detector medium, the box that contains it, and a coupled PMT. We describe the geometrical characteristics of each of these components.

Before describing the experimental setup in detail, it's important to describe the more important properties of the materials defined in the simulation. In the Table 4.1 we list these properties.

4.5.1 Water based Detector

It consists of an aluminum sphere 30 centimeters in diameter and 1 mm thick. One of the PMTs is placed in the lower part of the sphere, aligned with the vertical axis of the experimental system, i.e. it is centered in the xy plane and its geometric center is at the origin of the simulation coordinate system. The other is placed at 45° from the vertical axis.

The inside of the sphere is painted black so that the reflectance inside is 0%. The sphere is filled with pure water, which is the detector medium in which the gamma rays will interact to produce the Compton effect.

4.5.2 Scintillator material based Detector

It consists of a scintillator material of 30 cm x 30 cm x 3 mm, covered by an aluminum box. The inside of the box is polished with a reflectance of 98% so that all the photons produced are reflected in all possible directions to increase the amount of photons reaching the PMT.

Since we have two detectors of this type, one is placed above the sphere and the other is below it. The detectors are centered in the xy plane and the vertical axis one is placed at 170.5 mm and the other at - 170.5 mm.

4.6 Preliminary results

Given the considerations of the experimental setup, we are interested in knowing the properties of the photons produced by the passing of muons and gamma rays in the detection medium. To this end, we simulate different conditions to study different properties of these particles in order to determine which conditions are useful to distinguish between the two primary particles we are studying: gamma rays and muons.

In this first part, we will present the results of the simplest simulations, i.e. in order to be able to simulate the whole experimental setup it was first necessary to study different simple cases to make sure that with the planned experimental setup we will get the results we are interested in.

Later we will explain the results of the simulation of the whole experimental setup, where we have a fine simulation whose results can be directly compared with the results we obtain in the laboratory.

4.6.1 Detection Efficiency

We now present the results of the tests to measure the detection efficiency of the water-based detector. We shot 1000 primary particles (muons or gamma rays), these particles interact with the water inside the sphere and produce photons, but due to the dimensions of the PMT used, we can't detect all the photons produced, only some of them. So we measure the detection efficiency by comparing the total number of photons detected in the PMT with the total number of photons produced in all events.

Throughout this whole chapter, we will present the results of the spherical detector for the following PMT colocation angles (measured from the vertical axis): 0°, 20°, 45°, 90° y 135°. This is to determine in which region it would be more convenient to place the PMTs to be able to distinguish the photons produced by the passing of muons from those produced by the passing of gamma rays.

The first of the results in the Table 4.2, corresponds to the case where the inside of the sphere is polished in such a way that the photons are reflected, causing a greater amount of photons to reach the PMT and increasing the detection efficiency. In the case of gamma rays, we have a greater detection efficiency when the PMT is placed at 20° y 45°, a result analogous to the anti-veto condition we will explain later. Similarly, the detection efficiency of photons produced by muons is maximum when the PMT is at 45°.

Now, in the Table 4.3 we present the detection efficiency when the inside of the sphere is not polished so it doesn't reflect photons, it absorbs them all. We are inter-

Detection Efficiency		
PMT angle	Gamma	Muon
0°	1.74%	1.68%
20°	1.74%	1.78%
45°	1.74%	1.84%
90°	1.71%	1.67%
135°	1.75%	1.69%

Table 4.2: Detection efficiency of photons produced by 1000 shots of primary particles: From the total number of photons produced in all events, how many do we detect in the PMT of the spherical detector? Reflectivity: 98%.

Detection Efficiency		
PMT angle	Gamma	Muon
0°	0.104%	0.049%
20°	0.133%	0.132%
45°	0.095%	0.227%
90°	0.039%	0.020%
135°	0.028%	0.015%

Table 4.3: Detection efficiency of photons produced by 1000 shots of primary particles: From the total number of photons produced in all events, how many do we detect in the PMT of the spherical detector? Reflectivity: 0%.

ested in this case because we want to detect the trajectory of the photons produced. If the photons are reflected inside the sphere, we lose that information because the photons can be basically hit in any direction. In this case, the efficiency decreases considerably in both cases, although the detection efficiency is greater when shooting gamma rays than muons when the PMT is placed at small angles.

We need to think of other conditions we can apply to distinguish photons produced by different primary particles, but now we have an estimate of the direction in which these photons propagate.

4.6.2 Coincidence Method

Before we begin to describe these results in detail it is important to define what we mean at this moment by **coincidence**.

A coincidence is defined as the detection of a simultaneous signal in two or more detectors with a time difference. As we know, the word coincidence necessarily implies a time interval that can be as small as we want, this parameter will depend on the resolution of our experimental setup.

In this section, when we talk about coincidence we are not yet considering time. This is what we are considering for now:

We shoot one primary particle per event and we count the total number of photons detected in each of the 3 detectors. If the result of this event is the detection of a simultaneous signal produced by photons in all three detectors due to the incidence of only one primary particle, then we have a coincidence in this case. At this point, we are interested in knowing whether charged particles can produce signals in both the vetoes and the spherical detectors. In the same way, we are also interested in knowing whether or not gamma rays produce a simultaneous signal and what the characteristics of these signals are.

When we simulate the whole experimental system we will take the time constraints into account, but at this point, we don't.

Strictly speaking, we are not yet measuring coincidences yet, we are only investigating whether signals are produced in the 3 detectors by the passing of a primary particle.

Once we know the resolution of the experimental setup, we can look over time to determine if there was a coincidence or not. In the simulation we can also measure the time it took for all the secondary particles to be detected after the primary particles were shot, and then we can consider the minimum resolution we need to identify these events. We will make time considerations later.

First, we present the results of the tests with veto conditions, i.e. we have signal in both veto detectors and in the spherical detector. For each test, we shot 1000 primary particles (muons or gamma rays) and we count the total number of events validated by this condition.

We are interested in determining whether the coincidence method works to discriminate between photons produced by gamma rays and those produced by muons. The result, if we have a veto reflectance of 95% (see Table 4.4), is that out of all 1000 gamma rays events we don't have a simultaneous signal in the 3 detectors for any of the different PMT positions of the spherical detector. In the case of muons, we have a coincidence in 4 of the 5 cases considered for the position of the PMT.

If we increase the reflectance in the vetoes to 98%, we notice an increase in the number of events in which we have coincidences when shooting muons but we still have no coincidence events when shooting gamma rays.

We can observe that the optimal position to detect photons produced by the pass-

Coincidences		
PMT angle	Gamma	Muon
0°	0	55
20°	0	38
45°	0	28
90°	0	16
135°	0	7

Table 4.4: Veto condition for 1000 particle shots: For how many events do we have a simultaneous signal in all 3 detectors? Vetoes reflectance: 95%.

Coincidences		
PMT angle	Gamma	Muon
0°	0	159
20°	0	141
45°	0	134
90°	0	104
135°	0	83

Table 4.5: Veto condition for 1000 particle shots: For how many events we have a simultaneous signal in all 3 detectors? Vetoes reflectance: 98%.

ing of muons is when we place it at 45° from the vertical axis.

One last test we did was to reduce the reflectance of the vetoes to 0% to also reduce the response time of the experimental setup. Now the photons in the vetoes would no longer be reflected so we will simply detect the photons that went directly to the PMT, avoiding delay times. We show the result in Table 4.6, we know that having coincidence events when shooting muons is fundamental to increase as much as possible the reflectance inside the vetoes. In the cases where we shoot gamma rays we still do not have a coincidence event, but we already expected this.

Coincidences		
Ángulo PMT	Gamma	Muon
0°	0	0
20°	0	0
45°	0	0
90°	0	0
135°	0	0

Table 4.6: Veto condition for 1000 particle shots: For how many events do we have a simultaneous signal in all 3 detectors? Vetoes reflectance: 0%.

Anti-veto condition		
PMT angle	Gamma	Muon
0°	6.0%	50.6%
20°	6.7%	50.3%
45°	5.3%	46.9%
90°	3.1%	35.1%
135°	2.0%	33.5%

Table 4.7: Anti-veto condition detection efficiency for 1000 shots: For how many events do we detect photons only on the sphere detector but not in any of the vetoes? Vetoes reflectance: 95%

4.6.3 Anti-veto Coindition

The next case to consider is the anti-veto condition, where we only have a signal on the sphere detector but none on the vetoes. In this case, it is not necessary to consider a time constraint because we are only considering events where we detect photons on the sphere regardless of when this happens. What will be more relevant later is to determine the acceptable time range for detecting these events, taking into account the time it takes for the relativistic particle to pass through the entire experimental setup.

We will also later consider not only the number of events where this condition was validated, but also the properties of the validated photons.

Again, we shoot 1000 primary particles. In Table 4.7 we observe that this condition is optimal to detect photons produced by the passing of gamma rays when we place the PMT of the sphere at an angle of 20° or 45°. These results are for an internal reflectance of the vetoes of 95%.

The problem we have is that with this condition there is also a high efficiency of detection of photons produced by the passing of muons, so it's necessary to use more conditions together to guarantee that the photons detected correspond to the passing of gamma rays and not the passing of charged particles.

If we now increase the reflectance on the inside of the vetoes to 98%, two important things happen. The first one is that the number of events validated by this condition stays the same when we shoot gamma rays. The second one is that the number of events validated by the anti-veto condition decreases when we shoot muons, it is cut in half.

The conclusion of this and the previous section is: We can consider placing the PMT in a range between 20° and 45°, because here we validate a larger amount of events that satisfy both coincidence and anti-veto conditions. We need to increase the reflectance within the vetoes as much as possible because this not only improves the validation of coincidence events but also reduces the amount of anti-veto events vali-

Anti-veto condition		
PMT angle	Gamma	Muon
0°	6.4%	31.4%
20°	6.1%	31.1%
45°	5.8%	26.8%
90°	3.2%	20.2%
135°	2.6%	18.9%

Table 4.8: Anti-veto condition detection efficiency for 1000 shots: For how many events do we detect photons only on the sphere detector but not in any of the vetoes? Vetoes reflectance: 98%

dated when shooting muons. This latter point is crucial to being able to distinguish validated photons in events when we shoot muons and gamma rays.

4.6.4 Spatial Distribution

To know the spatial distribution of photons produced by the passing of primary particles we place a square detection plane directly under the water sphere. In previous simulations, we concluded that the placing of the detection plane will be in this position is because this is where we detect the greater amount of photons compared to the sides of the sphere.

We want to see if it's possible to distinguish between the photons produced by gamma rays and those produced by muons.

In a laboratory setup, we can't focus the gamma ray beam, they travel uniformly and randomly throughout the entire experimental system. Considering this, then we shoot 1000 gamma rays uniformly and vertically along the whole experimental setup and we observe the spatial distribution shown in Figure 4.2. We then find that we need to stay in the center or closer to this region of the detection plane to detect a greater amount of photons produced by the gamma rays passing through the detection medium.

In 3D, the spatial distribution looks like in Figure 4.3. Here the location of the regions where a high concentration of photons is detected is more visual.

Now that there is the possibility of lower energy gamma rays passing through the spherical detector, we need to know whether these particles produce photons and, if they do, what is their spatial distribution is in order to establish conditions for distinguishing them from the photons produced by the 2.22 MeV gamma rays we are interested in.

The result is that if the gamma rays have an energy of 1 MeV or less, they don't

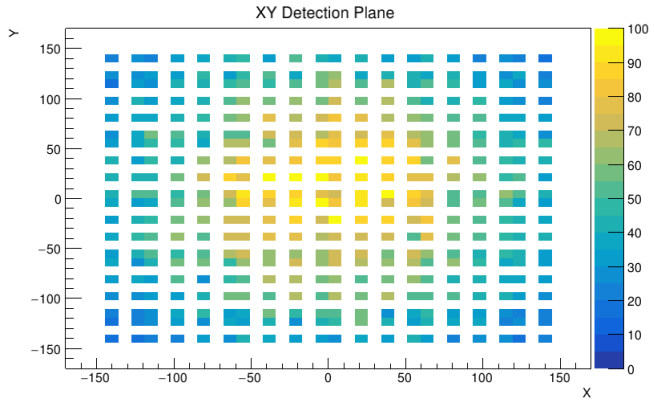

Figure 4.2: Detection plane for 1000 2.22 MeV gamma rays shot uniformly.

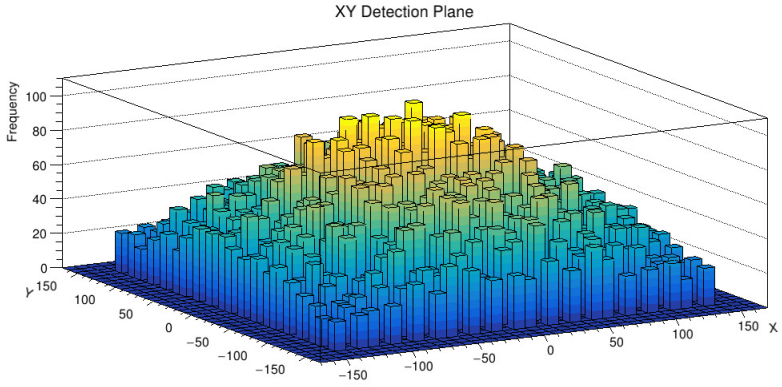

Figure 4.3: 3D detection plane for optical photons produced by 1000 2.22 MeV gamma rays shot uniformly.

produce photons inside the sphere detector due to interaction with water, and they don't produce signals on the vetoes either. So, we don't have to worry about these low-energy particles.

Now, we need to also consider the case where higher energy gamma rays pass through the experimental setup. In the simulation, we shot 1000 1 GeV gamma rays uniformly through the experimental system. In this case, photons are produced and we observe their spatial distribution in Figure 4.4. We notice that the region where there is a large concentration of photons is not in the center but in one of the corners. Given the symmetry of the experimental setup, this corner could be any of the 4 corners.

The conclusion is that if we place the PMT in the center of the detection plane, i.e. at 0° from the vertical axis, we are more likely to detect not only the photons

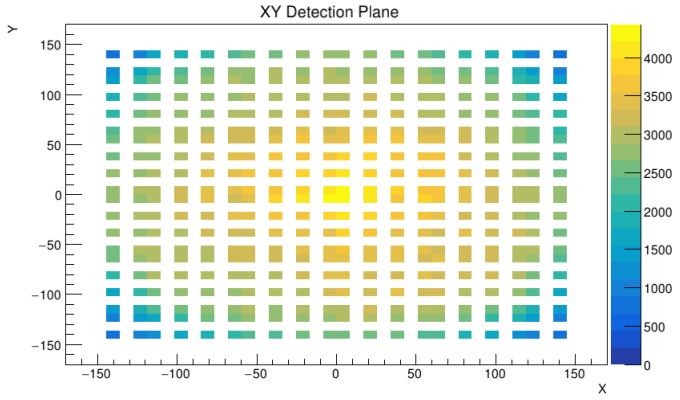

Figure 4.4: Detection plane for 1000 1 GeV gamma rays shot uniformly.

produced by gamma rays but also the photons produced by gamma rays in the energy range we are interested in.

In Figures 4.5 and 4.6 we show the spatial distribution of photons produced by the passing of 4 GeV muons in two and three dimensions, respectively. In this case, we have a well-defined spatial distribution, there is a circle whose center is on the geometric center of the detection plane and whose diameter matches the side of this plane. Not only is the number of photons greater, but they are also uniformly distributed within the formed circle. At the corners of the detection plane is where we have little photon detection in this case.

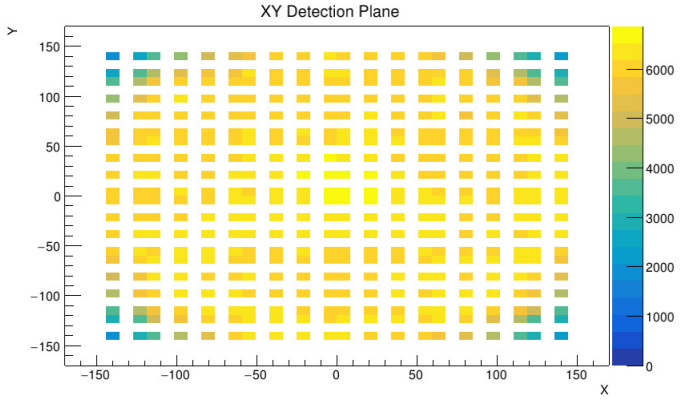

Figure 4.5: Detection plane of optical photons produced by 1000 4 GeV muons.

Given that most of the photons produced by the passage of gamma rays are detected in the center of the detection plane and we observe that we also detect a large number of photons produced by the passage of muons in this region, it is necessary to think about what conditions we should add to the experimental setup

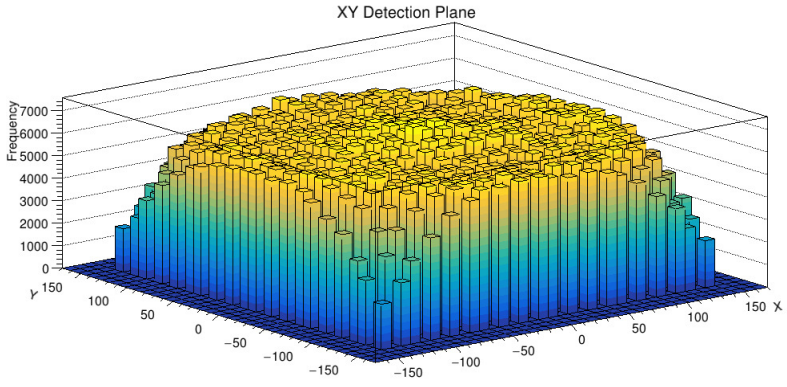

Figure 4.6: Three-dimensional detection plane of optical photons produced by 1000 4 GeV muons.

so that we can identify both sets of photons. This is what the veto detectors are for, and the use of the coincidence method is the first criterion for being able to perform this photon discrimination.

4.6.5 Angular Distribution

The placement of the PMT on the spherical detector will be with at an inclination angle relative to the geometric center of the sphere. This angle will depend on the region where there is a greater concentration of photons produced by the passing of gamma rays. In the next Figures, we show the frequency of the photons as a function of the zenith angle measured from the vertical axis. Essentially, we are showing the same information as in the spatial distribution but now we are showing it as a function of the angle from vertical at which the photons hit the detection plane.

In Figure 4.7 we show the angular distribution of the photons detected in the detection plane by the incidence of gamma rays and muons. The photons produced by the passing of gamma rays are shown in a light pink color, while the photons produced by the passing of muons are shown in blue color. The overlap of the two graphs is shown in a dark pink color. In the case of gamma rays, we observe that the peaks where more particles were detected are at small angles, there is also a higher concentration of photons at angles between 30° and 45°.

In the case of photons produced by the passing of muons, it is clear that both the number of photons and the location of the maximum detection peak (approximately 45°), it is convenient to consider this region of the PMT placement angles because we would mostly be detecting photons produced by muons and not by gamma rays, with which we would obtain physical information of these photons per event to be able to

distinguish them from those produced by the passage of gamma rays.

Let us remember that in this section we are interested in the shape of both angular distributions, but we know that the number of photons produced by the passing of muons is much greater than those produced by the passing of gamma rays.

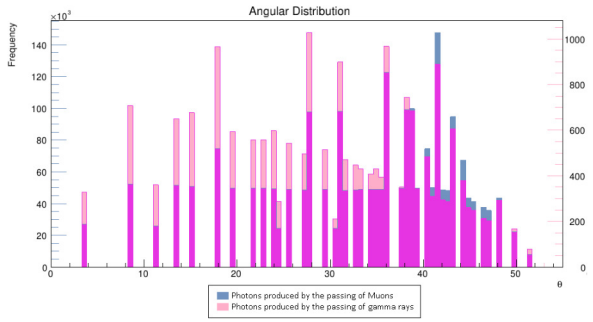

Figure 4.7: Angular distribution of photons produced by the passing of 1000 gamma rays and 1000 muons.

Again we conclude that not only because for the detection efficiency, the coincidence method, and the veto condition we have to consider the placement of the PMTs of the sphere between 0° and 45°, but also by observing these spatial and angular distributions we come to the same conclusion.

4.6.6 Wavelength Distribution

Another criterion used to distinguish between the photons produced is their wavelength distribution.

In Figure 4.8 and Figure 4.9 we show the wavelength distribution of the detected photons produced by the incidence of gamma rays and muons, respectively. Remember that in this section we are studying the properties of the photons detected in the detection plane we mentioned in the previous sections.

We can see that the only difference between the two graphs is the number of photons detected, both the wavelength range and the distribution of the graphs are the same. There is a greater number of photons detected at 300 nm and as the wavelength increases, fewer and fewer photons are detected, with a cut-off at 610 nm.

Therefore, we cannot use the wavelength property of the photons produced because both primary particles produce photons with the same properties.

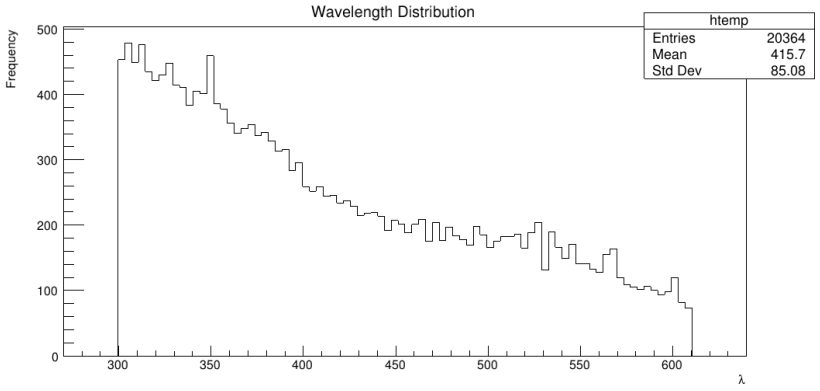

Figure 4.8: Wavelength distribution of photons produced by the passing of 1000 gamma rays.

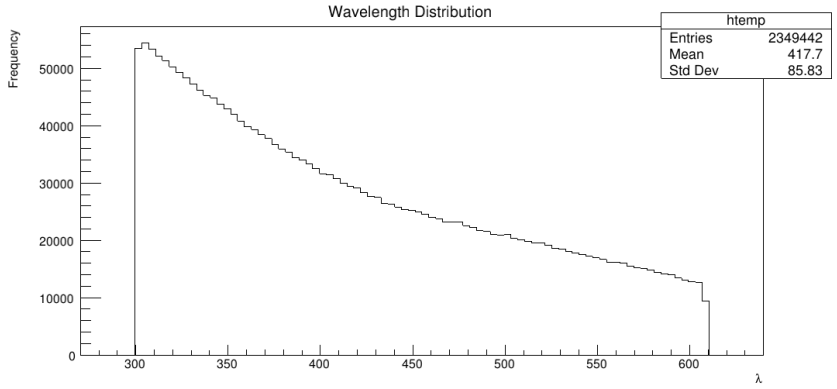

Figure 4.9: Wavelength distribution of photons produced by the passing of 1000 muons.

What we can conclude from this section is that there will be a significant difference in the intensities of the signals emitted by the PMT. The PMT converts an optical signal into an electrical signal and the intensity of this electrical signal is directly proportional to the number of photons that have passed through the optical window of this device. Then, when analyzing the data of the signals emitted by the passage of primary particles, at least two predominant regions of intensity in the signals should be evident, the one with the lowest intensity would correspond to photons produced by the passage of gamma rays while the region of higher intensity would correspond to photons produced by the passage of muons through the detection medium of the spherical detector.

4.6.7 Forms of Photon Production

From the simulation, we know that the secondary photons produced by the passage of muons and gamma rays in the water of the spherical detector are produced in two ways, either by Cherenkov radiation or by Scintillation.

We study the distribution of the wavelengths of the photons produced by each of these forms of production, this is to determine if observed differences between the characteristics of the photons produced by one form or another could constitute a criterion for identifying of the primary particle that produced them.

In this section, we study the total number of photons produced in 1000 events for each primary particle. Once we have counted all the photons, we separate them according to how they were produced and then we measure their wavelengths to observe their energy distribution.

First, we find that of the total number of photons produced during the 1000 events, most of them are produced by Cherenkov radiation and the rest by Scintillation. Specifically, we measure the following quantities:

- 1000 muon shots
  - Total photons produced : 7951952
  - Cherenkov photons produced : 6347201
  - Scintillation photons produced : 1604751
- 1000 gamma ray shots
  - Total photons produced : 98563
  - Cherenkov photons produced : 66125
  - Scintillation photons produced : 33438

In both cases, the dominant form of production is by Cherenkov radiation. When we shoot muons, about 80% of the photons are produced by this form while in the case where we shoot gamma rays, about 67% of the photons are produced by the Cherenkov effect.

First, we compare the wavelength distribution for photons produced by the Cherenkov effect. In Figures 4.10 and 4.11 we observe these distributions for photons produced by passing gamma rays and muons, respectively.

We note that both graphs follow the same distribution, photons are emitted with wavelengths between 300 nm and 610 nm, approximately, with the maximum at 300 nm and decreasing in frequency as the wavelength increases. The most significant difference is in the number of photons detected when each primary particle is shot

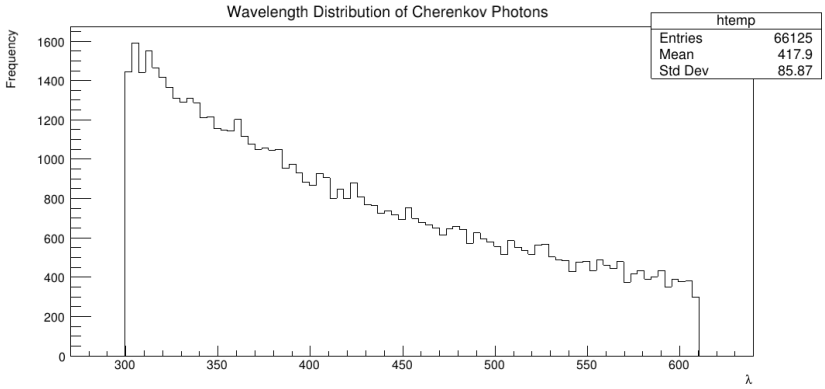

Figure 4.10: Wavelength of photons produced by Cherenkov due to the incidence of 1000 gamma rays.

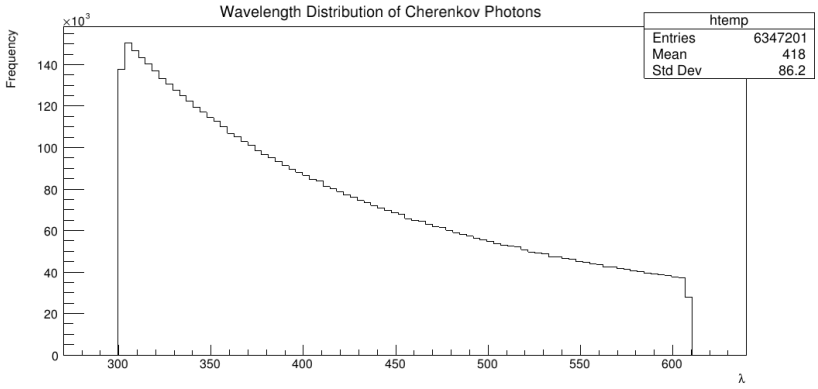

Figure 4.11: Wavelength of photons produced by Cherenkov due to the incidence of 1000 muons.

since, as we have shown in previous results, many more photons are produced by the passage of muons than by the passage of gamma rays.

Now, in Figures 4.13 and 4.12 we show the distribution of wavelengths for photons produced by Scintillation due to passing muons and gamma rays, respectively.

We note that again the most noticeable difference is in the number of photons detected, even though the number of photons produced by scintillation is lower, the rate between the amount produced by both primary particles is maintained.

The range of wavelengths is the same and the shape of the two plots is essentially the same. The difference between these distributions and those of the photons produced by Cherenkov is that in this case, we have a valley between 400 nm and 500 nm, with which we identify the overall maximum at 300 nm and a local maximum

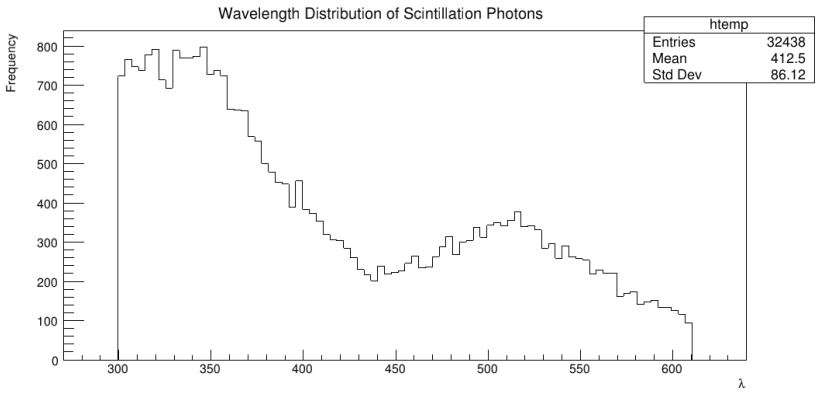

Figure 4.12: Wavelength of photons produced by Scintillation due to the incidence of 1000 gamma rays.

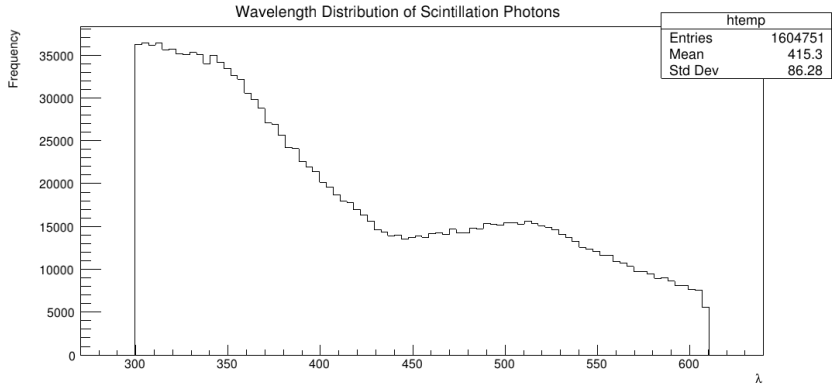

Figure 4.13: Wavelength of photons produced by Scintillation due to the incidence of 1000 muons.

around 520 nm.

Given these characteristics, we observe small differences between the wavelength distributions of the photons produced by both forms of production, but it is not possible to identify whether the photons were produced by muons or by gamma rays since the distributions are equivalent for both cases.

4.6.8 Secondary Electrons

In Figure 4.14 we show a general diagram of the experimental setup.

When gamma rays hit the sphere, secondary electrons are scattered by the Compton effect, which can produce photons by the Cherenkov effect if they have enough

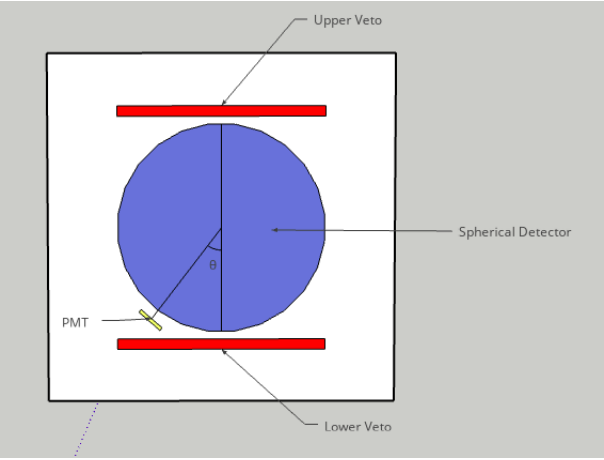

Figure 4.14: Frontal view of the experimental setup.

energy. If these electrons reach the lower veto they could also produce Cherenkov-type photons, so we would not only detect photons in the spherical detector but also in the lower veto.

When muons pass through the sphere, electrons are produced by ionization, either ionization by the muons or ionization by secondary electrons. Likewise, these electrons produce Cherenkov-type light if they have an energy greater than 175 keV and can produce signals in the lower veto if they pass through the sphere and reach the position of the lower veto.

At this stage of the simulation, the lower veto is about 20 centimeters away from the spherical detector.

When 1000 muons hit the experimental setup, a total of 78107 electrons are produced, of which only 91 reach the lower veto. If we consider how many of these electrons have enough energy to produce photons via the Cherenkov effect we find that only 52448 could cause this effect, of which only 53 reach the lower veto.

Now, when 1000 gamma rays strike, a total of 11542 electrons are produced, of which only 8284 have enough energy to produce photons of the Cherenkov type in water. In these 1000 events, no electron reached the lower veto. If we shoot 10000 gamma rays, 113235 electrons are now produced, of which only 9 reach the lower veto and have enough energy to produce the Cherenkov effect in water, as we can see in the Figure 4.15.

Moreover, these scattered electrons have no a preferred direction.
If we consider this condition of the secondary electrons that reach the lower veto

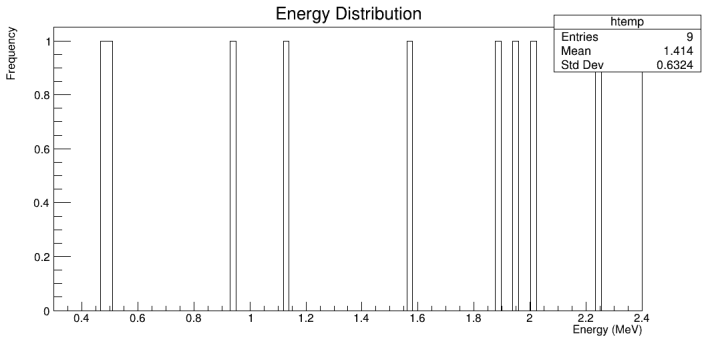

Figure 4.15: Energy of secondary electrons incident on the lower veto, produced by the passing of 10000 gamma rays.

and produce photons in it, we have to take into account that of the total number of electrons produced by the incidence of electrons, only 0.1% reach the lower veto, while when we shoot gamma only 0.006% of the electrons produced to reach the lower veto.

In Figure 4.16 we observe the energy distribution for the scattered electrons due to the incidence of muons in the experimental system. On the other hand, there is also no preferred direction for these scattered electrons.

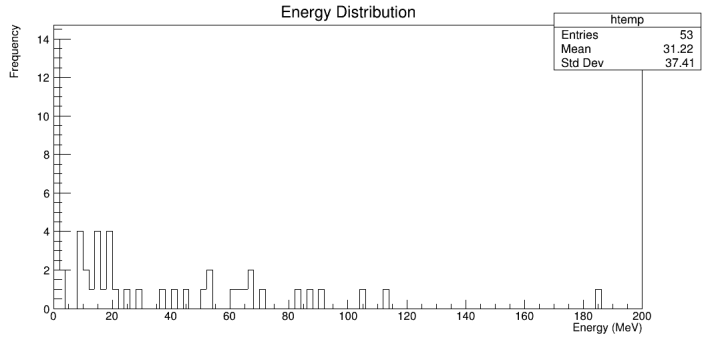

Figure 4.16: Energy of secondary electrons incident on the lower veto, produced by the passing of 1000 muons.

The conclusion is that if we decide to consider this secondary electron that reaches the lower veto, we would be imposing a condition that favors the detection of muons, not gamma rays. So far we already have sufficient conditions to detect muons with good efficiency, precisely the intention is to determine conditions to take advantage of the distinction of photons produced by the passage of muons in such a way that we improve the identification of photons produced by the passage of gamma rays.

4.7 Results

This second part of the simulation results is precisely the most important since we are simulating the entire experimental laboratory system. It is in this section that we take into account the time constraints among other conditions, in order to be able to directly compare the results that we obtain in this part with the measurements that we make in the laboratory.

With the previous section, we determined the best position to place the PMT, the regions where more photons are detected and we undertook the task of determining if the coincidence condition and the anti-veto condition work, at least to a first approximation to be able to identify the events produced by both primary particles.

We now refine the simulation with these considerations and show the results below.

4.7.1 Total photons detected in the spherical detector per event

From Figures 4.17 to 4.21, we observe the total number of photons detected for each of the 1000 events produced by both gamma rays and muons. What we must note in these plots is that the production of photons per event is not uniform, some events produce more photons than others.

If the photon production were uniform, then we could easily identify two regions of deposited energy and we could measure them and determine whether it was due to the passing of a gamma ray or a muon. That is not the case here, so we need to do a deeper study to determine the characteristics of the signals so that we can achieve our goal. Of course, we need to study the characteristics of the photons produced on the spherical detector, not on the vetoes.

It is clear from Figures 4.17 to 4.21 that the number of photons produced by muons is much greater than the number of photons produced by the passing of gamma rays, but we note that the maximum detection of photons produced by muons is when we place the PMT at 45°, as we see in Figure 4.19.

4.7.2 Time Consideration

When an event starts due to the shooting of a primary particle, a counter known as *Global Time* starts running, this counter stops when there are no more interactions resulting from the secondary particles in the event and restarts when another primary particle shot occurs.

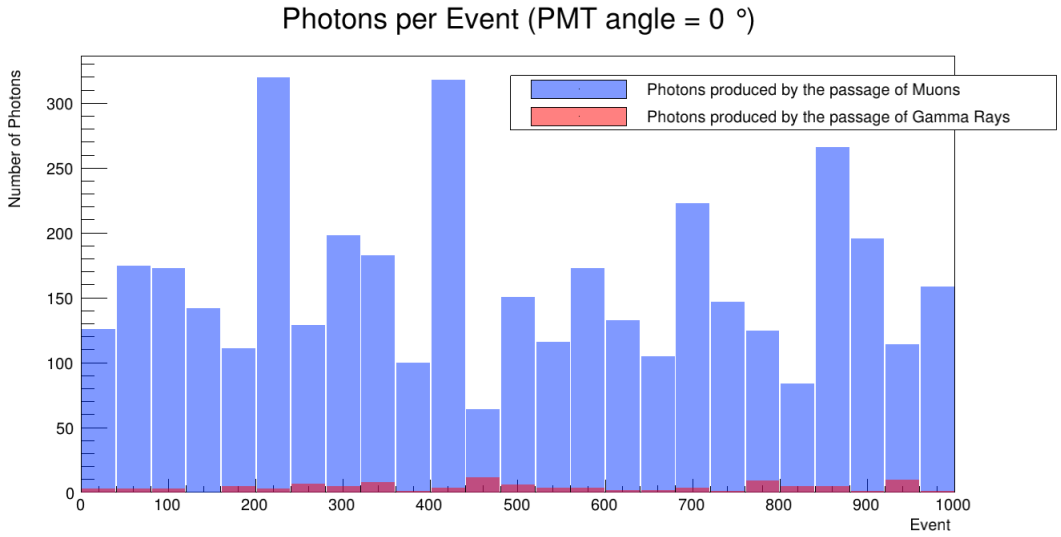

Figure 4.17: Total photons detected in the spherical detector per event. PMT angle: 0°.

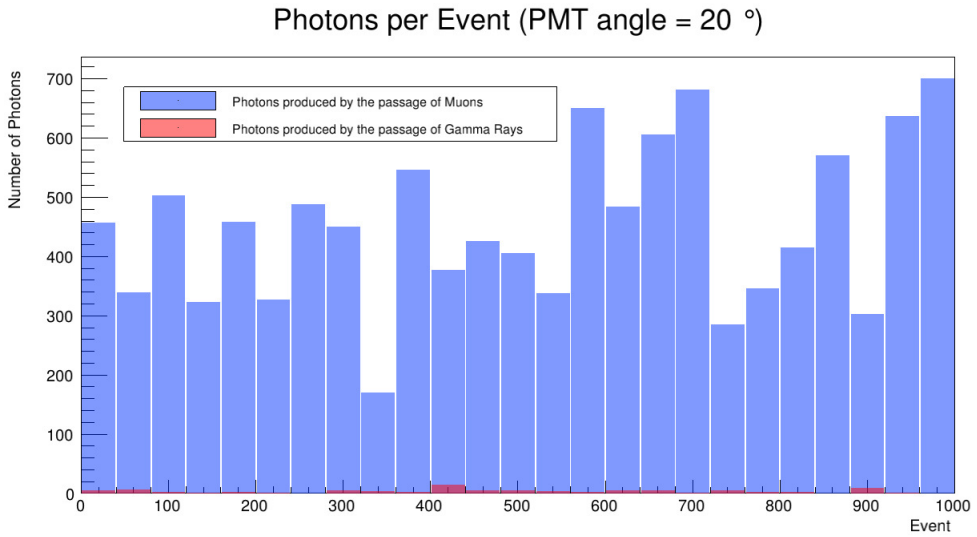

Figure 4.18: Total photons detected in the spherical detector per event. PMT angle: 20°.

In the simulation we have set the shot time of the particle to 0 ns, so from that point on we expect to detect the photons resulting from the interaction of the primary particle with the detectors. In a laboratory system, we don't measure a *Global Time* because we don't know at what time the incident primary particle was produced, but we do know that the particles we are interested in may have been produced in the Sun.

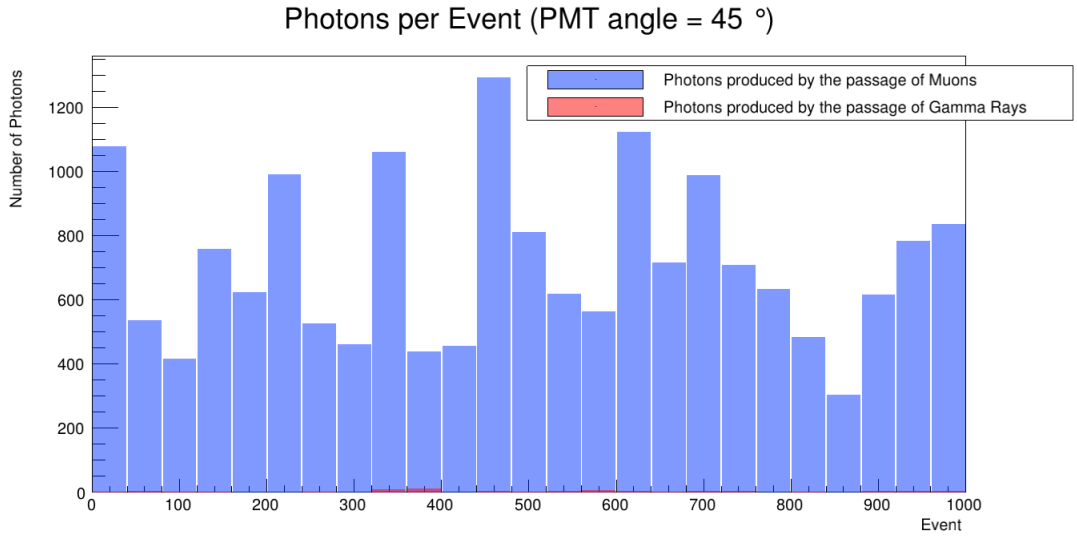

Figure 4.19: Total photons detected in the spherical detector per event. PMT angle: 45°.

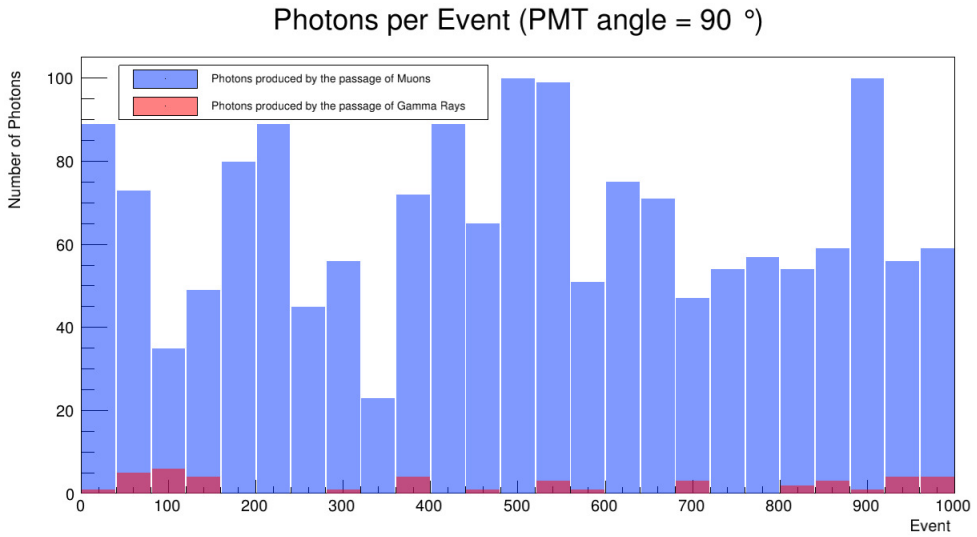

Figure 4.20: Total photons detected in the spherical detector per event. PMT angle: 90°.

Therefore, in the simulation we are not interested in measuring this *Global Time* but rather the flight times of the particle, that is, the time difference between the photons detected in each of the 3 detectors to determine some additional time criteria to validate these photons detected as the passage of a charged particle.

Let us remember that when we shot gamma rays in the simulation, no signals

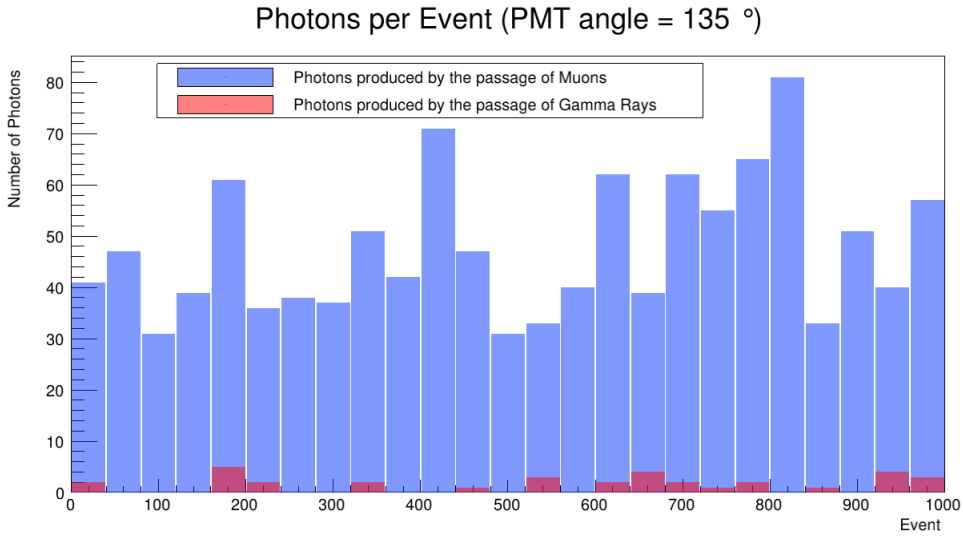

Figure 4.21: Total photons detected in the spherical detector per event. PMT angle: 135°.

were produced in the 3 detectors, so if we have a coincidence event, it would have been produced by a charged particle. In addition, once we determine the duration of the events we can then determine what time window we need to consider so that the coincidence criterion is complete, we are not only interested in photons being produced in the 3 detectors but we also want to determine the temporal resolution we need to validate these signals.

For the time measurement results in Event Duration and Flight time we have placed the PMT aligned to the vertical axis, that is, with a zenith angle of 0°.

Length of events produced by Muons

When we shoot muons in the experimental system, photons are produced in all 3 detectors, in many of these events photons are detected in all 3 detectors simultaneously. Each detected photon carries the information of the *Global Time* in which it was detected, so the duration of the event is exactly given by the time difference between the first and the last detected photon.

Specifically, the conditions considered are the following: a muon is shot, if in this event photons were detected in the 3 detectors, we access the detection time of each of them and arrange them from the smallest to the largest with which we determine the time that elapsed between the detection of the first and the last photon.

Note that we are looking at temporary differences but not the *Global Times* them-

selves. In the Figure 4.22 we observe the duration of the events produced by the incidence of 1000 muons.

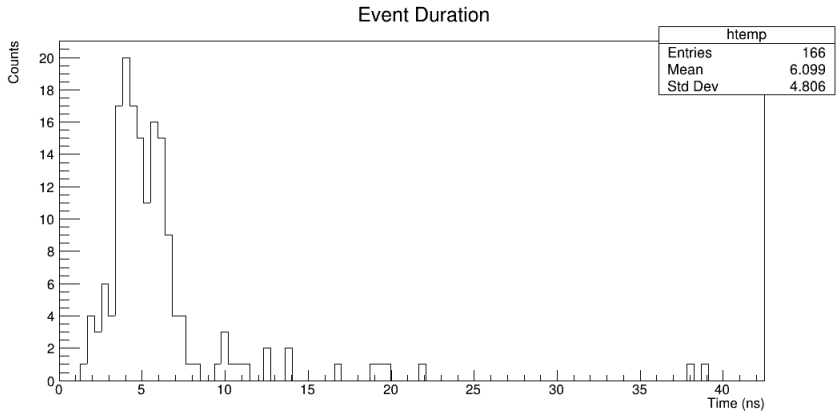

Figure 4.22: Length of events produced by the incidence of Muons.

We note that the duration of the events is generally less than 5 ns, with an average of 4 ns. Some events are longer but much less frequent, these delays may be due to the time it takes the photons to propagate through the water in the spherical detector, or to the reflection of the photons in the vetos before reaching the PMT.

For the purpose of this condition, we can consider 5 ns as an acceptable time window for validating coincidences produced by muon incidence.

Flight Time

The flight time is the time difference between the photons detected in each of the detectors of the experimental system, more precisely, it is the time difference between the first photons detected in each detector, since it is with this that we will determine the resolution necessary to detect of the muons.

In Figure 4.23 we show the flight time between the top veto and the sphere. Since the muon is incident from top to bottom, we expect the times measured at the top veto to be less than those measured at the sphere, so we define

$$t_{V1-S} = t_S - t_{V1}.$$

Note that the flight time between the upper veto and the sphere is typically 1 ns. If the photon production is very fast, the photons may be detected simultaneously on a scale of nanoseconds, which is why we also have a significant fraction of flight times equal to zero. The fact that we also have negative flight times means that photons were detected first in the sphere and then in the upper veto. This is a result of the

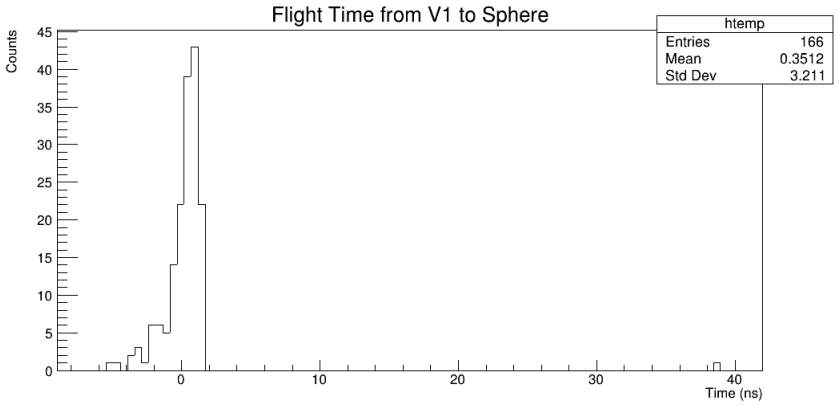

Figure 4.23: Flight time between upper veto and sphere.

time it takes for photons to reflect inside the vetoes until they reach the PMT.

The conclusion is that the time of flight between the upper veto and the sphere is 1 ns.

In Figure 4.24 we observe the flight time between the sphere and the lower veto. Now we define the flight time is defined as

$$t_{S-V2} = t_{V2} - t_S.$$

In this case, the time difference in both detectors is more obvious, which is 1 ns followed by a difference of 2 ns; with this we verify that most of the photons produced are detected first in the sphere than in the lower veto.

There are times when we first detect photons produced in the lower veto before those produced in the sphere, remember that photons travel slower in water, so there is a delay at the time of detection. Time differences less than zero occur less frequently than in the case of the upper veto and the sphere.

Finally, we measure the flight time between the upper veto and the lower veto, through the accommodation of the experimental system, then we define

$$t_{V1-V2} = t_{V2} - t_{V1}.$$

In Figure 4.25 we can see that the flight time between the upper veto and the lower veto is mainly 2 ns, which is consistent with the expected results when compared to Figures 4.23 and 4.24. For faster events, we have a time of flight of 1 ns between both detectors, these two being the most recurrent flight times in the simulation.

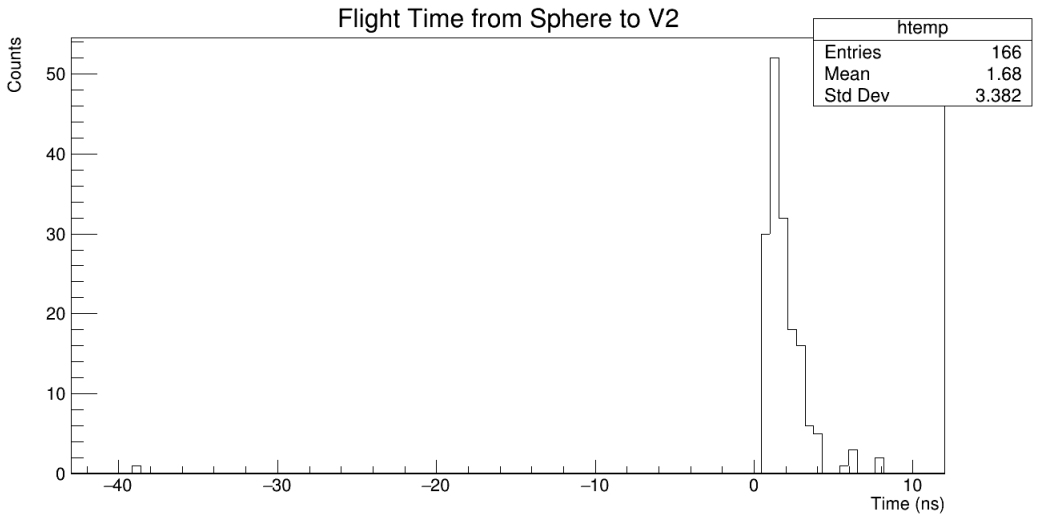

Figure 4.24: Flight time between the sphere and the lower veto.

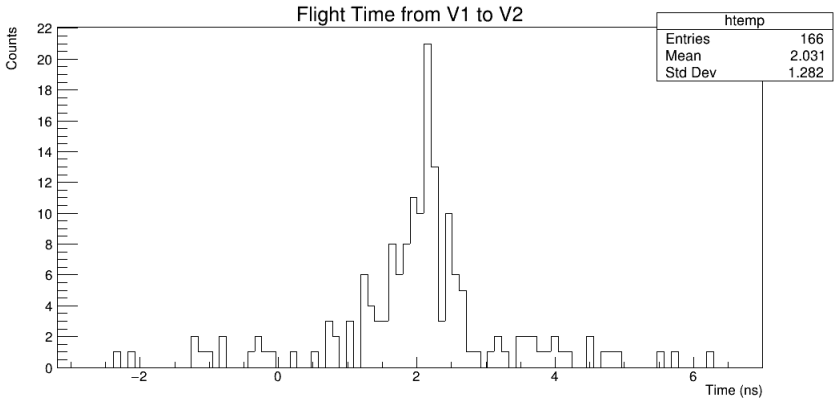

Figure 4.25: Flight time between the upper veto and the lower veto.

Again we notice that there are some time differences less than zero, which implies the delay between the production of photons and their detection, or, under the right conditions, we could determine that these signals were produced by incident particles from the bottom up.

In conclusion, the flight time between a detector and its consecutive is 1 ns. There are cases where the photons are detected first in the successive detectors, so we have to consider how we can establish an appropriate time window to consider these photons since they are all part of the same event produced by the incidence of a muon.

4.7.3 Coincidences with Time Consideration

We must be more stringent when selecting events produced by muons to distinguish them from those produced by gamma rays.

For example, we must vary the position of the PMT in the sphere to determine not only in which of these positions will detect more photons but also which will maximize the detection efficiency of photons that satisfy the temporal constraints that we determined in the previous sections.

Let's take the case of Figure 4.24, where we discard the negative values for causality reasons and zoom in on the region of highest concentration, which is exactly between 0 and 5 ns. We observe these considerations in Figure 4.26.

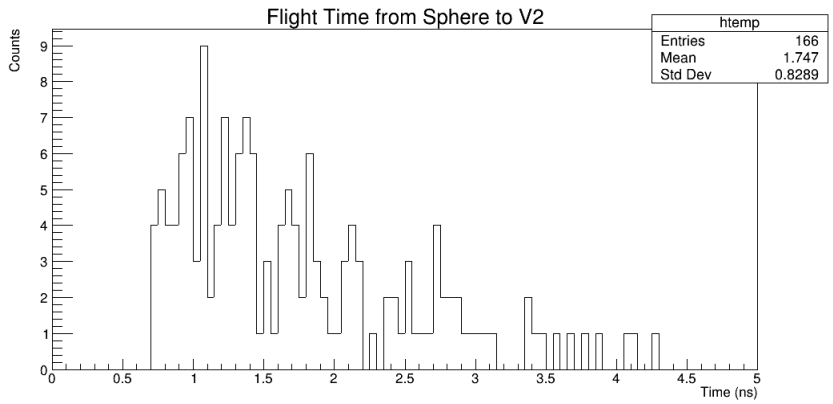

Figure 4.26: Flight time between the upper veto and the lower veto. We show the region between 0 and 5 ns.

Ideally, we expect the measured time of flight between the sphere and the lower veto to be 1 ns when the PMT is positioned at 0° relative to the vertical axis, that is when the optical window of the PMT coupled to the sphere is at the same distance from the lower veto as from the upper veto. We notice that we measure some times less than 1 ns, in particular, we notice that we start counting photons with times from 0.7 ns, that is, there is a difference of 0.3 ns below the expected value in the expected time. Therefore, we can consider an uncertainty of $\pm$ 5 ns, since according to this graph it is a reasonable value to consider in order to limit the time differences to an acceptable range. In this case, we then have two conditions for each event:

1. It must be produced and detected in all 3 detectors.
2. The photon detection time between the sphere and the bottom veto should be 1 ± 0.3 ns.

Coincidences for 1000 events (Muons)					
	0°	20°	45°	90°	135°
Coincidences	166	125	151	114	72
Coincidences with temporal restriction	59	36	56	32	15
Rate	35.5%	28.8%	37.0%	28.0%	20.8%

Table 4.9: Events that satisfy validation by coincidences with temporal restriction.

Now, if we vary the position of the coupled PMT on the sphere without changing the vertical position of the sphere, we notice that as we increase this zenith angle, we will further separate this PMT from the lower veto and, therefore, we expect the photon detection time between the sphere and the vetos to increase. We first obtain the expression to determine the vertical displacement of the PMT coupled to the sphere.

Let us denote the vertical displacement as Δz and let r be the radius of the sphere, which is 15 cm. Let θ be the zenith angle of the PMT measured from the geometric center of the sphere, so that

$$R = \Delta z + Rcos\theta,$$

so

$$\Delta z = R - Rcos\theta = R(1 - cos\theta). \tag{4.1}$$

The distance between the window of the PMT coupled to the sphere and the lower veto is 30 cm, if we have a particle traveling close to the speed of light then it will travel this distance in 1 ns, which is what we expect in the ideal case. Thus, by determining what the displacement Δz is, we can estimate how long the increase in photon detection time between the sphere and the lower veto will be. This detection time difference increases as the distance between this PMT and the lower veto increases.

The exercise we do with the simulation is then to plot these differences in detection times, identify the time at which the maximum value of the distribution is found, and then consider that value, with the corresponding uncertainty of $\pm$ 0.3 ns, to apply the temporary constraint between the sphere and the lower veto. We do this for each of the zenith angles that we have studied so far.

In the Table 4.9 we show the results of this study when we impose the condition of coincidences with temporary constraint, given that the coincidences occur only when charged particles are incident, the results of the Table are only for 1000 muon events.

From the previous sections, we had concluded that when the PMT of the sphere was placed at an angle of 0° or 45°, the muon detection efficiency by the coincidence

Anti-veto condition for 1000 events										
	0°		20°		45°		90°		135°	
	Muon	γ	Muon	γ	Muon	γ	Muon	γ	Muon	γ
Events	314	64	311	61	268	58	202	32	189	26
Rate Events	20.3%		19.6%		21.6%		15.8%		13.7%	

Table 4.10: Events that satisfy the anti-veto condition.

method was maximum. The above was without considering the time constraint.

Now considering the detection time of the photons in the sphere and the lower veto, we notice that there is a decrease in the number of validated matches, but the highest detection efficiency for this case was when the PMT angle is 45°. To be less strict, we can say that basically, the detection efficiency with temporal considerations is basically equivalent for angles between 0° and 90°, only when we consider the case where the PMT is placed at 135° is when we can notice a significant decrease in this detection efficiency.

4.7.4 Angular Distribution with Anti-veto Condition and Intensities Analysis

Let us remember that another strong condition for the identification of gamma rays is the anti-veto condition, in which we consider those events in which photons have been detected only in the spherical detector. Since sometimes charged particles also satisfy this condition, it is necessary to study the angular distribution of the photons when this condition is satisfied for one of the two incident primary particles.

Note that in this case, we don't consider any time constraint since we don't measure flight times between the vetoes and the sphere, in which case there is no signal in the vetoes. Nor we are interested in measuring the global time in which the particles are detected, in the simulation we know the time and position in which the primary particles are shot, in the laboratory system the gamma rays of interest are produced on the solar surface but we do not know the time in which this happens.

In Table 4.10 we show the results of the measurement of the angular distribution of the photons validated by the anti-veto condition, comparing results for both incident primary particles.

Considering the anti-veto condition, we find that we detect muons more efficiently when we place the PMT at 0°, while the highest gamma detection efficiency is at an angle of 90°. We are interested in the ratio of events validated with the anti-veto condition for muons and gamma rays, i.e. we want to know at which of these positions

is where the proportion of validated photons, produced by gamma rays, with this condition is greater than the proportion of validated photons produced by muons. We observe that this ratio is maximum when the PMT is at 90°. So far we have considered the efficiency by counting how many events satisfy the anti-veto condition for 1000 incident primary particles, now it is necessary to consider the properties of the photons that have been validated with this condition.

Wavelength Distribution

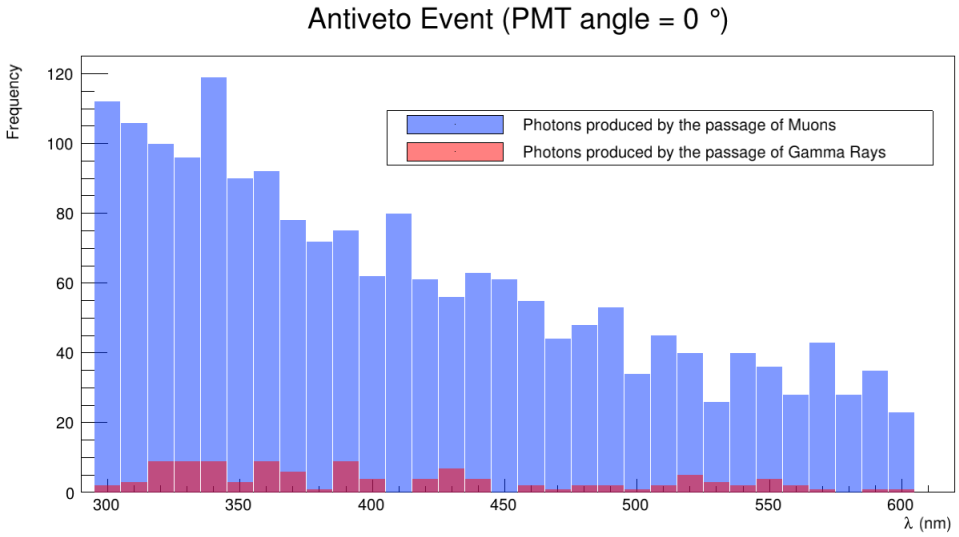

Figure 4.27: Wavelength distribution of photons validated by anti-veto condition. PMT angle: 0°.

.

In the Table 4.11 we now show the number of photons that have been validated with the anti-veto condition and the ratio between them when they are produced by gamma rays and by muons. First, we look at the angles where more photons were validated. In the case of muons, this happens when the PMT is placed at 20° and 45°, while in the case of gamma rays, we have the maximum at 45° and 90^0, at 90^o the overall maximum.

We must consider the rate between the photons detected. In the PMT the light signal is converted into an electrical signal, and depending on the number of photons entering the PMT, the amplitude of the electrical signal in the meter will change. Given this, then the ratio between the photons detected is equivalent to the ratio between the amplitudes of the electrical signals that we will detect. We are interested in those regions where the ratio between the signals produced by muons and those produced by gamma rays is not very large so that we do not confuse the lower

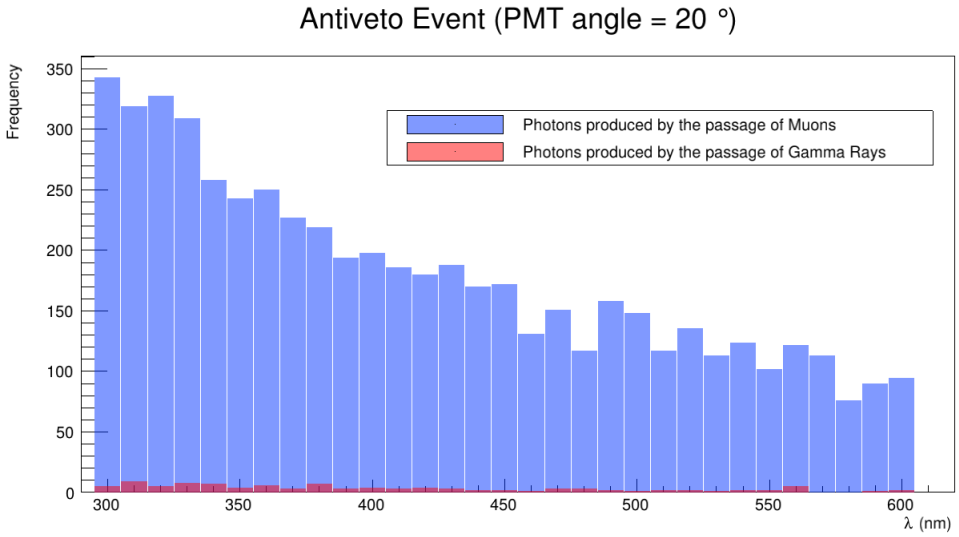

Figure 4.28: Wavelength distribution of photons validated by anti-veto condition. PMT angle: 20°

.

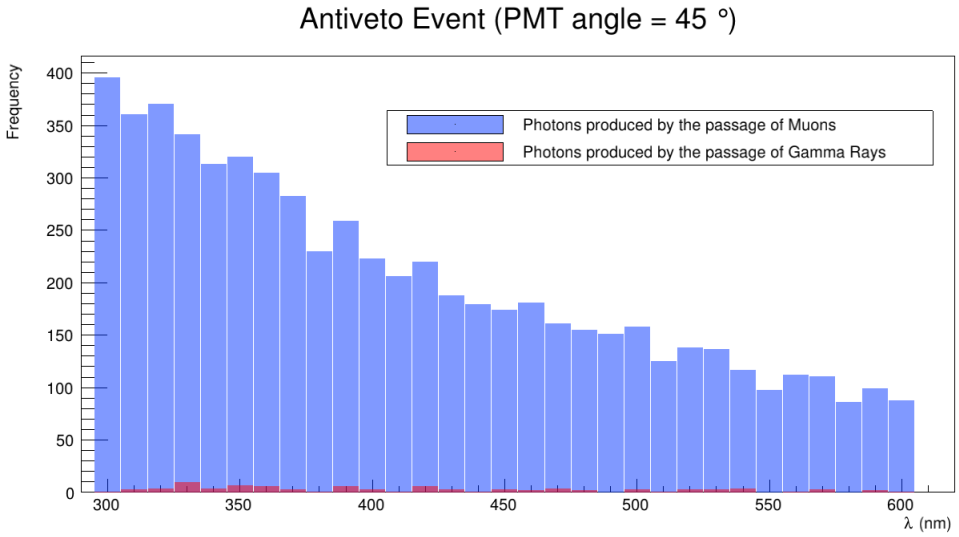

Figure 4.29: Wavelength distribution of photons validated by anti-veto condition. PMT angle: 45°.

amplitude signals with noise and so that the range of amplitudes that we consider is not so very large.

We find that, for example, that we have to discard placing the PMT at 20° from the vertical axis, since the electrical signals produced by muon incidence would be almost 139 times larger than the signals produced by gamma rays. We then consider

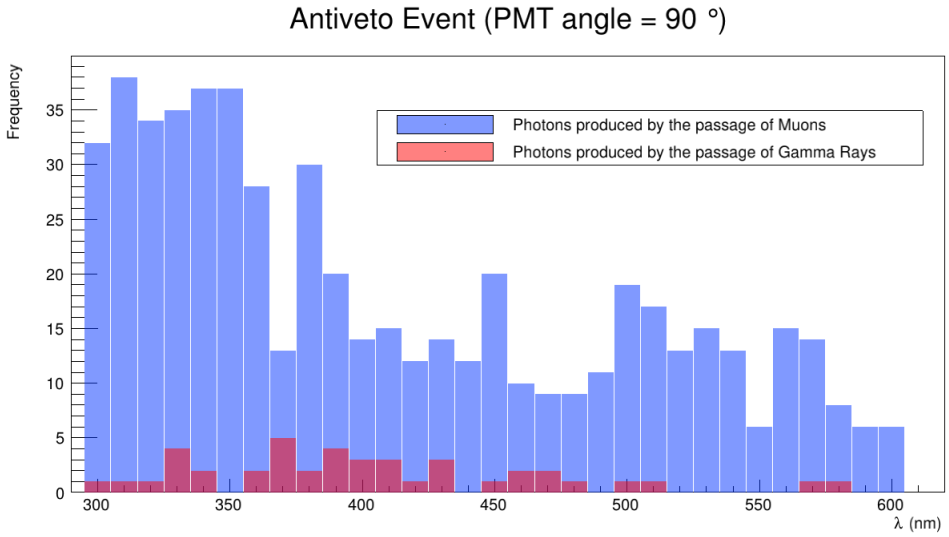

Figure 4.30: Wavelength distribution of photons validated by anti-veto condition. PMT angle: 90°.

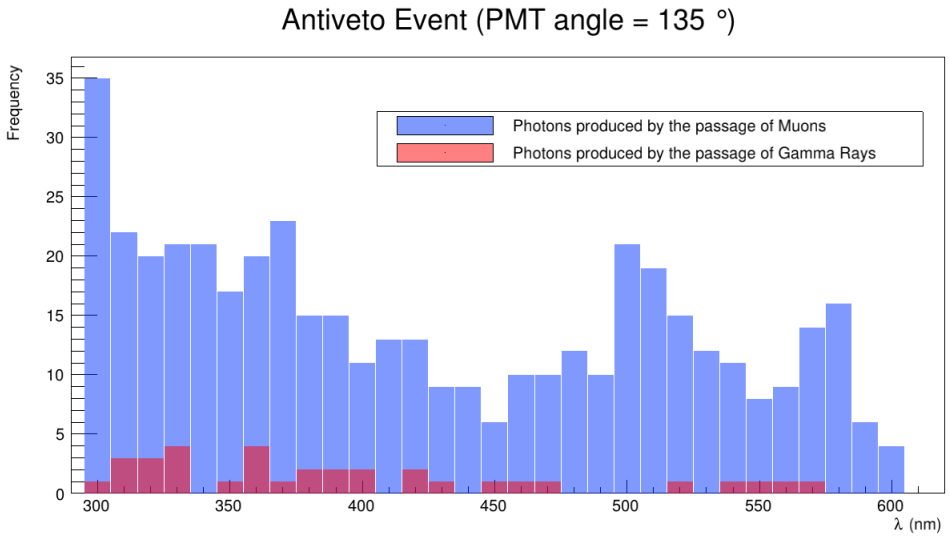

Figure 4.31: Wavelength distribution of photons validated by anti-veto condition. PMT angle: 135°.

the region where this ratio is minimum, which happens when the PMT is 90° from the vertical. Using the same criteria, we can exclude any region between 0° and 45°, since the amount of photons detected by muon incidence is much larger than that detected by gamma rays incidence.

Now we will present the information contained in the tables graphically, so that

Anti-veto condition for 1000 eventos										
	0°		20°		45°		90°		135°	
	Muon	γ	Muon	γ	Muon	γ	Muon	γ	Muon	γ
Photons	1906	108	5589	102	6304	91	562	43	449	34
Rate Photons	17.65		54.79		69.27		13.07		13.20	

Table 4.11: Total photons detected in events that satisfy the anti-veto condition.

the identification criteria of the photons produced by the passage of each of the primary particles are more visual.

First, we see in Figure 4.32 the total energy deposition on the PMT per event. We can see the shape of the distribution for the photons produced by the passing of the two primary particles we are studying, but it is not so clear at lower energies because we have some very energetic events, the most intense being due to the passing of muons. In Figure 4.33 we have made a zoom on this graph so that we can focus only on the lower energy events. Although both graphs follow the same distribution, we can easily see that as we look for higher energy events, we no longer see that these events are caused by the passing of gamma rays. So, we need to cut data, first to eliminate the highest energy events that we know were caused by the passing of muons, and second to look only at the lower energy events and measure the average energy of the photons detected due to the passing of both primary particles.

In this way, if we look only at the low-energy events, we can compare the events we measure with the average energies of the photons detected in the simulation and then we can assign the signals to the passing of one or the other primary particle.

If we detect a lot of photons, the energy deposition on the PMT will be greater, so the amplitudes of the signals will be also be greater. So we need to determine the average amplitudes of the signals to compare them and distinguish the cause of these events.

In this case, where the PMT is placed at 0°, we apply the energy cutoff at 25 eV, so that we have only the lower energy events where all of the events produced by gamma rays are included. We measure the following quantities

- Average energy of detected photons produced by gamma rays: 4.765 eV
- Average energy of detected photons produced by muons: 9.634 eV.

So, on average, the amplitudes of the signals produced by the passing of muons will be twice as large as the signals produced by the passing of gamma rays.

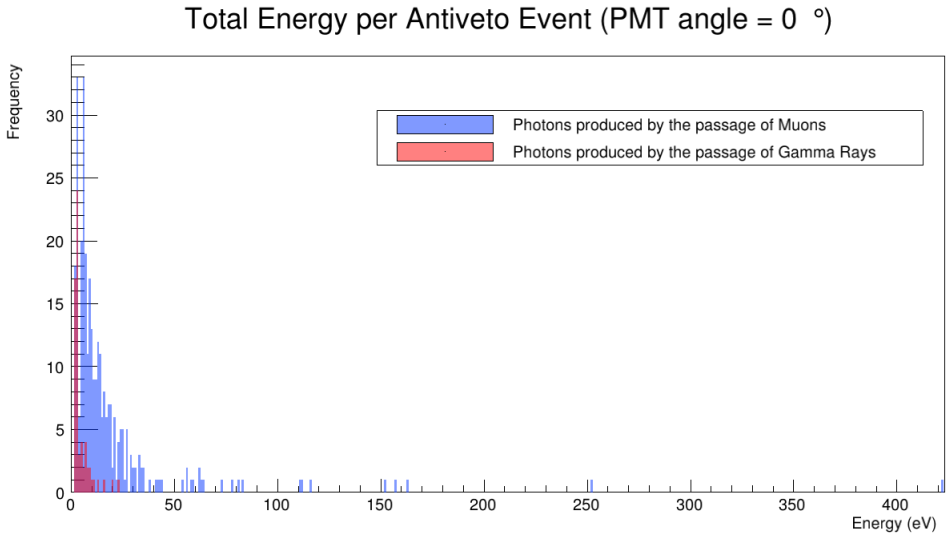

Figure 4.32: Photons produced in events validated by the anti-veto condition. PMT angle: 0°.

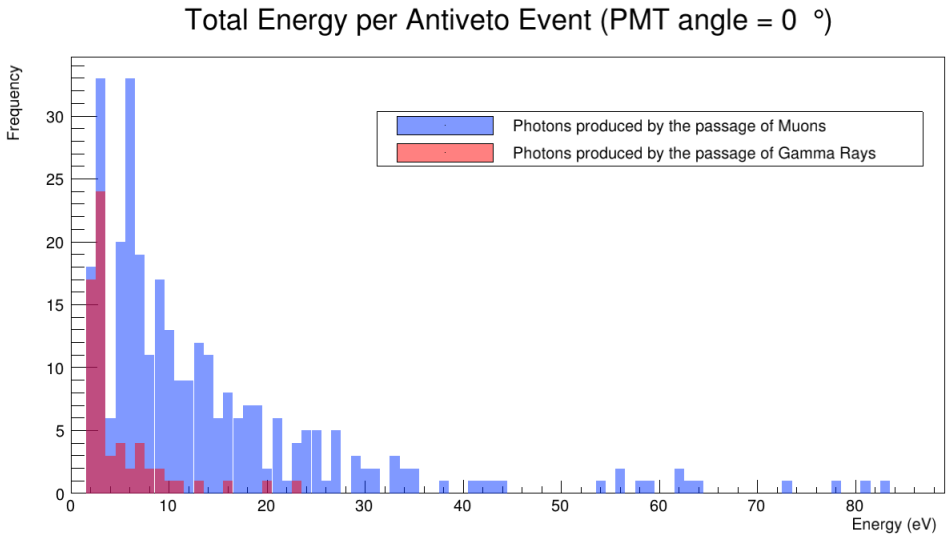

Figure 4.33: Photons produced in events validated by the anti-veto condition. ZOOM in, PMT angle: 0°.

In Figure 4.34 we can see the total energy deposition on the PMT per event when the PMT is at 20° from the vertical axis. Again, we identify the higher energy events as muon passes, the most intense being around 440 eV. To better appreciate the distribution of the graphs at lower energies, we apply zoom to Figure 4.34, which is Figure 4.35. In this case, the higher energy measured by the passing of gamma rays is $\sim$ 30 eV, so a good section would be 32 eV. In this way, we discard all of the most

intense events, which are produced by the passing of muons, and we include in the lower energy region all of the events produced by gamma rays.

When we measure the average energy in this low-energy region, we find that at 20° we have

- Average energy of detected photons produced by gamma rays: 4.803 eV.
- Average energy of detected photons produced by muons: 13.458 eV.

that is, the amplitude of the signals produced by muons would be about three times greater than the signals produced by gamma rays.

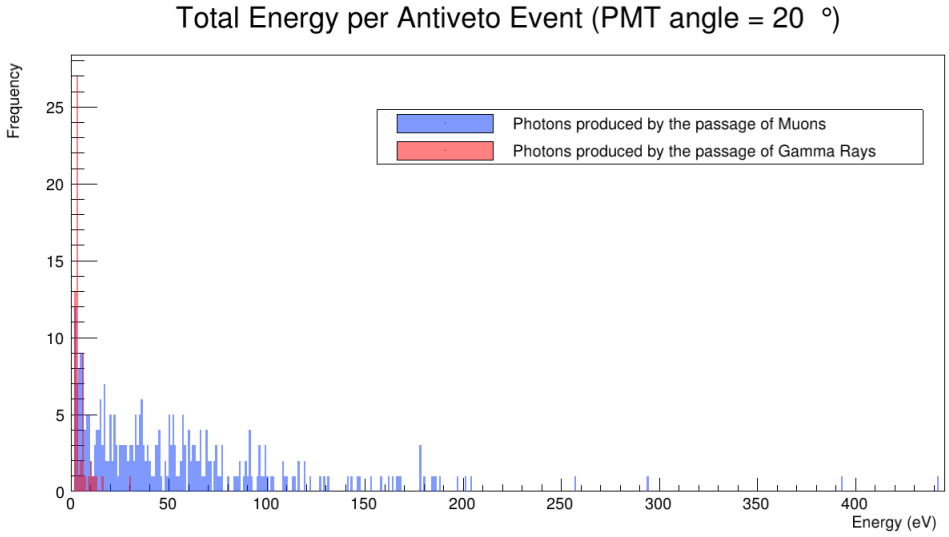

Figure 4.34: Photons produced in events validated by the anti-veto condition. PMT angle: 20°.

In Figures 4.36 and 4.37 we show the total energy deposition on the PMT per event when the PMT is at 45° and its zoomed version, respectively. In this case, the higher energy event was $\sim$ 410 eV and it was caused by a muon. If we look at the zoomed graph, we see that the higher energy event produced by a gamma ray was 22 eV, so in this case a proper cut would be 25 eV, as it was for the case where the PMT was at 0°. With this cut, we measured the average energy for the lower energy region and found

- Average energy of detected photons produced by gamma rays: 4.275 eV.
- Average energy of detected photons produced by muons: 8.980 eV.

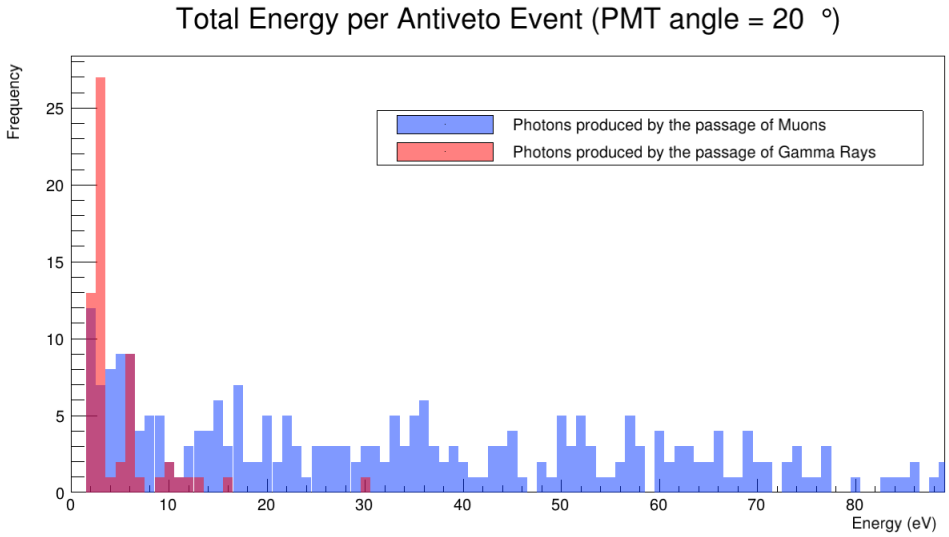

Figure 4.35: Photons produced in events validated by the anti-veto condition. ZOOM in, PMT angle: 20°.

so the amplitude of the signals produced by muons would be twice that of the signals produced by gamma rays.

Finally, in Figures 4.38 and 4.39 we show the total energy deposition on the PMT per event when the PMT is at 90° and 135°, respectively. In this case, even the events produced by muons are not as energetic as in the previous cases.

For the case of the PMT at 90° we measured

- Average energy of detected photons produced by gamma rays: 3.687 eV.
- Average energy of detected photons produced by muons: 5.761 eV.

and for the case of the PMT placed at 135°, we have

- Average energy of detected photons produced by gamma rays: 3.769 eV.
- Average energy of detected photons produced by muons: 5.267 eV.

In Table 4.12 we summarize the conclusions of this section, considering the cuts we made, the average energy detected per event, and the rate between the amplitudes of the signals produced by the two primary particles: gamma rays and muons.

In general, we observe that the events with low photon production are the most numerous when both primary particles are incident, only that in the case of incident

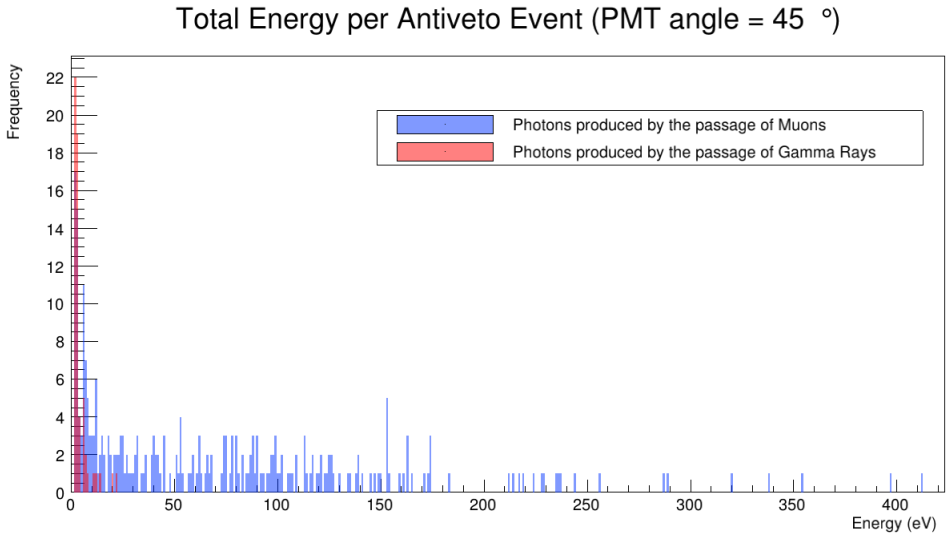

Figure 4.36: Photons produced in events validated by the anti-veto condition. PMT angle: 45°.

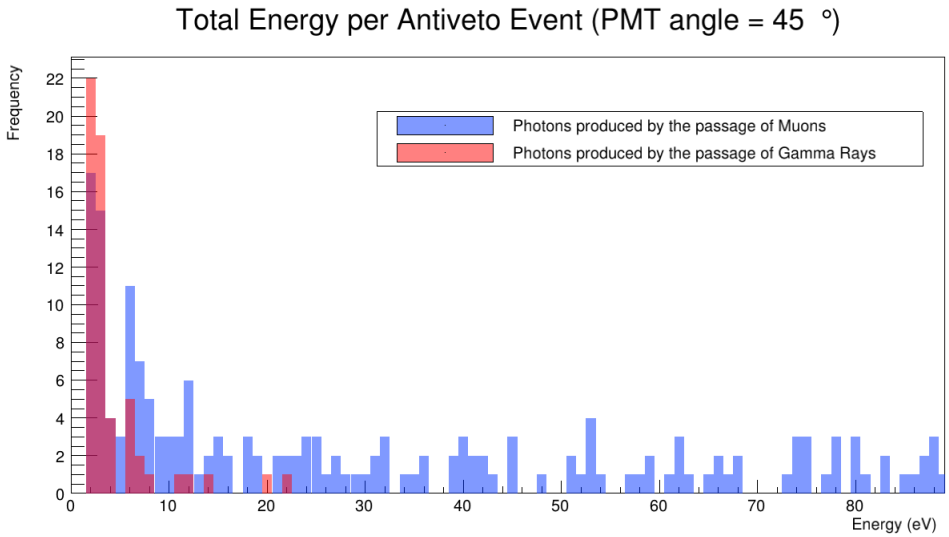

Figure 4.37: Photons produced in events validated by the anti-veto condition. ZOOM in, PMT angle: 45°.

muons, it is possible to appreciate a wider distribution of detected photons, so that in case of detection of very intense signals we can immediately associate them with the passage of a muon.

In an event with weak signals, we will have to use other criteria to determine whether the signal is caused by a primary particle or the other. We notice that when

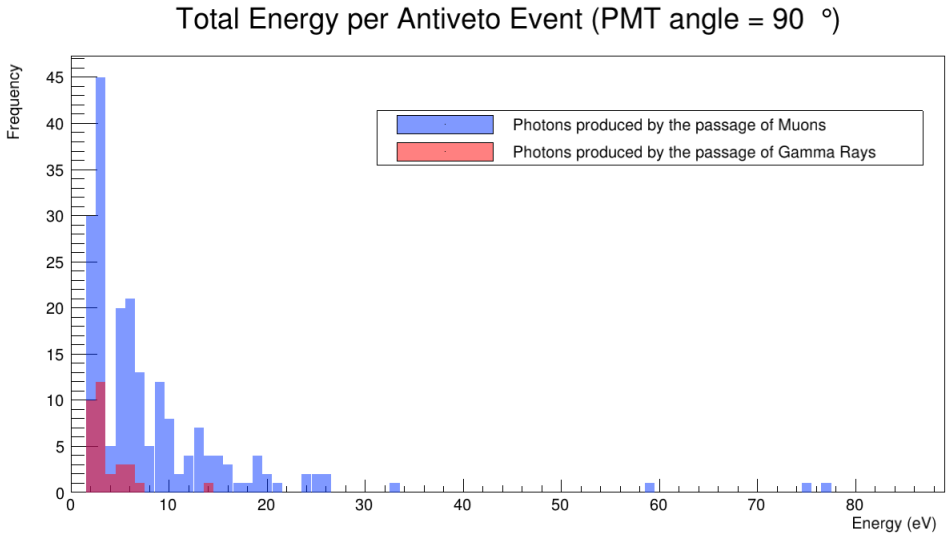

Figure 4.38: Photons produced in events validated by the anti-veto condition. ZOOM in, PMT angle: 90°.

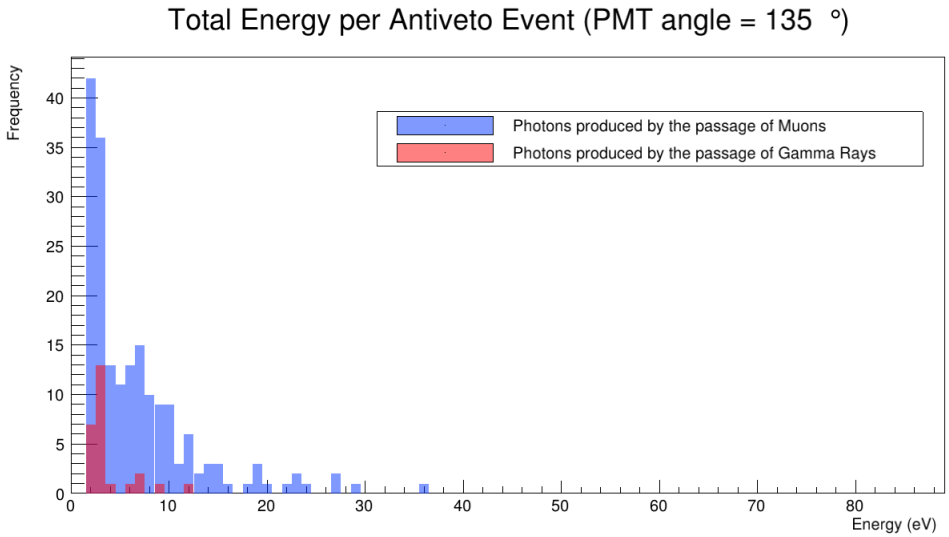

Figure 4.39: Photons produced in events validated by the anti-veto condition. PMT angle: 135°.

the PMT is at 20° or 45°, the difference between the distribution of photons produced by the passage of muons is much more noticeable since it covers a wider range of photons produced and at very high frequencies. At these two angles, we detect the strongest signals and they are produced by muons.

Something to note is that, in all cases, the maximum frequency is when we detect

PMT angle	Energy cut (eV)	Average energy γ (eV)	Average energy μ (eV)	Rate
0°	25	4.765	9.634	2.022
20°	32	4.803	13.458	2.802
45°	25	4.275	8.980	2.100
90°	15	3.687	5.761	1.562
135°	15	3.769	5.267	1.397

Table 4.12: Average energy detected in the low energy range due to the passing of gamma rays and muons.

one photon, and from there, as we look at cases where we detected more photons, the frequency with which they are detected decreases. So, if we have low-intensity signals, they can be produced by both primary particles; if we have a more intense signal, we can associate it with the passage of a charged particle.

4.7.5 Other Time Constraints

Only in the case of muon shooting do we have coincidences between the sphere and some of the vetos, even just between the vetos only. We need to take advantage of this feature to determine other criteria that are useful for distinguishing signals by criteria other than coincidences in the 3 detectors.

A particle traveling at the speed of light passes through the entire experimental setup in about 2 ns, considering the delay times in which the Cherenkov-type photons propagate until they reach the PMTs, we can assume that any event that occurs with a time window less than or equal to 5 ns is due to the passage of a charged particle. Thus, the condition is as follows:

$$0\ ns \leq \Delta t \leq 5\ ns. \tag{4.2}$$

where Δt is the time between a photon being detected at one detector and a photon being detected at the next detector.

From the configuration of the experimental system we expect that, since the particles come from the top down, the photons will be detected first in the upper veto, then in the sphere, and finally in the lower veto, so the time differences should all be positive under this consideration. However, there are cases where, for example, we detect the first photons in the sphere before the upper veto, so in the simulation, we ignore these events from our analysis. By chance, we then consider positive time windows (for particles coming from top to bottom) and less than or equal to 5 ns.

In principle, we can apply this temporary restriction to any event where there is a simultaneous signal in at least two detectors. The events to consider are the following:

- Simultaneous signal on both vetoes and sphere.
- Simultaneous signal on top veto and sphere only.
- Simultaneous signal on the sphere and lower veto only.
- Simultaneous signal on vetoes only.

In Table 4.13 we show the results of comparing the total number of events validated by each of these criteria with the total number of these events that are now validated by the causal temporal constraint. In this way, we determine which conditions are more useful to consider in the laboratory system, keeping in mind that these conditions are only satisfied when muons are incident.

We compare the results at two different angles of the PMT on the sphere, at 0°, 20°, 45°, 90°, and 135°.
where Δt is the time between a photon being detected at one detector and a photon being detected at the next detector.

From the configuration of the experimental system we expect that, since the particles come from the top down, the photons will be detected first in the upper veto, then in the sphere, and finally in the lower veto, so the time differences should all be positive under this consideration. However, there are cases where, for example, we detect the first photons in the sphere before the upper veto, so in the simulation, we ignore these events from our analysis. By chance, we then consider positive time windows (for particles coming from top to bottom) and less than or equal to 5 ns.

In principle, we can apply this temporary restriction to any event where there is a simultaneous signal in at least two detectors. The events to consider are the following:

- Simultaneous signal on both vetoes and sphere.
- Simultaneous signal on top veto and sphere only.
- Simultaneous signal on the sphere and lower veto only.
- Simultaneous signal on vetoes only.

In Table 4.13 we show the results of comparing the total number of events validated by each of these criteria with the total number of these events that are now validated by the causal temporal constraint. In this way, we determine which conditions are more useful to consider in the laboratory system, keeping in mind that

1000 events produced by muons								
PMT	V1-S-V2		V1-Sphere		Sphere-V2		V1-V2	
at	Total	Δt	Total	Δt	Total	Δt	Total	Δt
0°	159	154	98	39	103	96	84	84
Rate	98.8%		37.8%		93.2%		100%	
PMT	V1-S-V2		V1-Sphere		Sphere-V2		V1-V2	
at	Total	Δt	Total	Δt	Total	Δt	Total	Δt
20°	141	137	97	35	102	97	115	112
Rate	97.2%		36.1%		95.1%		97.4%	
PMT	V1-S-V2		V1-Sphere		Sphere-V2		V1-V2	
at	Total	Δt	Total	Δt	Total	Δt	Total	Δt
45°	134	132	85	42	96	90	123	121
Rate	98.5%		49.4%		97.7%		98.4%	
PMT	V1-S-V2		V1-Sphere		Sphere-V2		V1-V2	
at	Total	Δt	Total	Δt	Total	Δt	Total	Δt
90°	104	96	75	29	86	72	158	155
Tasa	92.3%		38.7%		83.7%		98.1%	
PMT	V1-S-V2		V1-Sphere		Sphere-V2		V1-V2	
at	Total	Δt	Total	Δt	Total	Δt	Total	Δt
135°	83	69	67	35	48	44	158	151
Tasa	83.1%		52.2%		91.7%		95.6%	

Table 4.13: Time constrained coincidence events. $\Delta t = 5$ ns.

these conditions are only satisfied when muons are incident.

We compare the results at five different angles of the PMT on the sphere, at 0°, 20°, 45°, 90°, and 135°.

We observe that the ratio between validated events and total coincidence events is higher when we consider the matches in the 3 detectors and only in the vetoes. The other two criteria have a lower ratio between the two parameters, so their consideration is not convenient because it could generate confusion regarding the information validated with this restriction, in addition to the fact that we lose an important part of the sample when applying these conditions.

Therefore, the conclusion is that we will use the criteria of coincidences in the 3 detectors and coincidences in the vetoes to discriminate the signals of charged particles. Applying the temporal restriction we can now speak of the concept of simultaneity for which we consider that an event produced by a charged particle will be less than or equal to 5 ns.

4.8 Discussion

With the simulation results, we have noted the following important points to consider: The production of optical photons occurs by two processes: either by scintillation or by Cherenkov radiation, independent of the primary particle shot.

Photon production by Cherenkov is dominant, of 100% of the photons produced, about two-thirds are by Cherenkov.

The total number of photons produced by muons is much larger than the total number of photons produced by gamma rays. Although the anti-veto condition applies to muons and gamma rays, a fundamental result obtained is that in none of the events we obtained a simultaneous signal in the 3 detectors, so when this condition is met, it is sufficient evidence to say that this event It was produced by the passage of a charged particle.

The detection of photons produced by gamma rays in the water detector is improved if we place the PMT at small angles around the vertical axis, a result that we observe directly.

Air is not a good detection medium. Replacing the water inside the sphere with air in the simulation, we conclude that it can work to detect charged particles, but with much lower efficiency. However, the air did not serve to detect gamma rays in any of the cases, so we determined that it is always necessary to use detection materials that have at least the refractive index of water and its density.

It is possible to identify photons produced by Cherenkov and Scintillation when the primary particle is a muon, when gamma rays are shot there is no distinction between the two forms of production. In any case, the identification of the production mode in the detector medium is not a good criterion for determining whether the photons were produced by gamma rays or by muons, since the spatial distribution of these photons overlaps even if the incident primary particles are different.

Gamma rays of 2.22 MeV energy produce optical photons with a higher concentration in the center of the detection plane. Gamma rays with energies of the order of keV or less do not produce optical photons. Gamma rays with energies of the order of GeV produce many optical photons, but they are not directed toward the center of the detection plane.

Furthermore, there is no difference between photons produced by the incidence of negatively charged muons and positively charged muons, both primary particles produce photons with the same properties.

Selection criteria		
Condition	Muons	Gamma Rays
Vetoes	Coincidences	Anti-veto condition
PMT Zenith angle	45°	0°-20°
Wavelenghts	300-620 nm	300-620 nm
Detection media	Water, Air	Water
Secondary electrons	Ionization	Compton

Table 4.14: Simulation results

In the Table 4.14 we summarize the main results of the study of the simulation of the experimental system.

Chapter 5

Construction

With the study of the experimental setup we have exposed in previous Chapters, we finally get to the construction, this chapter is the product of all this study. We build 3 photon detectors, the aluminum structure to hold the detectors, connectors, etc.

The whole construction was made in the Elementary Particles Laboratory [1].

5.1 3D printing

Before describing each of the constructed components, we mention some features of 3D printing because it was an important tool to get some of the parts we needed in our experimental setup.

The software and equipment we used are from *Creality*, the designs we made in *SketchUp* were downloaded in *STL* format to then be exported through the *Creality* software into *gcode* format which contains information such as the number of layers of the part, the amount of material we need to print each part, and an approximate printing time. With this information, the printer reads the file and starts the printing.

The printer uses *PLA*, so that the print tip heats up to 200° while the print bed maintains a temperature of 40° so that the material adheres to the bed during the first few print layers. By default, the software adds a tiny *PLA* base to the design. At the end of the printing, it is very easy to remove this base from the original figure.

For more information about the 3D printer, please consult *Creality* official website. We will talk about the pieces we 3D printed, basically were

- 2 PMT supports for the vetoes.
- 2 PMT supports for the sphere.

- 1 piece for the vertex of the structure annex.
- 2 basis for the annex of the structure.
- 1 base for the valve.
- 2 guides for the optical windows on the sphere.

5.2 Veto Detectors

We used *AutoCAD* to design the planes with which we cut the metal parts of the veto detectors. Each veto is made up of a base (see Fig. 5.1a), a lid (see Fig. 5.1b), and 4 pieces that make up the sides of the box (see Fig. 5.1c). The lids and the bottoms were cut from a 1 mm width aluminum sheet, while the sides were cut from a 3.4 mm width aluminum sheet.

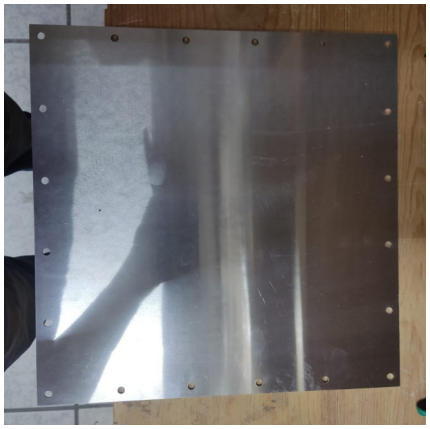

(a) Cut aluminum base.

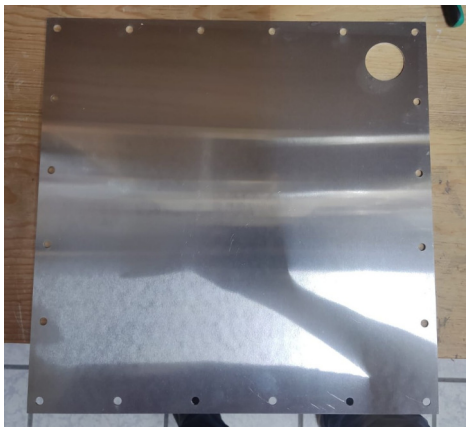

(b) Cut aluminum lid.

(c) Cut aluminum sides.

Figure 5.1: Parts of the aluminum boxes for vetoes.

Due to the veto conditions we consider, it is necessary to increase the reflectance inside the aluminum boxes. This is done by polishing each of the internal faces using a polishing machine and polishing cream. We look for the mirror finish in these faces

as we see in Figures 5.2a y 5.2a

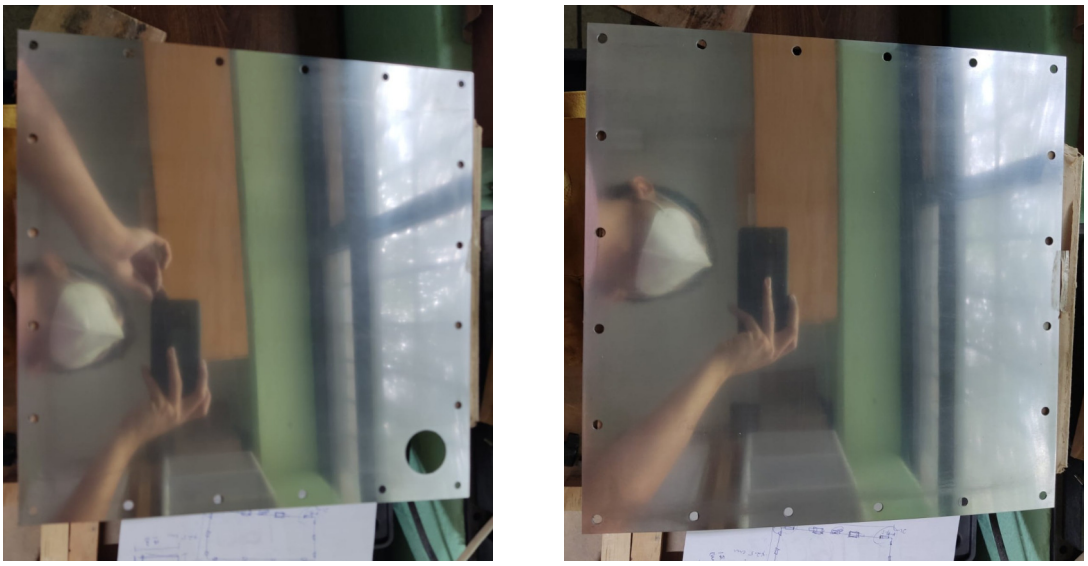

(a) Polished lid. (b) Polish base.

Figure 5.2: Polished materials.

The insides of the side panels were also mirror-polished to increase reflectance.

The *PLA* isn't opaque to visible light, so it was necessary to cover the inside and outside with aluminum tape. This way, we avoid possible light leakage to the PMTs and thus reduce the noise in our observations.

The PMT supports for the vetoes were 3D printed in white color. The printed pieces have some burrs (see Fig. 5.3a), once the printing is finished is necessary to clean all this waste for the figure to get it completely clean, as we observe in Figure 5.3b. In Figure 5.3c we show the support covered with aluminum tape. At this point, we can couple the support to the veto detector to place the PMT.

Then, we assembled the veto detectors. On top of the base, we placed the side pieces and the scintillator material in the center of this metal frame, as shown in Figure 5.4a. When we were sure that the scintillator material was well adapted to the frame, we removed the protective film. In Figure 5.4b we can see the green color of the scintillator material.

Finally, we placed the cover and closed with $1/4$ " $\times$ $3/8$ " screws and their nuts. We needed 40 screws and their nuts for the vetoes. The assembled vetoes are shown in Figures 5.4c y 5.4d. Note the covered hole where we place the PMT, this was done

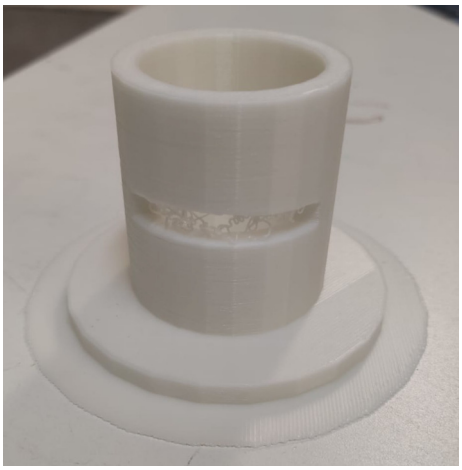

(a) Printed support.

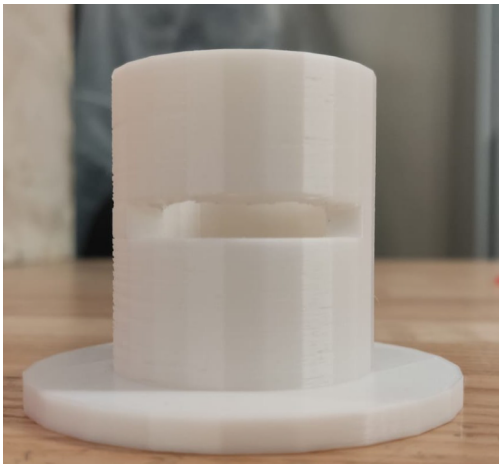

(b) Clean support.

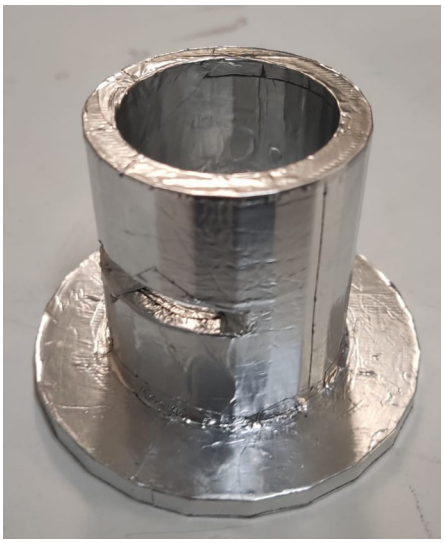

(c) Covered support.

Figure 5.3: PMT support for vetoes.

to prevent material damage, so we prevent a decrease in scintillation efficiency.

5.3 Aluminum Structure

We can see the main structure in Figure 5.5a, it consists of four 60 cm pieces, eight 30.2 cm pieces, and four corner connectors. In Figure 5.5b we show the main structure and the annex in which we will protect the PMT placed at 45° from the vertical. In the corners of the annex, there were spaces we needed to fill to make it more stable,

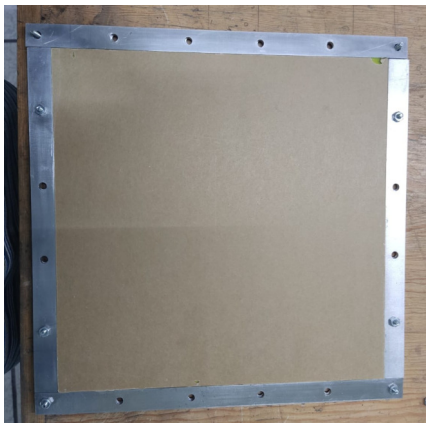

(a)

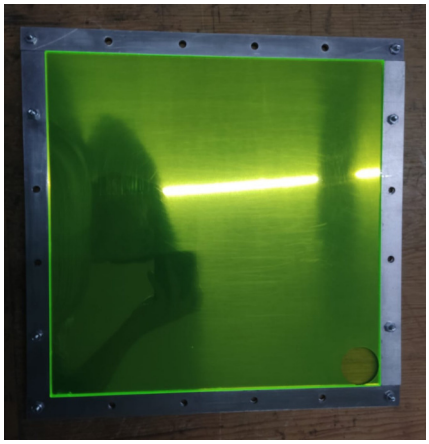

(b)

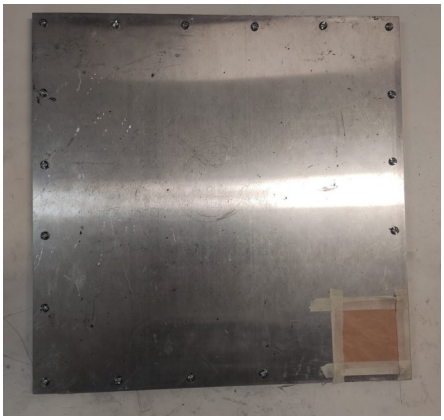

(c)

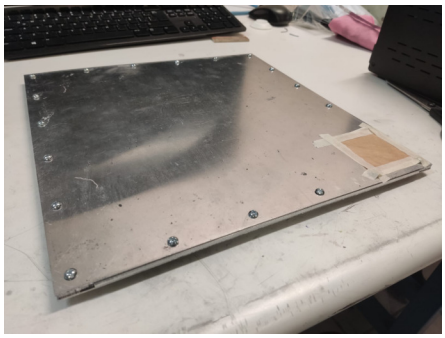

(d)

Figure 5.4: Veto.

we fill these corners with 3D printed parts as we can see in 5.5c. Also, the base of the secondary structure didn't have a base, the aluminum pieces were touching the table, so we also 3D printed two small bases for the aluminum extrusions. These pieces fit perfectly, as we can see in Figure 5.5d.

This part of the experimental setup completes the second of the three existing elements; this structure will hold the three detectors will hold along with their electronic components.

(a) Main Structure.

(b) Full Structure.

(c) Corner.

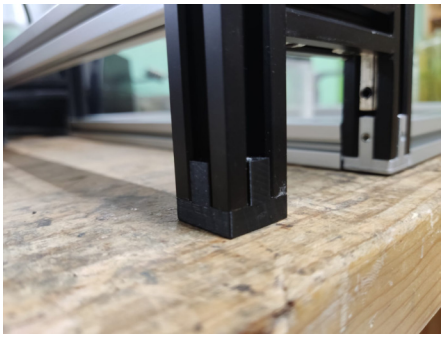

(d) Base.

Figure 5.5: Aluminum Structure.

5.4 Detector Sphere

The last and most important part of the whole experimental setup had to be done with special care. The spherical detector is the key element to identify the photons produced by the passing of gamma rays.

We have two hemispheres, and they are 1 mm of thickness. In Figure 5.6a shows one of them. We bought these pieces online. Each of them requires a different treatment because the elements attached to them are also different, but, both hemispheres will have something in common, their inner color.

Contrary to the vetoes, the inside of the sphere must have a minimum reflectance

to be able to apply each one of the conditions to distinguish the photons produced by gamma rays from those produced by muons. To achieve this goal, we paint the inside of both hemispheres black.

In Figures 5.6b and 5.6c we observe the inside of the sphere unpainted and painted in black, respectively. We painted with spray paint.

First, we will describe the work done with the top hemisphere, this is the one that will have the valve to fill the whole sphere with water, our detection medium where gamma rays and muons will interact with water molecules to produce photons.

So, to fill and empty the sphere we need one valve on top of the sphere, so we needed a 1/2" diameter perforation, which is the outside diameter of the valve we used. We can see the perforation done in Figure 5.7a. In Figure 5.7b we show the valve placed on top of the hemisphere. As you can see, it's not very stable considering that only 1 mm of the tube gets inside the sphere and the rest of the weight of the valve is supported by only this small fraction of the tube, so we also had to 3D print a support for the valve too, this piece is very similar to the one we printed to hold the PMT on the sphere, but it's smaller, as we told in the last Chapter. Finally, in Figure 5.7d we can see the valve connected to the sphere and held by this small support, which is also covered with aluminum tape to avoid leakage of photons inside the sphere.

The lower hemisphere required more work because the perforations needed to place the PMTs were much larger and we made two of them, both 36 mm in diameter. These are the places where we will detect the photons.

As we can remember, the inside of the hemisphere was painted in black, in Figure 5.8a we can take a look inside the lower hemisphere, we can now see both holes we made and if we look carefully , we can see that we removed some paint around both holes, this was done to put in the circular glass windows so that the glue we used would adhere to the metal and not to the paint. Later we will explain in detail what we did inside these holes. We can see the holes outside the hemisphere in Figure 5.8b. Outside the hemisphere is where we will place the PMT supports to hold the PMTs.

Once we had the holes made, we needed to attach the hemispheres to the aluminum frames that will hold the sphere on the aluminum structure. We can see both the top and bottom hemispheres in their frames in Figures 5.8c and 5.8, respectively.

Both aluminum frames are placed on a flat wooden base, which is covered with food-grade plastic. This is because in the Figures, inside of the frames are filled with resin, so next we need to explain now what we did with the resin.

(a) Outside of hemisphere.

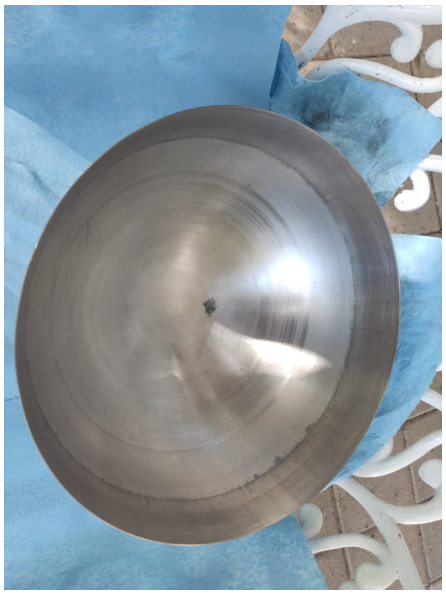

(b) Inside of hemisphere.

(c) Inside painted.

Figure 5.6: Hemisphere.

Epoxy Resin is made up of two components: resin and a hardener, we see them in Figure 5.9a. To prepare it, we need to mix equal amounts of resin and hardener and then mix them very well for a few minutes to create a homogeneous mixture. Depending on the resin used, the mixing may vary as well as the working time in

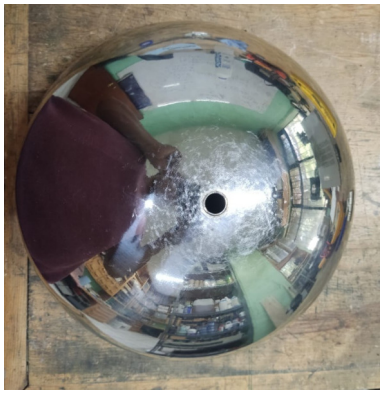

(a) Hole for valve.

(b) Valve in sphere.

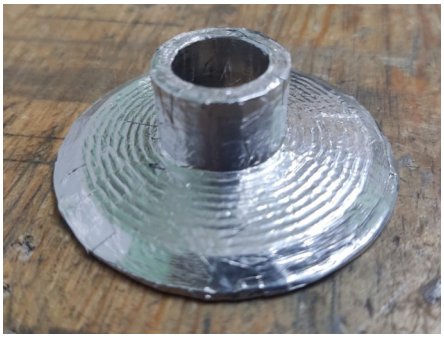

(c) Support for valve.

(d) Support and valve in sphere.

Figure 5.7: Upper hemisphere.

which the mixture begins to thicken and cure. For a single layer of the resin we used, it takes about 45 minutes to start thickening and the total time for a single layer of resin to completely cure is 72 hours.

The mix we made looked completely white, as we can see in Figure 5.9b, this was due to the number of bubbles created during the process. The manufacturer recommends mixing for at least three minutes. In Figure 5.9c we show the resin placed in one of the corners of the aluminum frames, it is easy to appreciate the white color of it, but we had to be very careful when pouring the mixture to avoid empty spaces and bubbles.

We had to pop all the bubbles with a heat gun, we applied heat evenly along all the resin and the mixture began to turn clear. We had to apply heat several times before the mixture began to thicken, as the bubbles continued to form but fewer each time. When we removed the bubbles, the mixture looked like in Figure 5.9d, and as it hardened, it became transparent.

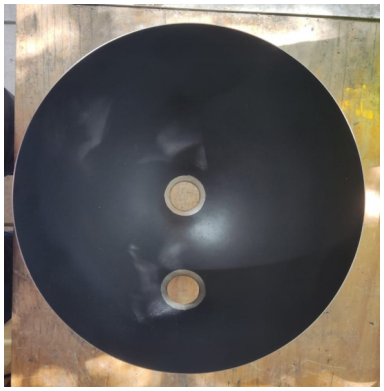

(a) Inside view of sphere.

(b) Outside view of sphere.

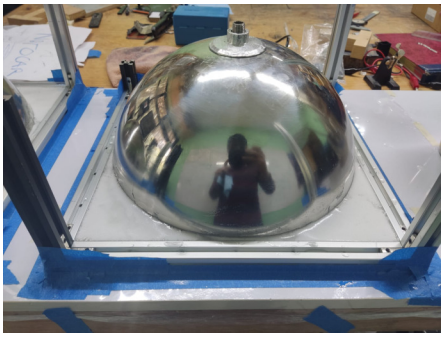

(c) Top hemisphere with resin.

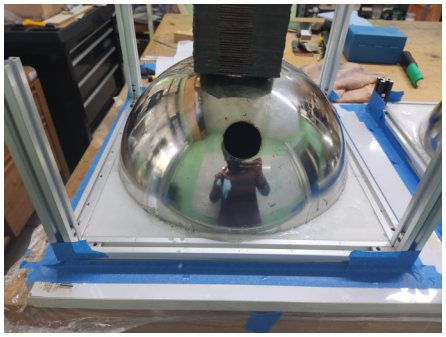

(d) Bottom hemisphere with resin.

Figure 5.8: Bottom hemisphere.

Now we need to talk about what we did on the lower hemisphere, first, we will explain what we did on the outside.

Similar to what we did with the PMT supports for the vetoes, we also worked with the PMT supports for the spherical detector. The material used to print these pieces was black, as we can see in Figure 5.10a.

The base of these supports has a spherical shape to couple to the spherical detector. Due to the limitations of 3D printing, this surface is not smooth enough so it doesn't couple to the sphere as well as we expected. We had to sand the surface to remove the excess material and we used an epoxy resin layer to cover the gaps created by the sanding process, which created a more appropriate connection between the two surfaces. Then, it was also necessary to cover the surfaces with aluminum tape to avoid any possible light leakage, the finished piece is shown in 5.10b.

Remember that we have two places to place the PMT, but we will only use one

(a) Resin and hardener.

(b) Mix of resin and hardener.

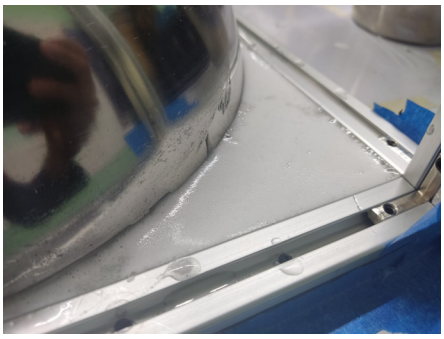

(c) Resin with bubbles.

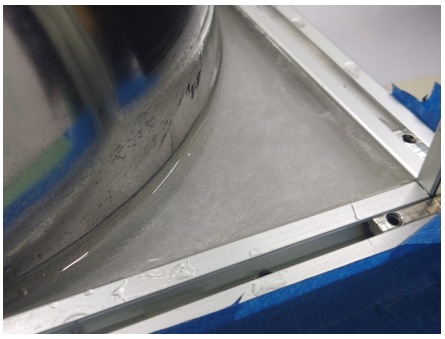

(d) Resin without bubbles.

Figure 5.9: Resin deposit.

at a time, so, when we use one of the supports to hold the PMT the other one will be empty and we need to cover it to avoid photon leakage, so we designed and 3D printed a cap, which is essentially a cylinder with a base that fits perfectly into the nozzles of the supports. We can see this cap in Figure 5.10c, it's also covered with aluminum tape to shield it from electromagnetic radiation. Finally, in Figure 5.10d we can see one of the supports with the cap. When we use this cap we must also cover the joint between the cap and the nozzle of the support with aluminum tape to prevent any photons from leaking to the PMT.

Both supports for the PMT were placed on their respective holes of the lower hemisphere, we used gray epoxy resin. Then, the joint of the support with the hemisphere was covered with aluminum tape to avoid possible leakage of photons to the inside of the sphere. When we made the test with the PMT at 0°, we covered the other support with the cape, using aluminum tape in the joint of both pieces to avoid leakage of photons. When we did a test with the PMT at 45°, we covered the other support in the same way.

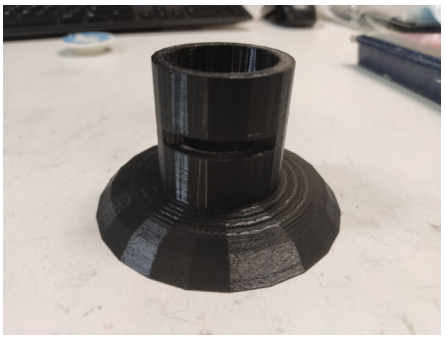

(a) Printed support.

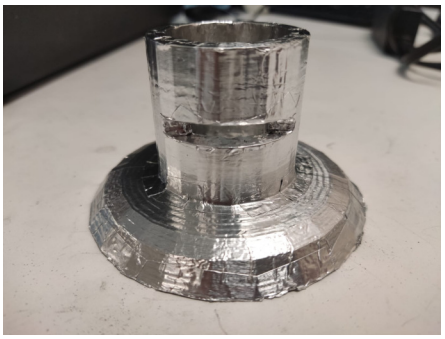

(b) Covered support.

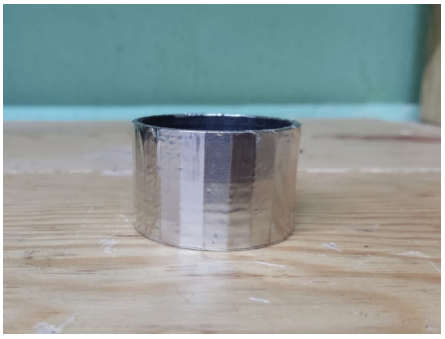

(c) Cap for support.

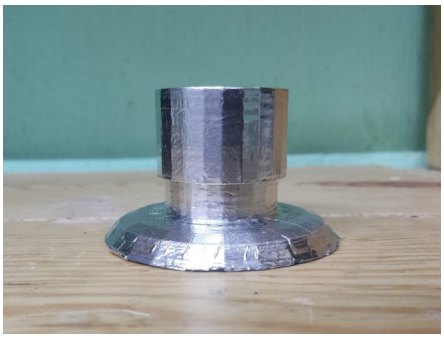

(d) Capped support.

Figure 5.10: PMT support for the spherical detector.

Finally, we placed our two optical windows in the holes of the lower hemisphere. We 3D printed two guides to limit the area where we would fill with glue the joint between the glass and the hemisphere. The glue we used was super glue mixed with a some titanium dioxide. We did some testing beforehand and found that this mixture produces in a hard glue that sticks well to the metal,it is water resistant, and doesn't lose its hardness. First, we fixed the guides, then we fixed the glass with glue only on the circumference of the glass. When the glasses were fixed, we filled all the remaining space between the glass and the guide with glue, so we avoid any water filtering through the glass.

It was very important to only use glue around the edges of the glass because in the center is where all of the photons would pass through to be detected by the PMT. When we finished filling it with glue, we filled the bottom hemisphere with water to see if there were any water leaks. When we didn't observe any leaks for 24 hours, we removed the water and began assembling the entire sphere.

5.4.1 Sphere assembling

Once the clear epoxy resin was completely cured, we had to apply another layer of epoxy, but this time we applied a gray epoxy that was harder once it cured and took much less time to cure. We also applied a small layer of silicone to prevent possible water filtration between the two hemispheres of the sphere .

It was very important to check the eight corners of the aluminum frames because the area where the resin and the silicone would be had to be flush to have better mechanical contact between the aluminum extrusions.

Our main goal was to avoid water and photon leaks, so we also cut three cross sections, two made of aluminum foil and one more made of neoprene. With aluminum we shield the inside of the sphere from outside photons, with neoprene we improve the mechanical contact between the two hemispheres, thus avoiding water leaks. The neoprene layer was placed between the aluminum layers. We also put a silicon edge between each layer.

Finally, the assembly was made by placing all 20 screws with their respective nuts around the aluminum frame. We also needed washers, 4 for each screw-nut pair, two in the head of the screw and two in the other extreme to make the nut very tight. We covered all the corners where the epoxy resin was with aluminum tape, and we covered all the aluminum frames as well, paying special attention to the joint of the two hemispheres, where we might have more photon leakage. First, we assembled the sphere by putting the two hemispheres together, then, using the L connectors and screws, we assembled the sphere to the main aluminum structure, so we were able to put all three detectors together to do the first tests.

The area where the nuts and bolts were was also covered with aluminum tape.

We filled the sphere with drinking water and a hose. We waited 3 full days without noticing any water leaks before proceeding with the tests. When we finished this test, we also covered the valve with aluminum tape.

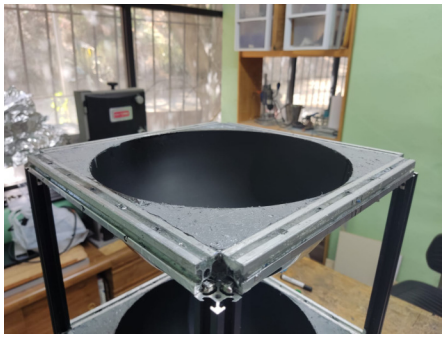

(a) Silicone layer.

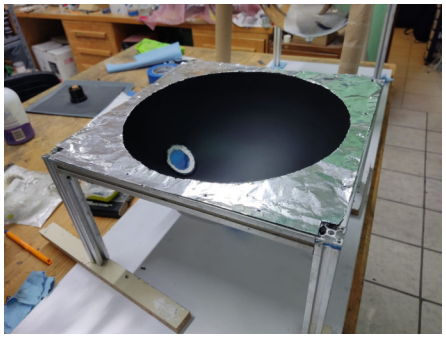

(b) Aluminum cross section.

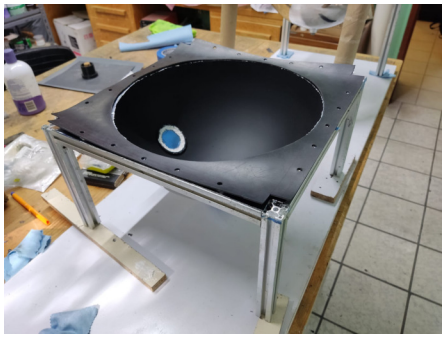

(c) Neoprene cross section.

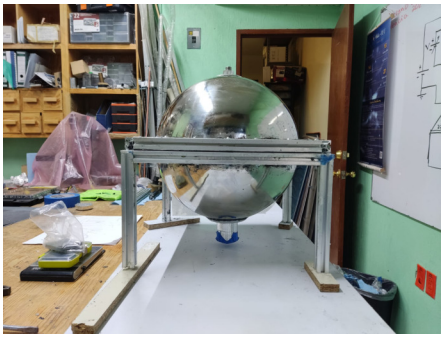

(d) Sphere assembled.

Figure 5.11: PMT support for the spherical detector.

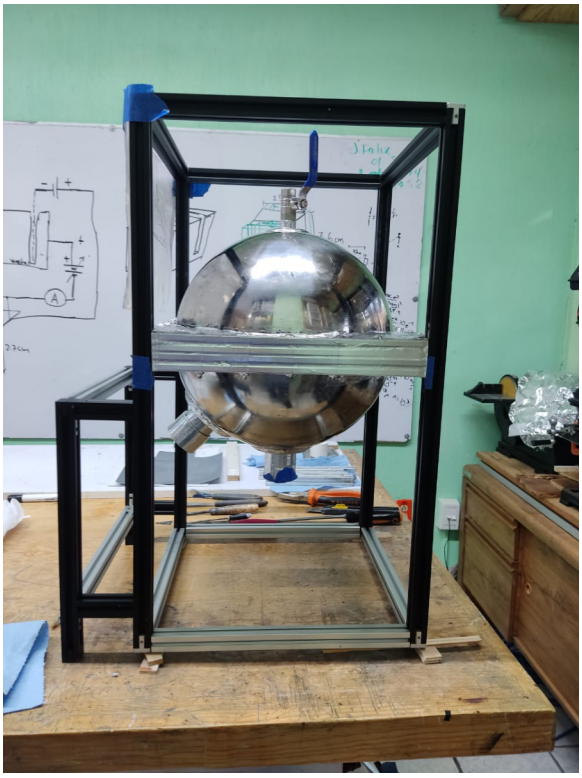

Figure 5.12: Sphere assembled on main structure.

Chapter 6

Testing

Once we finished building the experimental system, it was necessary to perform a series of tests to make sure that each component of the experimental system was working properly. In this Chapter, we will talk about the tests performed out and the results of each of them.

This Chapter is the one before the measurement process we'll use to obtain the results, so it's important to verify the operation of the detectors, the data acquisition system, and the connectors we use in each part.

6.1 Noise Measurement

There is noise in any electronic measurement device. In our case, we are working with PMTs and we need to make sure that the signals that we can associate with the detection of photons are not produced by noise.

Sometimes, fluctuations in the noise can cause us to validate signals that are not due to the photons hitting the PMT's optical screen. Therefore, we must set a *trigger* level, that is, the minimum voltage that the signals emitted by the PMT must have in order to be considered as non-noisy signals, that is, we set lower bound on the electrical signals produced.

The methodology is very simple, we measure the noise level in the experimental system and set the *trigger* as 3 times the measured noise level. In this way, we ensure with a 99% probability that the signals validated in the experimental system are produced by non-noisy signals.

In our vetoes the measured noise is ~ 25 mV, so we set the trigger level to 75 mV, so that we can validate signals with amplitudes greater than 75 mV as cosmic ray passes. Then, we need to analyze the amplitudes of the validated signals to classify

them as caused by muons or gamma rays.

In our Data Acquisition System we can set a trigger level so that we can only consider signals with lower or higher amplitude, in our case, we need to first set a trigger level to validate the signals as the passing of cosmic rays and then, we need to set another trigger level to discriminate the most intense signals as muons passing, this is a direct result we obtained from the simulation.

6.1.1 Vetoes Testing

We look for coincidences that match the time window we decided to consider based on the results of the simulation.

Both veto detectors work properly, we observe the characteristic signals of the passage of cosmic radiation, which has the form of an exponential decay. It was important to reduce the noise level by sealing the edges of them with aluminum tape.

The noise level we had on both veto detectors was $\sim$ 50 mV. For each veto we have a different channel in the oscilloscope, the voltage we use on each was as follows.

- Top Veto (CH1)
  - Power Input: 7 V.
  - Control Voltage: 0.8 V.
- Lower Veto (CH2)
  - Power Input: 7 V.
  - Control Voltage: 0.9 V.

We set these voltages on each PMT because when we set a larger value on any of them we observed an increase in the amplitude and frequency of the signals produced but there was also an increase in the noise and the shape of the signals began to distort.

Both vetoes emit signals with negative amplitude, we can change the display of the signals on the oscilloscope, so we can invert them on the horizontal axis, for example. On the oscilloscope, we can also change the trigger level, and the time resolution and we can set validation conditions in more than one channel simultaneously.

In this part of the test, we set the trigger level of both channels to 50 mV and we set the condition to measure both channels simultaneously, so we can detect coincidences with a certain delay, we need to capture these signals and then measure this

delay to decide if we can validate this event as a coincidence or not.

We now present some of the signals we have captured in this process.

In Figures 6.1 and 6.2 we show two pairs of signals whose delays are on the order of μs. Remember that, from the simulation, we set the time window to validate coincidences as

$$0 \leq \Delta t \leq 5ns$$

So, even though the delay is relatively short, we need a lower delay to validate these signals as coincidences, leaving aside the time duration of the signals, which is due to the characteristics of the PMTs, we are interested in the delay of the peaks of both signals. We are using the same model of PMT, the same power source, and the same oscilloscope to capture these signals, so the rise times of the signals must be the same and we can be more stringent when talking about the delay.

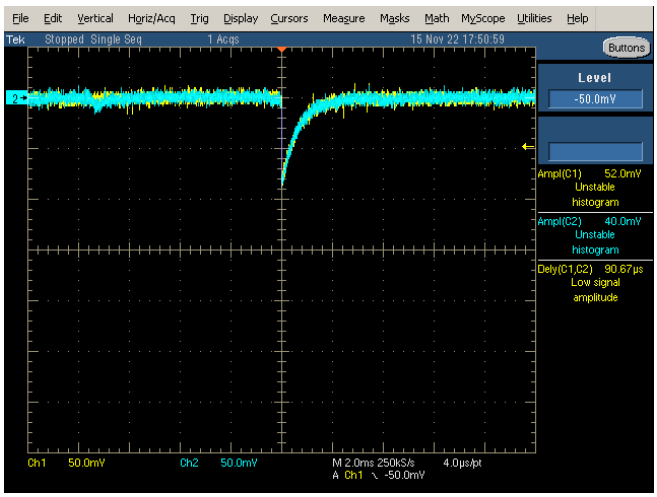

Figure 6.1: Coincidence with time delay of de 90.67 μs.

In Figure 6.3 we now show a coincidence with a time delay on the order of ns, it has a better resolution but is still larger than the time window we determined in the simulation.

Finally, we show (in Figure 6.4) a signal we detected on the oscilloscope that has a delay of ps, which is the best resolution we got with this data acquisition system and it fits the time window we are considering for coincidence events. This is the type of signal we are looking for to distinguish the passage of muons in the experimental setup.

In the end, we will be looking for signals produced only by the spherical detector, so it is important to make sure that the vetoes are working to get better results when we use all three channels.

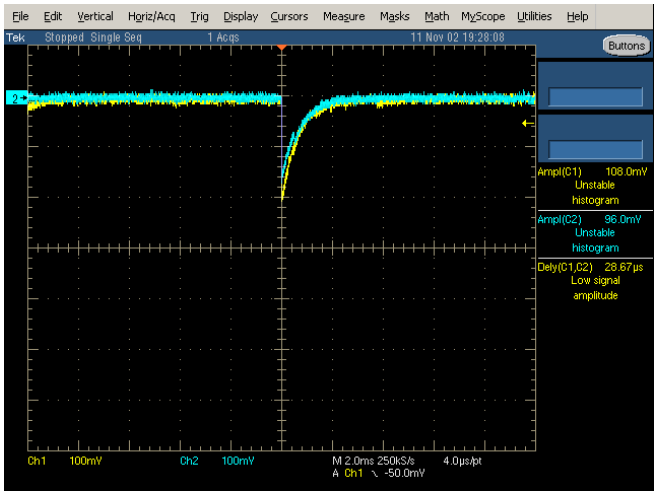

Figure 6.2: Coincidence with time delay of 28.67 μs.

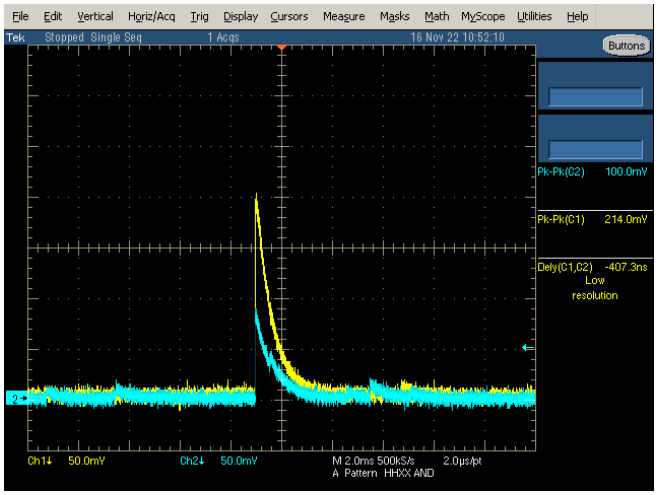

Figure 6.3: Coincidence with time delay of 407.3 ns.

6.2 Characterization

In the PMTs, there is a dependence between the applied voltage and the amplitudes of the output signals. We need to perform a characterization process, which consists of measuring the average amplitudes of the signals as a function of the input voltage.

The characterization is important because we can observe the regions where the dependence is stronger, so we need to avoid that voltage range to make sure that the measured signals are produced by the passing of the particles and not by the electronic circuitry of the PMT. This is an additional measure to ensure that the detected signals will not have a source other than the one we are interested in.

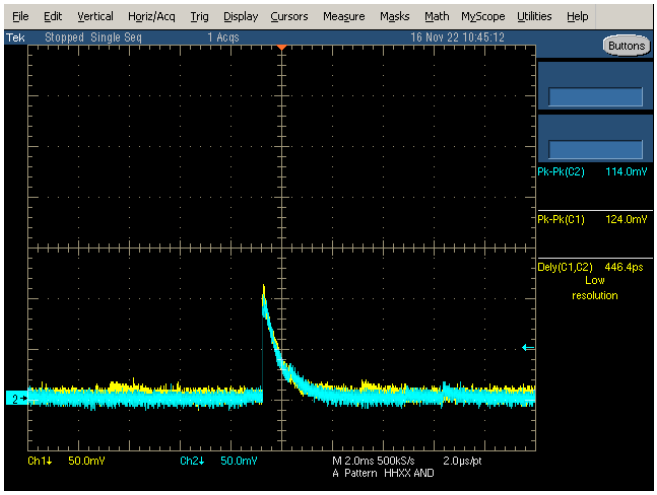

Figure 6.4: Coincidence with time delay of 446.4 ps.

Our PMTs have 2 different input voltages, the supply voltage and the control voltage. The supply voltage ranges from 5 V to make 8 V and is the one that activates the device. The control voltage is used to regulate the sensitivity and the gain of the device, it ranges from 0.3 V to 1.8 V. So we had to do two different tests. For each voltage tested we took 100 signals and reported the average of them.

The first test is to have a fixed control voltage while we vary the supply voltage. For the control voltage, we chose the center of the operating range, which is 1 V; and for the supply range, we varied it from 5 V to 7 V, in 0.2 V steps. We didn't cover the full range of the supply voltage to avoid damaging to the PMT by possible fluctuations in the output voltage of the source.

We can see the results of this first test in Figure 6.5. Even the average amplitudes vary from one detector to another, we notice that there is no significant variation of the average amplitudes, in fact, for each detector, all of the amplitudes during the whole range of applied voltage are inside the error bars, so we can say that there is no dependence between this supply voltage and the average amplitudes. We chose this voltage to be 6 V, because it is the center of the range studied and we know that there is no difference in the amplitudes over the whole range.

Now we fix the supply voltage (6 V) and we vary the control voltage in the range from 0.2 V to 1.6 V, in 0.2 V steps. Again, we don't go to the higher voltage in the range to avoid possible damage to the device. In Figure 6.6 we see that there exists a dependence between the control voltage and the average amplitudes. Signals start to appear from 0.8 V. This dependence is exponential-like, but in the middle of the

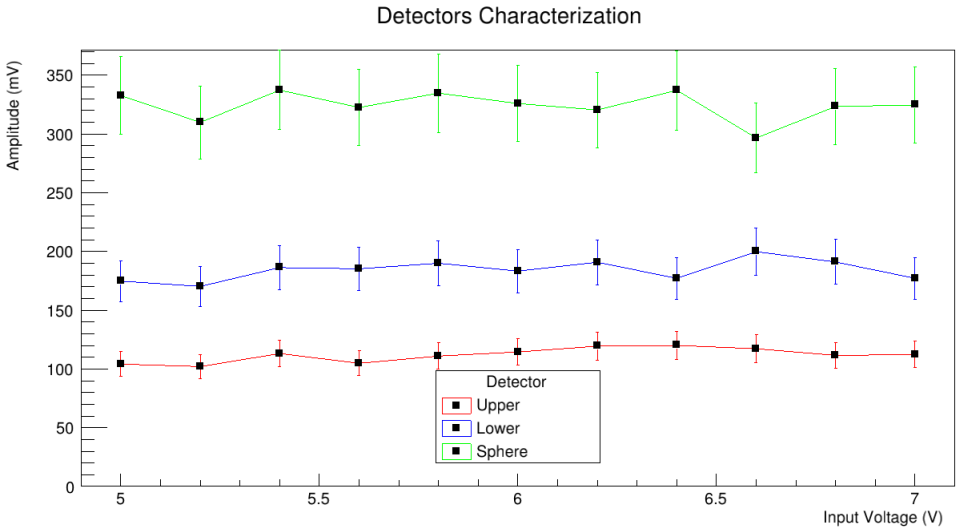

Figure 6.5: Characterization process with fixed control voltage.

range we can observe a smooth region on the curve, so this is the region we want to consider, since this dependence is not so notorious.

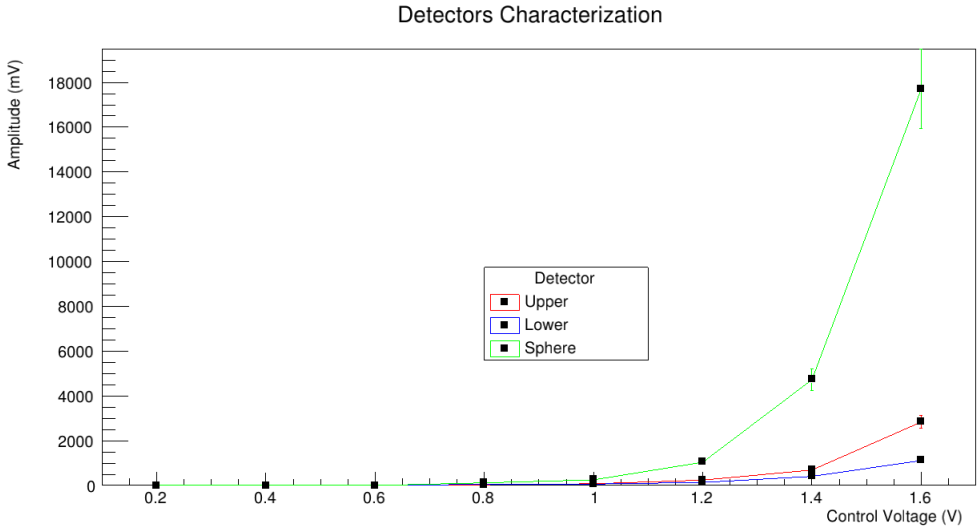

Figure 6.6: Characterization process with fixed supply voltage.

We now see Figure 6.7, where we can see the curves between 0.6 V and 1.2 V, the regions where the curves appear more like a straight line.

For the upper veto, we see that our plain region is between 0.8 V and 1 V, because the change was greater from 1 V to 1.2 V, so we now fix this control voltage to 0.9 V. For the lower detector, we see that the curve is plain between 0.8 V and 1.2 V, but

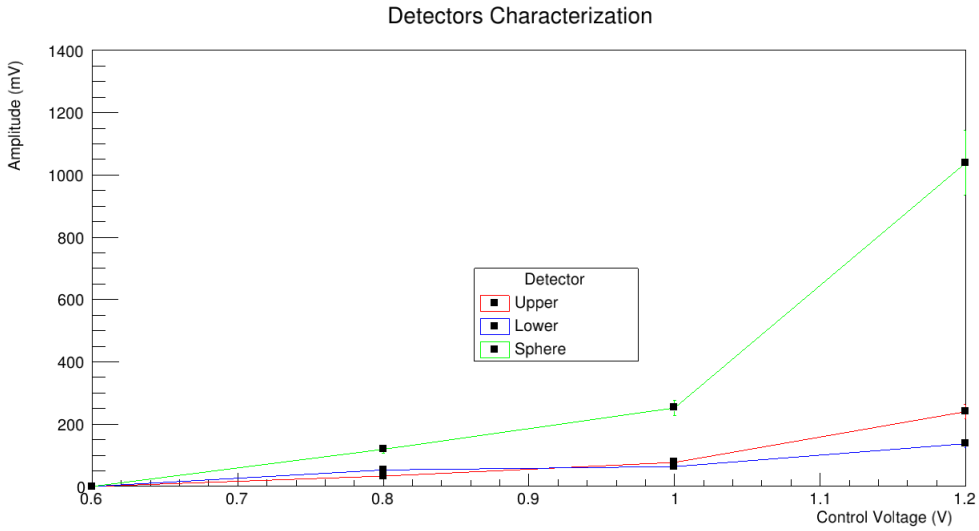

Figure 6.7: Characterization process with fixed supply voltage.

from 1.2 V it is evident that the curve is no longer linear, so we fix this control voltage at 1 V. Finally, we see that the curve of the sphere increases drastically from 1 V to 1.2 V, so it is convenient to have a low control voltage like the other two detectors. Considering the voltages we have studied, it's convenient to fix this control voltage at 0.9 V for the spherical detector.

With these voltages fixed, we expect the amplitudes of the signals from the spherical detector to be larger than those from the vetoes, as we can see in Figure 6.7. This fact will be useful when we analyze the rate of amplitudes between the events produced by the passing of gamma rays and muons.

Now that we have completed the characterization process we can proceed with the data acquisition to obtain our final results, which will be directly comparable with those from the simulation.

Chapter 7

Gamma rays flux measure

In this Chapter, we will talk about the way we will measure the flux of 2.22 MeV gamma rays, which is the main goal of this chapter.

Here, finally we can put together all of the previous processes with the results of the simulation to then propose a method of flux measurement given the considerations of the experimental system, and the physical and electronic characteristics of the measuring instruments used.

7.1 Flux

In the laboratory, we will measure a flow of particles that will be all those events that we have validated with the conditions previously exposed in the Chapter 4. We will call this flux of particles *Detected Flux* or *Measured Flux*, which is the measurement that we make directly with our detectors. This flux is simply the amount of gamma rays detected divided by the detection cross section and the time of data acquisition.

Now we must weight this measurement with the results of the simulation, i.e. we have to take into account an efficiency factor of the gamma ray detection. We must also weight this measurement with the geometric acceptance of our detector, which is the ratio of the photon detection area (PMT) to the total sphere surface. Finally, the PMT is not perfect, so it doesn't detect all of the incident light, this is another efficiency factor to consider and is given by the product manufacturer. So that the *Final Flux* will be the measured flow weighted by all of these factors, as we see in Eq. 7.1.

$$F_{Total} = \frac{F_{measured}}{(CS)(t)} \frac{1}{Det_{eff}} \frac{1}{Acceptance} \frac{1}{PMT_{eff}}. \tag{7.1}$$

where CS is the cross section of the sphere, t is the time of data acquisition, Det_{eff} is the ratio between the gamma rays events we detect and the total number

of gamma rays events, *Acceptance* is the ratio between the area of photon detection and the total area of the sphere, more precisely

$$Acceptance = \frac{\pi r_{PMT}^2}{4\pi r_s^2} = \frac{r_{PMT}^2}{4r_s^2} \tag{7.2}$$

and PMT_{eff} is the PMT detection efficiency. r_{PMT} is the radius of the PMT lens and r_s is the radius of the sphere.

7.2 Partial Calibration

By counting the number of incident photons in the PMT and comparing it to the applied voltage we can begin a calibration process, in which we will be able to relate the electrical amplitudes of the signals to the energy of the incident photons.

The procedure is as follows, we measure the amplitudes of the electrical signals on the oscilloscope. This signal is directly proportional to the number of photons incident on the PMT, which then produces the electrical signals. However, the number of electrons produced by the incident photons depends on the voltage applied to the PMT. We need to study this dependence between the applied voltage and the amplitude of the produced signals, in this way, we can then determine the relationship between the two parameters to then, in a more careful process, determine the energy of the incident particle that produced the photons in the detection media.

Method 1

To begin this study, we consider the simple circuit in Figure 7.1.

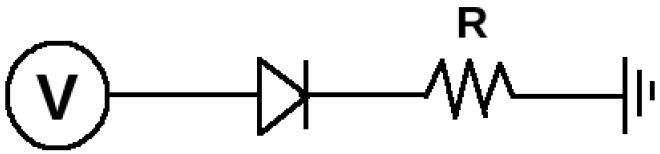

Figure 7.1: Simple circuit for LED testing.

We have a voltage source (V), and a LED connected to a resistor R. The voltage through the LED is V_D, and the voltage through the LED equals IR, where I is the

electric current flowing through the whole simple circuit.

Now, we can write the power as

$$P = \frac{\Delta E}{\Delta t}.$$

if all the energy comes from the photons produced by the LED, then

$$\Delta E = n_P E_P.$$

where n_P is the number of photons produced and E_P is the energy of each photon. If all the photons have the same wavelength, then $E_P = h\nu$, where h is the Planck constant and ν is the frequency of these photons. So, the power of the LED is

$$P = \frac{n_P h\nu}{\Delta t}. \tag{7.3}$$

Now, we can also write the power of the LED as

$$P = \Delta V_D I. \tag{7.4}$$

where V_D is the voltage drop through the diode. Combining 7.3 and 7.4 we can write

$$n_P = \frac{\Delta V_D I}{h\nu}\Delta t. \tag{7.5}$$

According to Kirchhoff, the circuit in Figure 7.1 must satisfy that

$$\Delta V = \Delta V_D + IR. \tag{7.6}$$

so $\Delta V_D = \Delta V - IR$ and we can write 7.5 only in terms of ΔV and R.

$$n_P = \frac{(\Delta V - IR)I\Delta t}{h\nu}. \tag{7.7}$$

We now have an expression to estimate the number of photons produced in the LED by the voltage applied to the simple circuit.

R and h are constants. If we choose an LED that emits a certain wavelength, then ν is also a constant. Δt is the time we turn the LED on, and we do this using a function generator. In this device, we fix a period T and we choose a value Z that represents a percentage of this period, this percentage is the one we are interested in because it is the fraction of the period T we are going to turn on the LED.

So, basically

$$\Delta t = Z\%T. \tag{7.8}$$

We have an error associated with the expression 7.7, but we will discuss this in the Appendix A.3.

Method 2

This method is based on the working principle of an LED. We know that these devices are made of two semiconductor materials, creating the region known as the depletion layer.

The energy for the electrons to recombine is provided by the power source. This energy is always less than the energy required for the electrons to recombine, this energy difference is compensated by the emission of a photon. This photon is always emitted with the same wavelength because the semiconductor materials in the LED don't change. With different semiconductor materials, the light color would be different.

The conclusion, or assumption in this case, is that for every electron recombined, one photon is emitted, so the relationship between the number of photons and electrons (related to the electric current through the LED) is one-to-one.

We can relate the number of photons to the expression for the electric current

$$I = \frac{C}{\Delta t}$$

where C is the total charge delivered by I in a time Δt. We know that the charge of a single electron is 1.6×10^{-19} C, so if we determine the total number of electrons that produce the current I, we know the number of photons as follows

$$n_P = \frac{I\Delta t}{q} \tag{7.9}$$

where q is the electric charge of a single electron. The expression 7.9 also has an associated error but we will discuss this in the Appendix A.3.
Later considerations of LED efficiency were made, we explained them in this Chapter.

7.2.1 Measurements

In both, Method 1 and Method 2, the number of photons depends on the electric current through the LED, all of the other parameters are fixed. For these tests, the frequency of the LED pulsations was 100 Hz with a duty cycle $Z = 1$, which is 1% of the total period. The voltage was applied in a range from 900 mV to 1100 mV, the

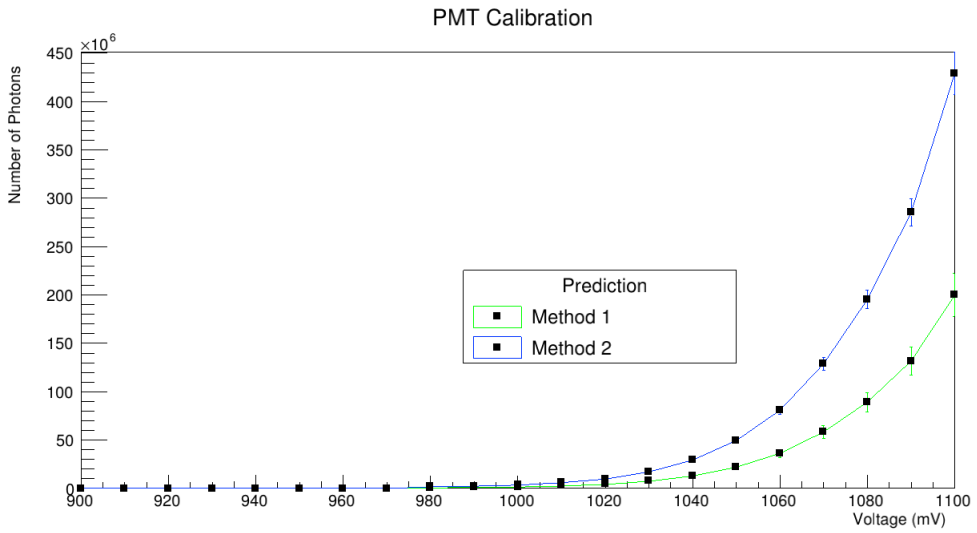

Figure 7.2: Number of photons emitted by an LED as a function of applied voltage.

resistor welded to the LED was of 100 Ω and the wavelength of the light was 525 nm (green color), and finally, the value of h is the Planck constant.

We show both graphs for methods 1 and 2 in Figure 7.2. It's clear that both plots have an exponential dependence but the amplitudes differ by a factor. Using the method of least squares we determine the value of this factor, which is 2.18108.

This difference in amplitudes is due to the fact that in Method 2 we assume that one photon is emitted for each recombined electron, so the efficiency of the LED would be 100%, which is not true. All LEDs have an efficiency of about 30% , so this would explain the difference. If we use this factor to correct the amplitude of the Method 2 graph we get the Figure 7.3.

Considering this factor, both graphs are superimposed, so, both graphs are within their error bars. Now, we need to stop talking about Method 1 and Method 2, we found that both methods worked well, considering the LED efficiency, so now we make an adjustment of both graphs to use it as our final result of the relationship between the applied voltage and the number of emitted photons.

Using the method of least squares we determine the curve that best fits both graphs, and we show it in Figure 7.4.

We now have the relationship between the predicted number of photons and the voltage applied to the LED, but we want to know the relationship between the amplitudes of the signals from the PMT and the number of photons that produced that signal.

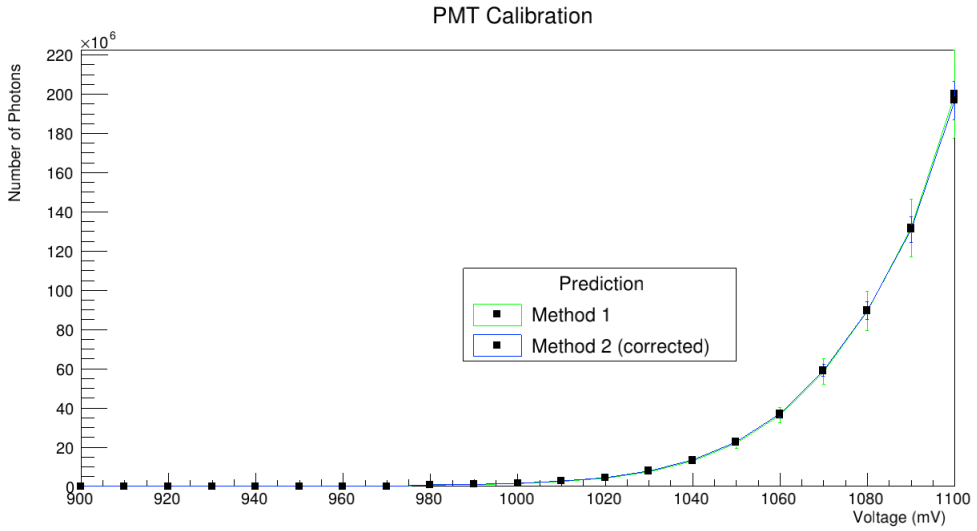

Figure 7.3: Number of photons emitted by LED as a function of applied voltage, M2 is corrected.

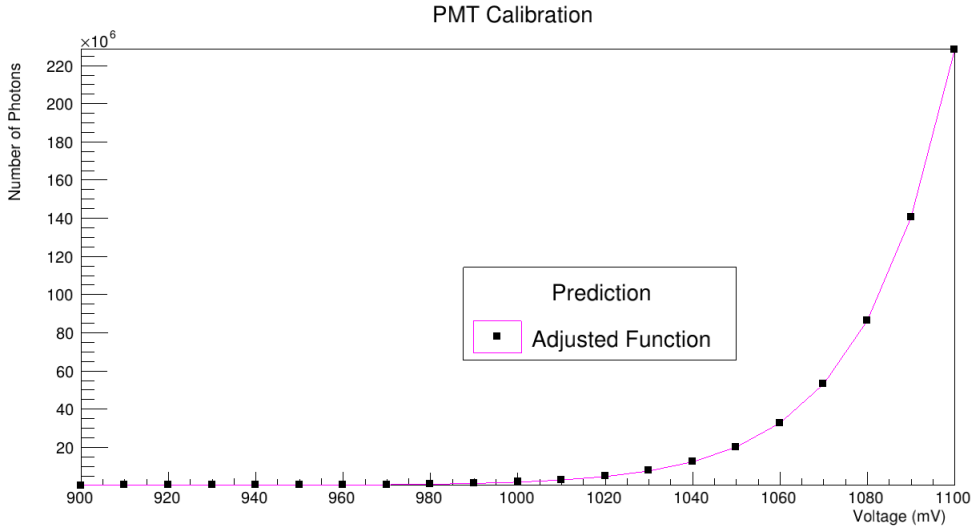

Figure 7.4: Number of photons emitted by LED as a function of applied voltage.

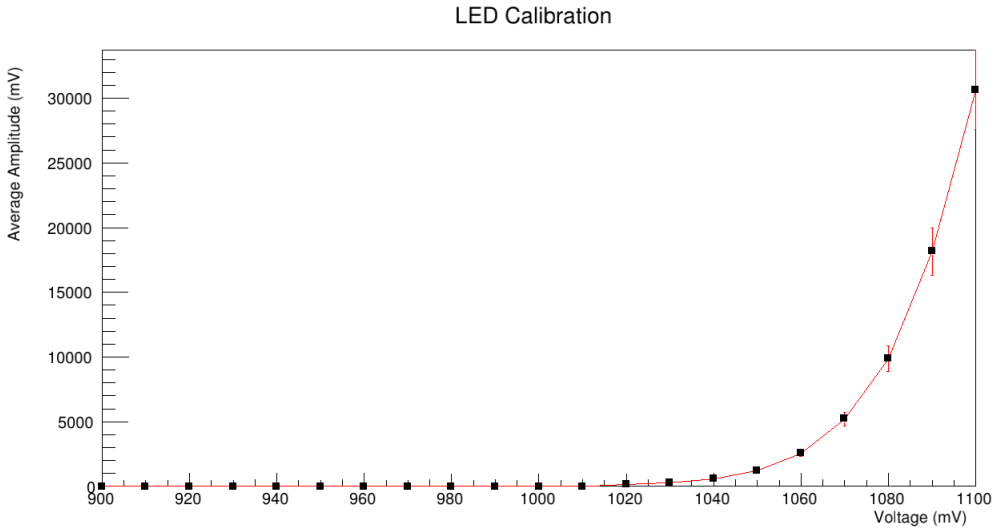

Figure 7.5: Average amplitude of signals from the PMT as a function of the applied voltage on the LED.

We placed the LED inside the sphere detector through the valve in the sphere, which we covered with aluminum tape to avoid noise. The LED was placed as close to the PMT as possible. For each voltage applied to the LED, we measured the amplitude of 100 signals on the oscilloscope and then, we reported the average amplitude of these signals. The result of these measurements is shown in Figure 7.5.

Now, we can see from Figure 7.4 and Figure 7.5 that both graphs have an exponential form and both are a function of the voltage applied to the LED. Thus, for each average amplitude in Figure 7.5, we can associate a number of photons from Figure 7.4. We expected to have a linear relationship between the number of photons and the average amplitudes, and we observe that in Figure 7.6.

Again, using the method of least squares we found the line that best fits to the points in Figure 7.6. We show this line in Figure 7.7.

And now, we are done with this partial calibration process. The relationship we were looking for is

$$n_p = 7531.56A + 3647026.11 \tag{7.10}$$

where A is the measured amplitude emitted by the PMT and n_p is the number of photons associated with that signal. This relationship is linear and has the form

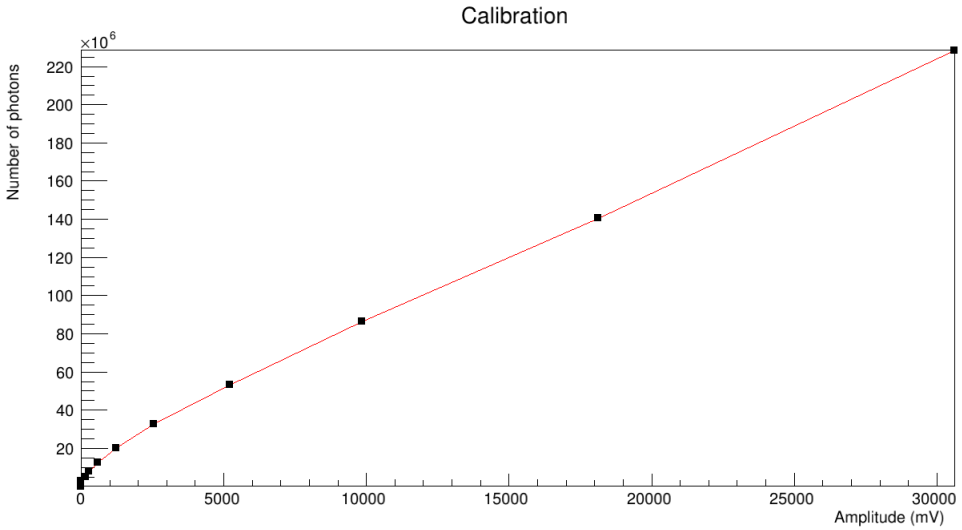

Figure 7.6: Number of photons as a function of the average amplitude of signals from the PMT.

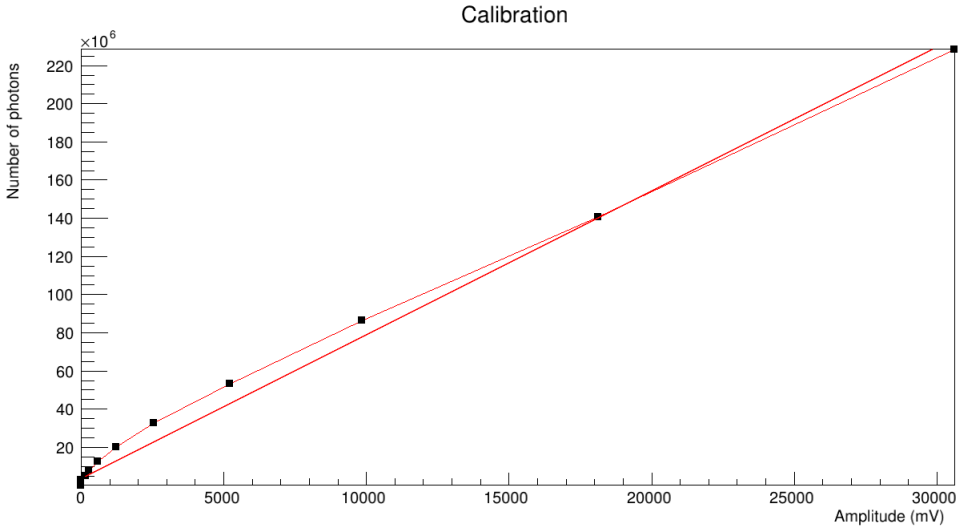

Figure 7.7: Adjust to the number of photons as a function of the average amplitude of signals from the PMT.

$$y = mx + b$$

where

$$m = 7531.56 \pm 150.045$$

and

$$b = (3647026.1095 \pm 1.22506\times)10^6.$$

The errors were obtained using Root, our data analysis software.

By observing this linear relationship between the amplitude of the signals and the number of photons we predict, we can conclude that we are detecting photons in our PMTs, in this case the source is the LED, but if we don't have this source, we are now sure that these signals are due to photons produced inside the sphere, and not due to other sources.

At the end of these tests, we were now sure that the whole experimental setup was working as expected, so we were ready to start collecting data. In Figure 7.8 we can see a picture of the whole experimental system working. Comments on the equipment used and the conditions for data collection will be explained later.

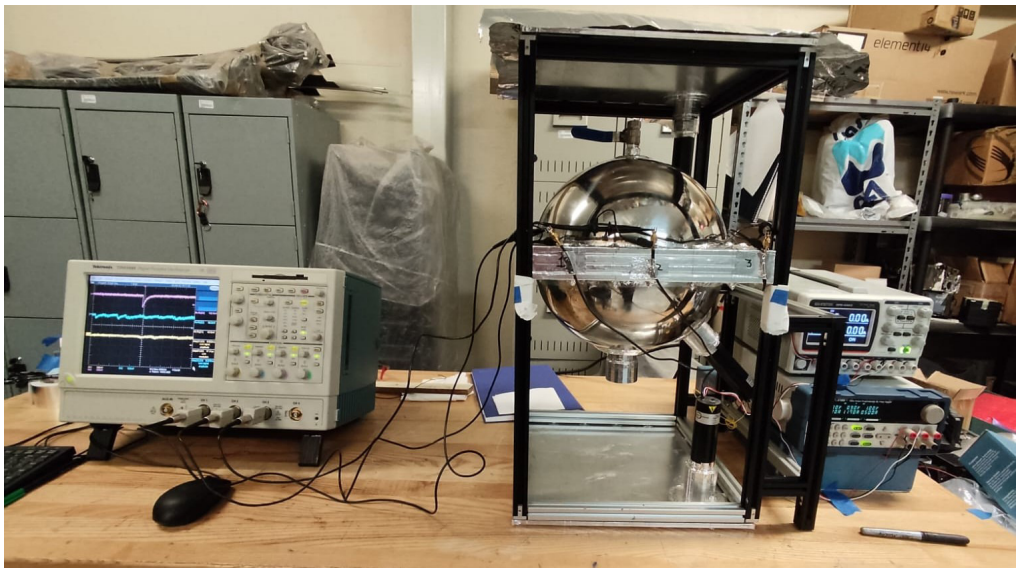

Figure 7.8: Whole experimental system working.

Signals from the upper veto usually had a larger amplitude than signals from the lower veto. In Figures 7.9 and 7.10 we can see an example of the signal in only one

of the vetoes. Channel 3 (pink) corresponds to upper veto while Channel 1 (yellow) corresponds to the lower veto.

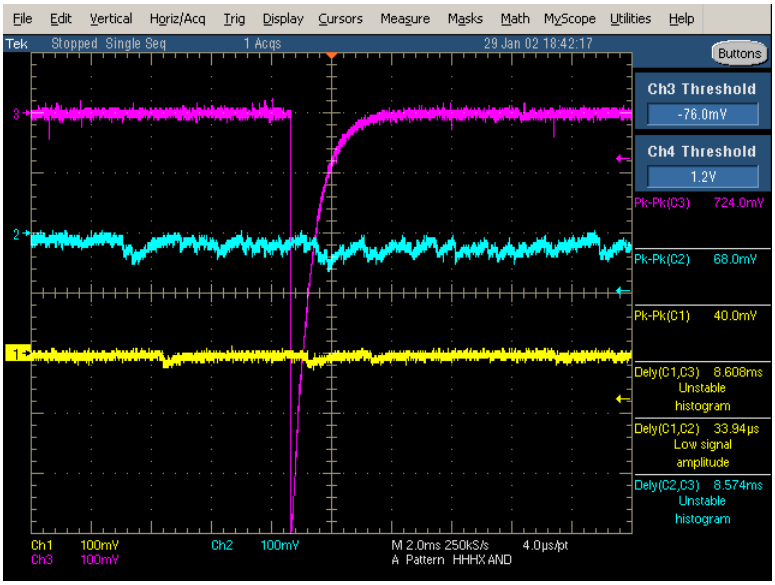

Figure 7.9: Signal only in the upper veto.

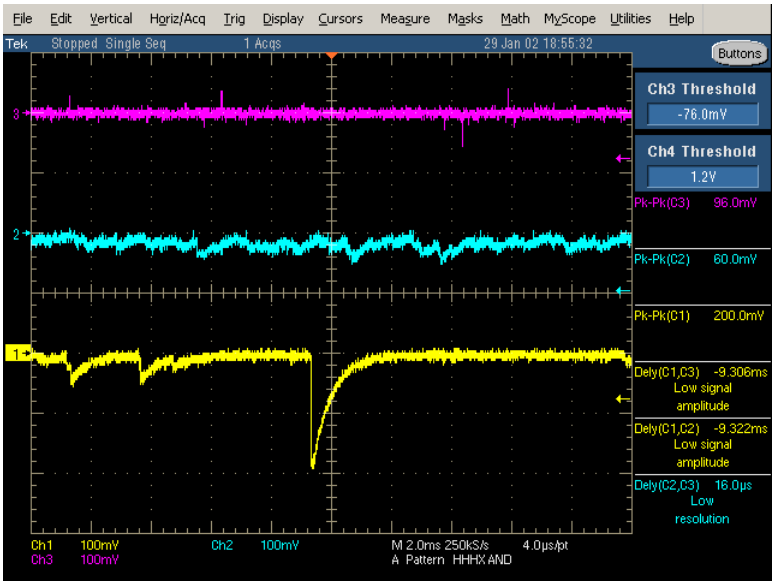

Figure 7.10: Signal only in the lower veto.

When we have signals from the sphere on Channel 2 (blue) we have an anti-veto event like the one in Figure 7.11. The amplitudes from the sphere were the larger

ones and also the frequency of the signals was greater than the vetoes. The only detail to consider was that we had a slightly higher noise level in this channel, so the trigger level we set in this channel was higher than in the vetoes.

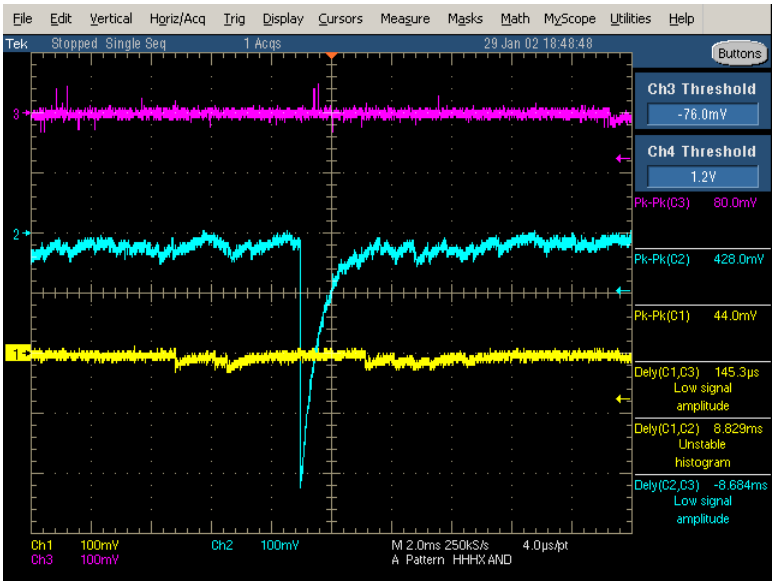

Figure 7.11: Signal only in the sphere.

Chapter 8

Results

In this Chapter, we will explain the results we got from measuring the flux of 2.22 MeV gamma rays using our experimental setup. From the planning we simulated; from the simulation we designed and constructed; and from the construction, we measured the flux of particles so that we could compare directly with the simulation results.

The efficiency corrections to determine the actual flux of particles passing through our detectors were explained in the previous Chapter 2.

8.1 Estimated fluxes using previous works

In the Chapter 2, we mentioned some previous works dedicated to measuring the flux of 2.22 MeV. Using this information, we can make a first approximation of what our actual flux will be.

In the Table 8.1 we summarize this information. It's obvious that the measured fluxes are solar related, due to an increase in solar activity; in this case the solar flares, which lead to a flux increase of 2.22 MeV. So they are produced in the Sun.

In previous works, the flux is given as

$$F = \frac{N}{A \cdot t}$$

where N is the number of particles detected , A is the cross-section of the detector, and t is the time of data collection. So, for each value of F we have to consider the cross-section of our experimental setup, which is 900 cm^2, the size of the scintillator material squared.

Note that the units of the estimated flux are photons per second, because this is the expected flux in the cross section of our experimental setup, i.e., the amount

Year	Reference	Measured flux $\frac{photons}{cm^2 s}$	Solar Flare	Estimated flux $\frac{photons}{s}$
1967	[17]	0.005	No	4.5
1973	[32]	0.280	Sí	252
1981	[33]	1.000	Sí	900
1982	[26]	0.29	Sí	261

Table 8.1: Measured flux from previous works.

of gamma rays we expect to hit our detector per second, according to the previous measurements by other authors.

So, in the case of a solar flare, there should be a significant increase in the number of events that produce signals only on the spherical detector. Furthermore, if we measure at night, we should not have a signal that satisfies this condition.

According to E. L. Chupp , there is no relevant information that we can get from the comparing of the day and night average as well as the daytime absence of any line [17]. However, our method is diferent. We can test our detector during night and compare the particle distribution results with those obtained during the day.

We will focus on the flux measured during the day but we can also compare it with the flux measured at night to make sure that these gamma rays are being produced in the sun.

8.2 Average Amplitudes

For each PMT position, we manually took 9 hours of data by looking for the two types of signals we were interested in, simultaneous signals on all 3 channels and events where we only got a signal on the spherical detector channel. Of all of the signals recorded during this time, we looked for only the best 100 ones in order to measure the average amplitudes with an error of 10%.

For the coincidence signals, the selection criteria were signals above the trigger level in all 3 channels, or at least two channels (the channel of the sphere necessarily being one of them), and short delay times, since the best signal resolutions found were in the nanosecond range. An example of a coincidence event in our experimental system is shown in Figure 8.1.

For the anti-veto signals, the selection criteria were signals above the trigger level only in the channel of the sphere, and very low noise in the veto channels. We show an example of an anti-veto event in our experimental system in Figure 8.2.

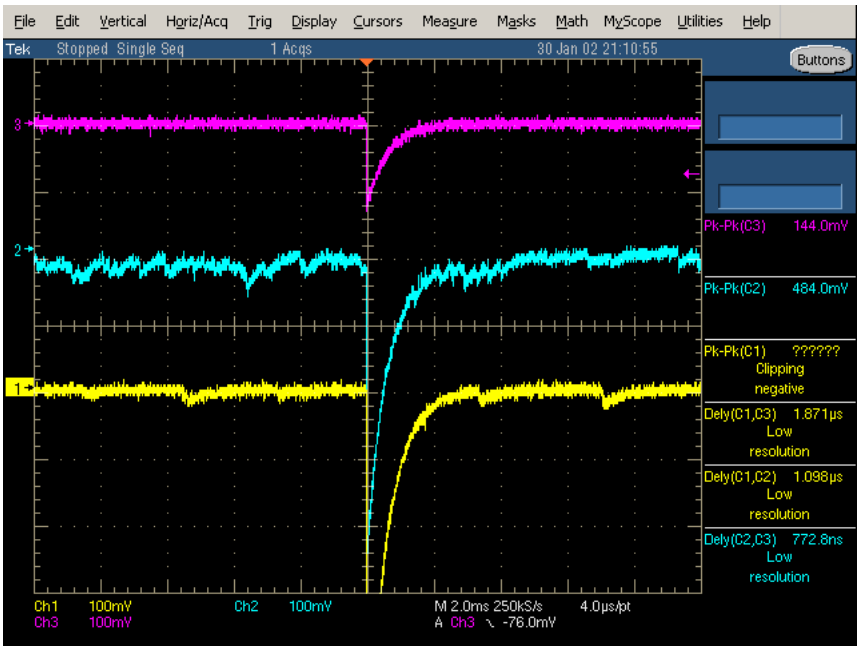

Figure 8.1: Coincidence event in our experimental system.

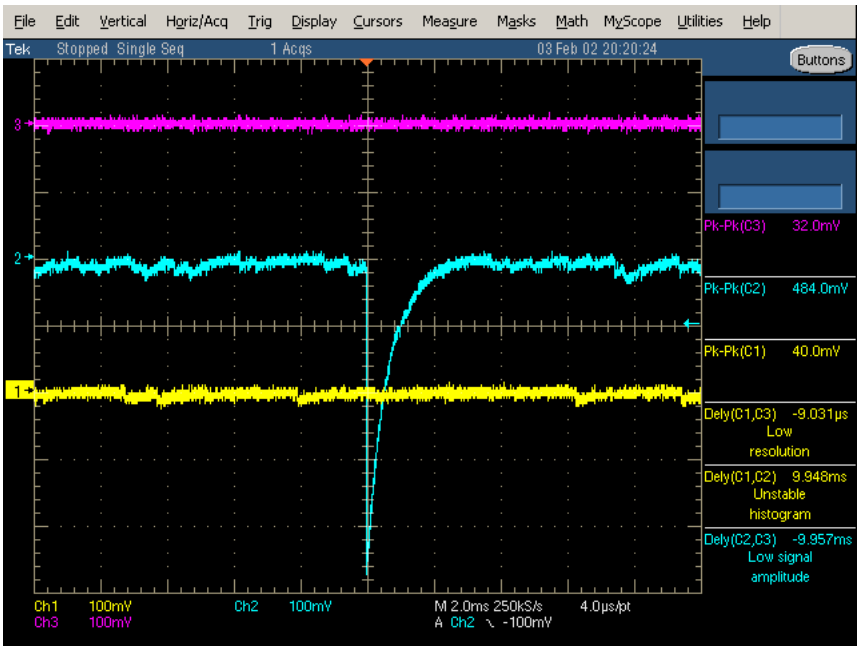

Figure 8.2: Anti-veto event in our experimental system.

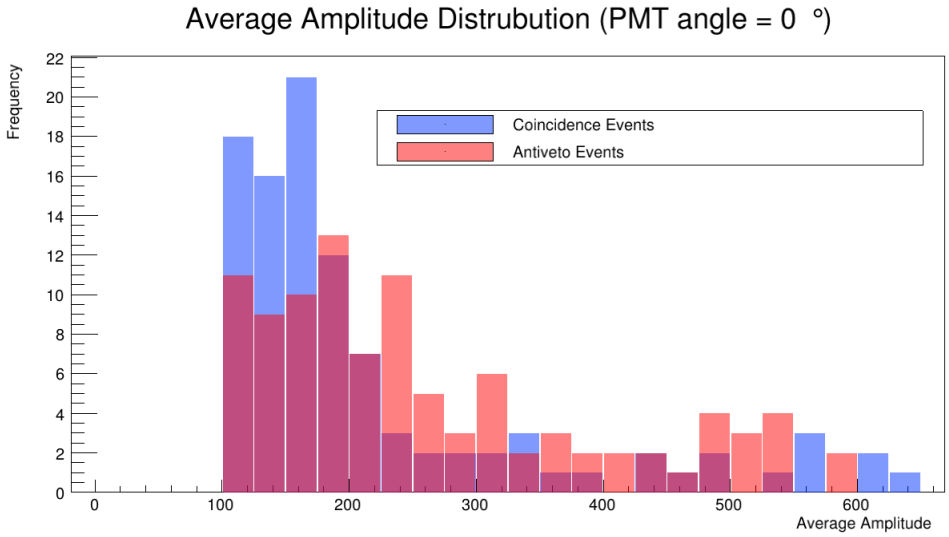

Figure 8.3: Average amplitudes distribution. PMT angle = 0°

In Table 8.2 we show the result of averaging the best 100 signals for each event type, for each PMT position. We can observe that the most intense amplitudes are from coincidence events, produced by muons. Averaged amplitudes from anti-veto events are less frequent as the amplitude increases.

Graphically, the distribution is clearer, as in Figure 8.3 for the PMT at 0° and Figure 8.4 for the PMT at 45°.

The shape of the peak distribution in Figure 8.3 is wider than in Figure 8.4, so there is a wider distribution of average amplitudes for the detected photons in this region. Basically, all of the events in Figure 8.4 are concentrated below 250 mV, so we observe a narrow peak that decays rapidly as a function of the average amplitude.

In both cases, the larger amplitudes are due to coincidence events, the most intense being detected at 45°.

To compare with the simulation results, we recall that we assume that all coincidence events are produced by muons, the most abundant charged particle at sea level. On the other hand, we have obtained that the anti-veto events are produced by muons and gamma rays, so our real task is to analyze the pink graph in Figures 8.3 and 8.4 to identify which regions of the distributions may be due to the passing of gamma rays. In Figures 8.5 and 8.6 we show the average amplitude distributions of the anti-veto events.

Let's recall that from the simulation results we obtained the ratio between the average energy of the photons produced by the passing gamma rays and the muons. For the case where the PMT is placed at 0°, this ratio is 2.021, since the average energy of the photons produced by the muons is greater. For the case where the PMT is placed at 45°, this rate is 2.100.

Average amplitudes frequency				
	PMT angle = 0° Events		PMT angle = 45° Events	
Amplitude (mV)	Coincidence	Anti-veto	Coincidence	Anti-veto
1 - 25	0	0	0	0
26 - 50	0	0	0	0
51 - 75	0	0	0	1
76 - 100	0	0	15	19
101 - 125	18	11	21	25
126 - 150	16	9	25	17
151 - 175	21	10	6	15
175 - 200	12	13	10	6
201 - 225	7	7	3	5
226 - 250	3	11	3	2
251- 275	2	5	4	4
276 - 300	2	3	3	1
301 - 325	2	6	1	1
326 - 350	3	2	1	0
351 - 375	1	3	3	1
376 - 400	1	2	1	0
401 - 425	0	2	0	1
426 - 450	2	2	1	0
451 - 475	1	1	1	1
476 - 500	2	4	0	1
501 - 525	0	3	0	0
526 - 550	1	4	1	0
551 - 575	3	0	0	0
576 - 600	0	2	0	0
601 - 625	2	0	0	0
626 - 650	1	0	0	0
651 - 675	0	0	0	0
676 - 700	0	0	0	0
701 - 725	0	0	0	0
726 - 750	0	0	0	0
751 - 775	0	0	1	0
776 - 800	0	0	0	0

Table 8.2: Averaged amplitude of 100 events for each PMT position.

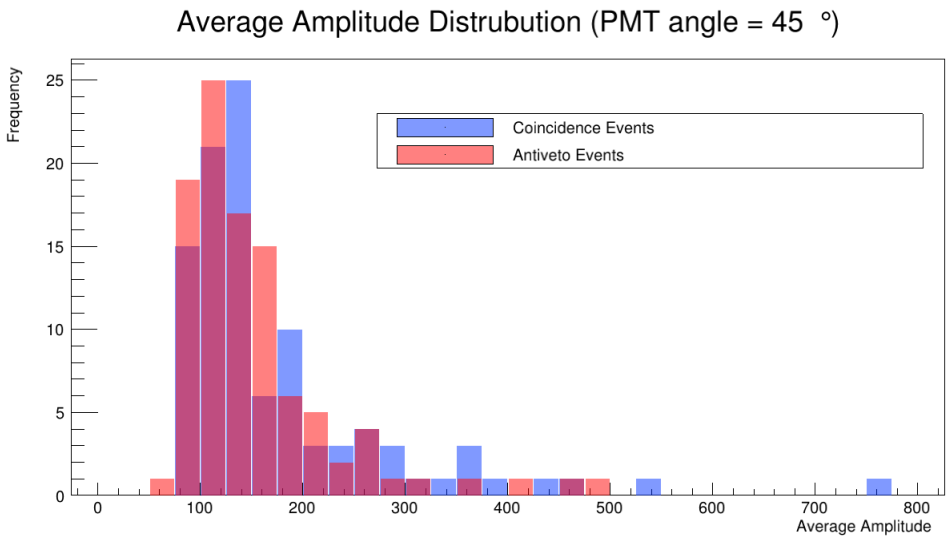

Figure 8.4: Average amplitudes distribution. PMT angle = 45°

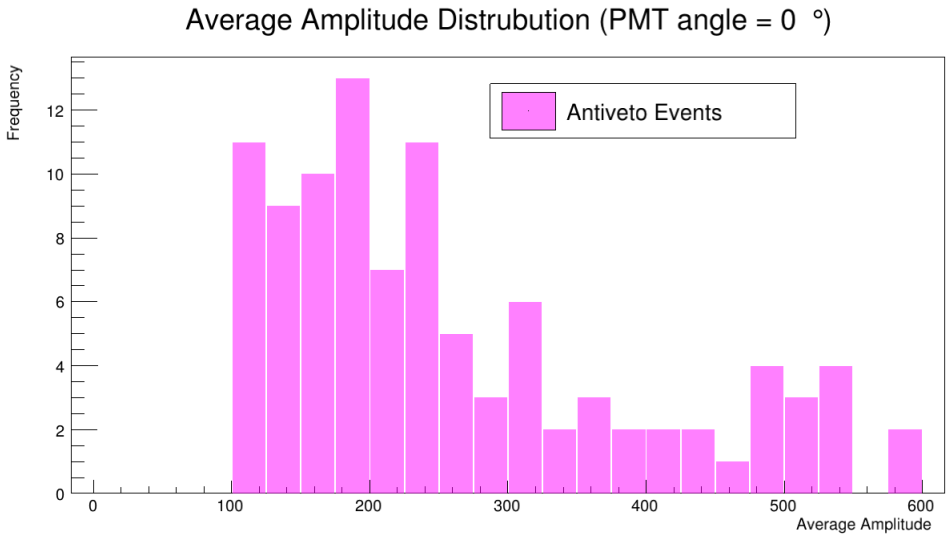

Figure 8.5: Average amplitudes distribution of anti-veto events. PMT angle = 0°

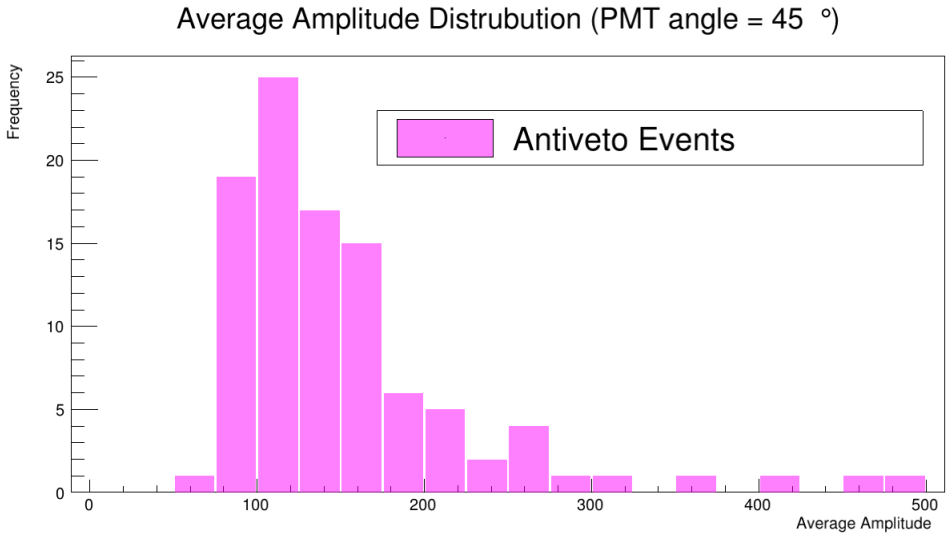

Figure 8.6: Average amplitudes distribution of anti-veto events. PMT angle = 45°

Thus, if the fluxes of both primary particles were equal, the average energy of the photons produced by the passing of muons would be twice the energy of the photons produced by the passing of gamma rays. Let's recall that the energy of the photons produced by the passing of gamma.

8.3 Shape Comparison

First, it was necessary to normalize all of the graphs to be compared, that is, the two graphs with our laboratory data and the four graphs with the simulation data. So we had to divide each bin value by the total number of data we got for each case. The error in our data also had to be normalized.

What we did was compare the shape of the distribution for each angle (0° and 45°) with the results from the simulation when we shot gamma rays and muons, for each angle. So, we have four graphs to analyze.

On the horizontal axis, we put arbitrary energy units just to compare both distributions in each case. We can do this because our data results are in function of the signal amplitudes which are directly related to the energy photons deposited on the PMT.

We will first compare our data distributions with the simulation results for the gamma ray case, for each angle. First, let's look at the Figure 8.7. Ideally, the two

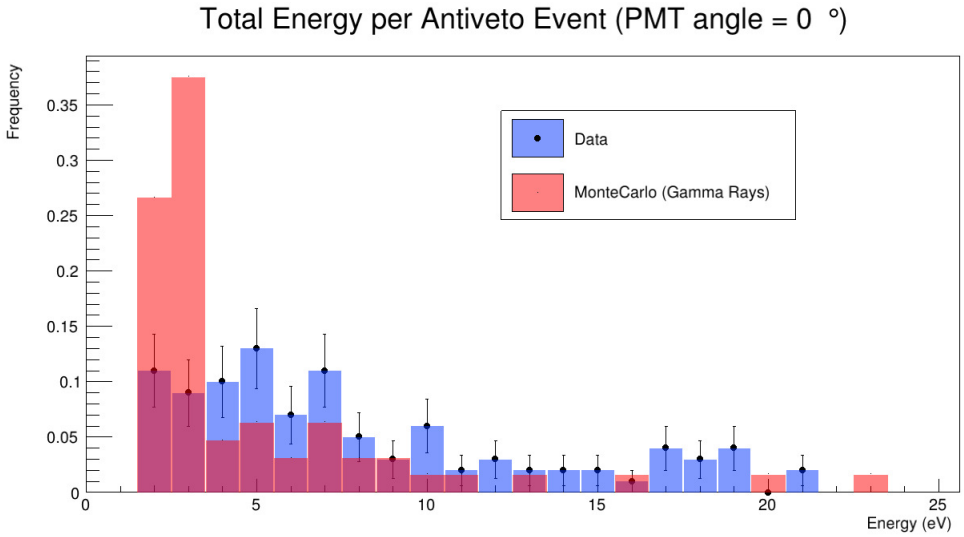

Figure 8.7: Our data distribution vs photons produced by the passing of gamma rays energy distribution. PMT angle = 0°

graphs should overlap. Our reference is the pink colored graph, it shows the probability distribution of detecting particles for each energy range. So, we can see that we have a high probability that the particles detected in the first two bins are the gamma rays we are looking for, but since the blue colored graph has a low data concentration on those first two bins, we can think that we are not detecting the number of gamma rays we expected from the simulation. In fact, we can see that at intermediate energies, we are detecting a significant number of particles in the lab and the blue colored graph outperforms the pink one, so we are detecting more than expected in this region. This is because we have other contributions to the distribution that we are measuring. So, for this first graph, the two distributions partially correspond.

We now look at Figure 8.8. At 45° it is obvious to the naked eye that we have a better match between the two distributions, the shape of them is more similar. Note that the probability of detection increases in both distributions compared to the 0° case. The larger bins in the blue graph are also the larger bins in the pink graph. For the pink graph, about 65% of the data is concentrated in the first two bins, while for the blue graph about 45% of the data is concentrated in these two bins. We also note that, unlike the other case, the blue graph decays rapidly as a function of energy, which is directly related to the pink graph where only a few high energy cases were detected.

At this point, we can say that we have detected photons produced by gamma rays with a higher probability at 45^0 for the low-energy region.

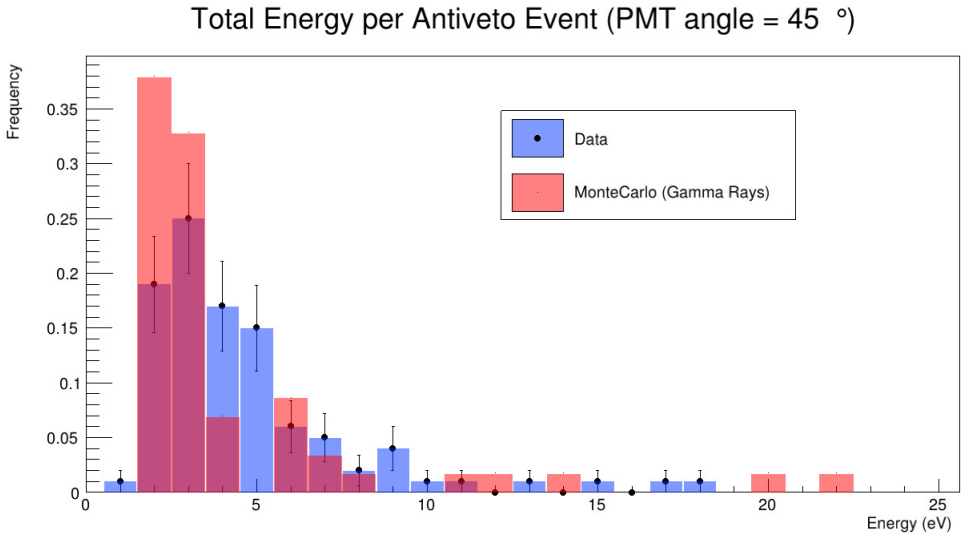

Figure 8.8: Our data distribution vs photons produced by the passing of gamma rays energy distribution. PMT angle = 45°

Now we need to compare our data with the Monte Carlo results when we have incident muons. At 0^0 we observe the distributions in Figure 8.9.

In this case, we can see that we have a better overlap between the two distributions along all of the energy ranges. This is a good indication that in our data we have a contribution of photons produced by muons, especially noting that the mid-energy region fits much better than in the case of photons produced by gamma rays. Furthermore, is evident that both distributions have the same shape, and the only region where our data exceeds the data from Monte Carlo is in the low-energy range, so considering also Figure 8.7 we can say that our probability of detecting photons produced by gamma rays is greater at low energy (for both observed angles); and in the mid-energy range we have more probability of detecting photons produced by muons at 45°, just as expected from the previous simulation results.

Finally, we have Figure 8.10. Let's remember that when we shoot muons, the energy range covered by the photons produced is very large. In this case, we expected not to have a good correspondence between the two distributions because having a wide range of available energies and a large amount of photons produced in our simulation, implies that our normalized data will have very small values, even though having a greater probability at lower energies, a usual.

Once again, comparing with photons produced by muons we observe that our data exceed the simulation data in the low-energy range, this implies that the probability of detecting photons produced by muons in this range is very low, so we have

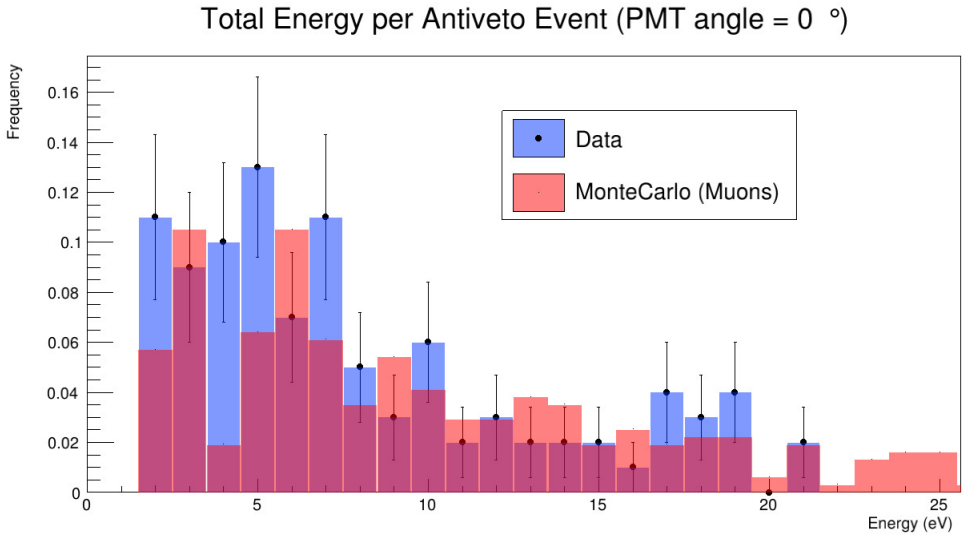

Figure 8.9: Our data distribution vs photons produced by the passing of muons energy distribution. PMT angle = 0°

contributions from other incident particles.

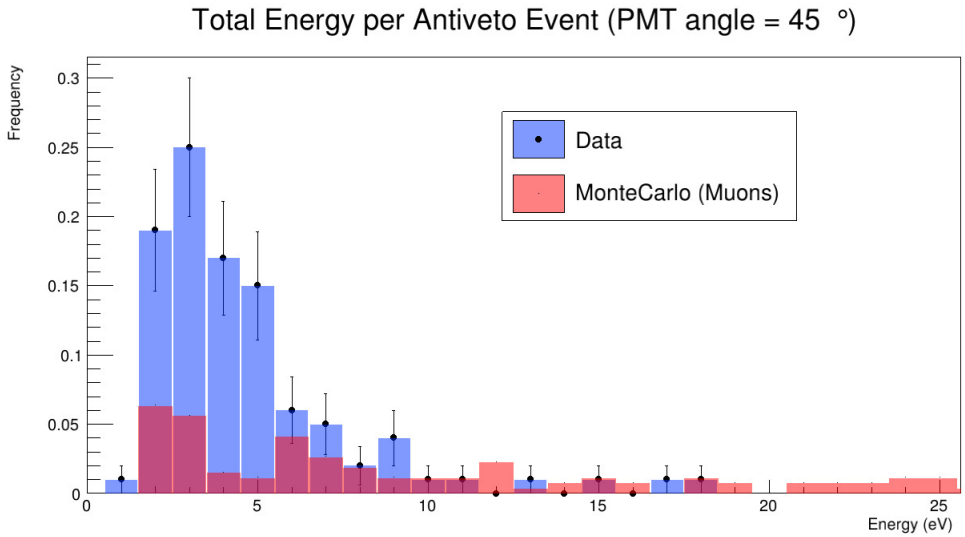

Figure 8.10: Our data distribution vs photons produced by the passing of muons energy distribution. PMT angle = 45°

8.4 Flux of Gamma Rays

Finally, we report the flux of gamma rays we detected in our experimental setup.

Recall that for each PMT position we manually took 9 hours of data, capturing signals that satisfied the coincidence or anti-veto condition. For the purposes of this work, we would only report the flux of gamma rays, which is the particle we are interested in.

From the previous Chapters, we have determined the characteristics of the signals produced by the incidence of gamma rays, and we have compared probability distributions with our energy distributions to determine the similarities of our distributions with those predicted by the simulation.

However, in order to measure the flux, we have to assume that all of the detected signals that satisfy the anti-veto condition are due to gamma rays, or more specifically, 2.22 MeV gamma rays. This is the best we can do at the moment, given the conditions under which the data were taken.

It is necessary to recall the equation 7.1, to make this result clear, we will show it again.

$$F_{Total} = \frac{F_{measured}}{(CS)(t)} \frac{1}{Det_{eff}} \frac{1}{Acceptance} \frac{1}{PMT_{eff}}. \tag{8.1}$$

At 0° we recorded 116 gamma-like signals, while at 45° we recorded only 101 gamma-like signals. So, $F_{measured}$ will take any of these values depending on the case we are looking at. CS is the cross section of the sphere, $225\pi\ cm^2$, while t is 9 hours for each case.

Since we have a detection efficiency distribution for the PMT, we consider an intermediate point in its wavelength detection range, which is about 450 nm. The PMT efficiency is 0.27, as stated by the manufacturer [38].

Now, for the purposes of our detection efficiency study, we only consider the detected 450 nm photons in our simulation, so we take into all 5 study cases we made and we average the number of these photons we detected, this result is 1.2 gammas. To be consistent with the particle we detected, we will consider the average as 1 gamma, so the detection efficiency is 1/1000.

The acceptance was given by eq. 7.2, we only need to consider the radius of the sphere and the radius of the PMT lens.

So, taking into account all these corrections, we can finally report in Table 8.3

the final flux, which is the real incident flux in our experimental system, now taking into account the photon losses through the PMT, the detection efficiency and the geometrical correction.

PMT Position	Gamma Rays Flux ($\frac{gammas}{cm^2 s}$)
0°	11
45°	9

Table 8.3: Flux of gamma rays measured in our experimental system.

On average, we can say that we measured a flux of 10 $\frac{gammas}{cm^2 s}$ in our experimental setup.

These results will be further discussed in the next Chapter.

Chapter 9

Discussion and Conclusions

We have planned, designed, simulated, constructed, tested and partially calibrated a gamma ray detector. We are not limited to detecting only this type of radiation, we can also detect charged particles with very good efficiency. In fact, we have used two different detection media in three detectors, so the fact that we have validated these signals by the coincidence method is a good indicator that we are detecting cosmic rays, in general.

The design is unique, there's no evidence of a gamma ray detector like the one we made, not even in the detection technique or the detection media. The planning and design of the project required the use of two different design software, AutoCAD and SketchUp.

For the simulation we used Geant4 software with C programming language. To make all of the graphics we used Root, developed by CERN. With the simulation, at this point, we can easily study different properties of the photons produced in our experimental setup due to the incidence of different primary particles, we can also change dimensions, positions, materials, etc. From the simulations, we can also get direct graphs and text files for different purposes, so it was and still is a very powerful tool to study the way particles interact with our experimental setup. And even so, modifications and improvements can be made.

To construct, we used many tools for different tasks, including cutting, gluing, welding, covering, polishing, cleaning, screwing, assembling, insulating, drilling, filling, vacuuming, aligning, measuring, painting, sanding, and many others. Careful work is directly related to the quality of the results obtained .

The testing of the entire experimental setup required the use of several devices, which we briefly mention in the Appendices A.4 and A.5. These devices were used to power the PMTs and LEDs we used, to measure voltage and current amplitudes, to

apply a function to evaluate the operation of other devices and to observe the shape of various signals. Putting it all together, we characterized and partially calibrated the experimental setup.

Acquiring data with an oscilloscope is something we can improve, we need to automate the data acquisition. But the resolution of that oscilloscope is optimal to detect very fast events, as we predict we have with the simulation results. Even so, the manual data acquisition was good enough because we were capturing not only the signal amplitudes but also the delay times between signals on different channels.

The noise level we measured in all three detectors was very low compared to the amplitude of the signals. As usual, we set the trigger level to three times the measured noise amplitude to ensure that the validated signals were not due to noisy sources. It is noteworthy that we observed clear signals in all three channels even though we didn't put the entire experimental setup in a black box to isolate it from daylight. This fact is a good signal that our detectors are well isolated and that the detected signals correspond to incident cosmic rays.

We have two types of results to discuss, the simulation results and the laboratory results.

From the simulation results, we basically concluded that our experimental setup works to detect not only 2.22 MeV gamma rays but also charged particles such as muons. We detect the photons produced by the incident particles in our experimental setup, i.e., we don't detect the muons or gamma rays directly but the results of their interaction with matter.

We could verify that simple water could be used to detect gamma rays, and we could also discard other elements as detection media, such as air.

Not only did we know that this detector would work, but we also knew the direction in which these photons were more likely to travel, their properties, and the conditions we needed to identify whether the photons were produced by muons or gamma rays.

Charged particles produce signals in both the vetoes and the sphere detectors; while gamma rays can only produce a signal in the sphere detector.

From now on we will talk about the characteristics of the photons produced in the sphere by muons and gamma rays, this is because the sphere is our main detector and is the key to knowing the identity of the incoming particles.

The number of photons produced by muons is much greater than the number of

photons produced by gamma rays in the water. Photons produced by both, muons and gamma rays, have the same wavelength distribution, are produced by the same forms, and have the same ratio, with the Cherenkov effect being the most dominant form of production compared to the photons produced by scintillation.

Photons produced by gamma rays are more likely to disperse in the direction of the incident particle, while photons produced by muons disperse mainly in the shape of a cone with its edge at some point in the trajectory of the incident muon. Observing the spatial and angular distributions of the photons, we concluded that we have a greater chance of detecting photons produced by gamma rays at 0° (or small angles) from the vertical and the maximum peak of detection for photons produced by muons is at 45° from the vertical. We need to keep in mind that in any case, we always have a greater amount of photons produced by muons than by gamma rays.

A particle traveling at the speed of light traverses the entire experimental system in 2 ns. We verify this fact with the simulation by measuring the time delays between the detected signals in all three detectors. We concluded that for the coincidence method, we need to consider a very small time window of 5 ns, which would be enough time to validate the passage of charged particles. As an independent test, we also verified that our best coincidence validation efficiency is at 0° and 45°.

As we said before, if the coincidence method is satisfied, we can associate that event with the passage of a muon. If we detect only a signal in the sphere detector, that signal could have been produced by a muon or a gamma ray. We will now present the conclusions of studying the photons validated in events where the anti-veto condition is satisfied, i.e., events where we had signal only in the sphere detector and not in the vetoes.

We have a better chance of identifying the identity of the incident particle at 0° and 45°, that is because of the ratio between the number of events satisfying the condition for each one of the incident particles and the number of photons produced in each case. At 0° the rates are minimal, and at 45° the rates are maximal.

By measuring the average energy of photons validated by the anti-veto condition when shooting muons or gamma rays, we predicted that the average deposited energy of photons produced during a muon event would be twice the energy of photons produced during a gamma ray event.

The energy distributions obtained for each incident particle for each angle we studied are the ones we directly compared with the results in our laboratory. Previous simulation results were used to verify the work of our proposed experimental setup and to determine the configurations we would need to achieve our goal.

Now, we present the results of the laboratory.

After characterization and partial calibration, we confirmed the functionality of the entire experimental setup. We detected very frequent signals in all three channels. If we were to manually acquire data on each channel, we would detect about one signal per second.

We noticed that we detected more signals in the morning than in the afternoon, so we took all of our data before noon. We collected 9 hours of data for each PMT angle, and, to have better control over the amount of data, we only selected the best 100 signals for events satisfying the coincidence method and 100 for the anti-veto condition. We then examined the amplitudes of the validated signals to obtain the distribution in our data.

Looking at the laboratory distributions, we can see that the simulation results were correct and corresponded to the signals we detect in our experimental setup. Looking at the shape of the distributions is the strongest evidence we have to compare the simulation results with the laboratory results.

We have a high probability that the low energy signals we detected were produced by gamma rays. We also have a high probability that the high-energy signals were produced by muons.

The most intense signals are also the least frequent, but they span a wide range of the distribution, we can directly associate these signals with the passage of muons. When we observe the distribution of the photons produced by gamma rays in the simulation, we note an increase in the detection probability that we also detect in our laboratory data.

The shape of the graphs is conserved in all 4 cases, we have very high and narrow peaks at 45° while the peaks are lower and wider at 0°, so we have a contribution from photons produced by both gamma rays and muons. However, we may also have a contribution from other particles that we didn't study in this work.

We need to mention possible reasons why the Monte Carlo and laboratory distributions didn't fit exactly.

We started our simulations by shooting only 2.22 MeV gamma rays and 4 GeV muons, but we know that even if these are the most likely energies of the primary particles, we actually have energy distributions due to energy loss as they interact with the Earth's atmosphere and particles in the outer space.

We also shot the particles uniformly at our detectors, but only in a vertical direction forming a 0° zenith angle. We know that particles come from all directions and we also know that these particles are more likely to come from the top down, but in a range of angles that don't necessarily have a 0° angle of incidence.

Other factors to consider are the water composition and water attenuation, PMT efficiency, photon leakage inside the sphere, oscilloscope resolution, DAS (Data Acquisition System) resolution, and finally, the lack of 24-hour data to compare day and night distributions.

To consider the PMT efficiency we could modify the simulation to detect different wavelengths with different efficiencies, since what we did was to consider the efficiency of all wavelengths to be the same. We can see the real efficiency of the PMT as a function of wavelength in Appendix A.2.

Data acquisition with DAS was not convenient because we are studying very fast events, with a duration of nanoseconds, and the DAS resolution is milliseconds, so we would lose a lot of information by using it, so it would not be enough to have our background and then better identify our events produced by incident gamma rays. However, it would be the first test to continue analyzing the data from the spherical detector and compare it again with the Monte Carlo results.

Finally, we need to make some remarks about the measured flux of gamma rays.

At 0° and 45° we measured fluxes of 11 $\frac{gammas}{cm^2 s}$ and 9 $\frac{gammas}{cm^2 s}$, respectively. This is larger than previous results and it only works as a primary measurement of the 2.22 MeV gamma rays flux by a factor of about 10 (compared with the most recent results).

Again, we have to mention that since we took the data manually, we lost a lot of information about the incoming particles due to the speed of the events. At this point, we could only compare our laboratory distributions with the simulation distributions, but we could not determine exactly how many of the anti-veto events were produced by muons or gamma rays.

For the flux measurement, we assumed that all of the anti-veto signals detected in all 9 hours of data acquisition were produced by gamma rays, and that is why we can report this numerical result. Of course, this is our strongest assumption and this is the reason why our flux is larger than previously reported by other authors, but it is the best we can do at this time to report a gamma ray flux measurement.

The fact that this flux is consistent with previous results by other authors is a good signal that our estimate may not be exact, but it is very close, and that makes

sense, especially considering that for this result we considered not only our laboratory results, but also the simulation results. Finally, we took only one of the PMT quantum efficiency values, and that was for the color blue. Since we detect in all visible colors, we need to consider the whole function of efficiencies to get more accurate results, but given the correspondence between the frequency of the blue photons produced and the maximum quantum efficiency for that color, this result is a good approximation of what we are really detecting.

Otherwise, we have considered geometric acceptance, which can be improved by using more PMTs at the same time or by using larger PMTs. The choice will depend on our specific goals.

Our detectors are working as planned and we have been able to directly compare our laboratory results with the simulation results. The spherical detector is our main detector, we list its main advantages.

- **Shape.** It is easy to measure the angular distribution in this way, even though we only measured from two different angles.
- **Size.** The detector is only $\sim$ 60 cm high and $\sim$ 34 cm wide. It's very small compared to the water-based detectors used in the Kamiokande and HAWC experiments. When our detector is filled with water, it can be moved by two people, when it's empty it can easily be moved by a single person.
- **Detection media.** Due to the construction of the sphere, we can change the detection media for testing. The results of the simulation were obtained using pure water as the detection medium, but if we want to change this material in the simulation we can also do it in our sphere by using its valve. We can use any liquid material and, with some additional considerations, we could use gases as well.
- **Operating Voltages.** We don't need huge power sources, the maximum voltage we used to operate the detectors was 7 V, but when taking data we feed them with a maximum of 6 V.
- **Simulation.** At this point, the simulation is finished and ready to be modified in order to take data with different considerations than the ones we made for this work.
- **Calibrated detector.** The spherical detector is partially calibrated, we could improve this process by using different LEDs. This calibrated detector is the key to studying more particle properties because we can try to identify different incident particles in our experimental setup just by analyzing their amplitudes.

This detector and the instruments needed to manipulate them are available at the Elementary Particles Laboratory of the University of Guanajuato, so it would be used by new students to learn about gamma rays and charged particle detection.

Appendix A

In this Appendix, we talk about the materials and devices we worked with during this project, all of which were not built in the lab. For each one of them, we mention only the features relevant to our work. We also briefly explain how we measured the error in measuring the number of photons as a function of the applied voltage.

All of the equipment mentioned is available in the laboratory where this work was done.

A.1 Scintillator plastic

We used two pieces of green acrylic (PMMA) sheets for our veto detectors. The exact dimensions of these pieces are 30.48 cm $\times$ 30.48 cm, 3 mm thickness. Since this is not a material designed for scientific purposes there is no exact information about the emission wavelength of the acrylic and the rise and fall times of the emitted signals.

We worked at room temperature all the time, so we didn't have to consider any other specifications when working with this product. The sheets were covered with a film on both square faces, and we took special care when removing it and placing it on the vetoes to avoid contaminating the acrylic.

Other specifications are available on the website where we purchased the plastics [37].

A.2 Photomultiplier Tube

We used the photodetector module from the P30CW5 series made by Sens-Tech. The effective diameter of the photocathode is 25 mm, and the outer diameter of the tube is 35 $\pm$ 0.5 mm. The length of the tube is 161.5 $\pm$ 1 mm and the connecting wires measure 450 $\pm$ 50 mm. There are 5 connecting wires

- Signal Output.
- Control (White).
- Set Voltage (Yellow).
- Input Voltage (Red).
- 0 V (Black).

There are two modes of operation for this unit. One is to use an external power source and connect it directly to the control voltage wire (white wire). In this mode, the yellow wire remains isolated. The other mode uses an internal variable resistor of the PMT, in this case, we connect the white and yellow wire to a monitor to measure the control voltage.

The control voltage is used to adjust the sensitivity of the PMT, i.e. to increase the gain of the signals for all of the wavelengths while maintaining the quantum efficiency observed in Figure A.1.

The input voltage is to activate the device, the input must be 5 V. The black wire is connected to the ground and is used as a reference for the input and control voltages.

When operating the PMT, the temperature must not exceed 55^{o}C and must not be lower than 5 ^{o}C. When storing the PMT, the temperature must not exceed 55^{o}C and must not be lower than -40^{o}C.

The wavelength detection range is also observed in Figure A.1, as well as the peak of detection sensitivity which is around 350 nm (violet).
For other specifications, you can check the official website of the manufacturer.

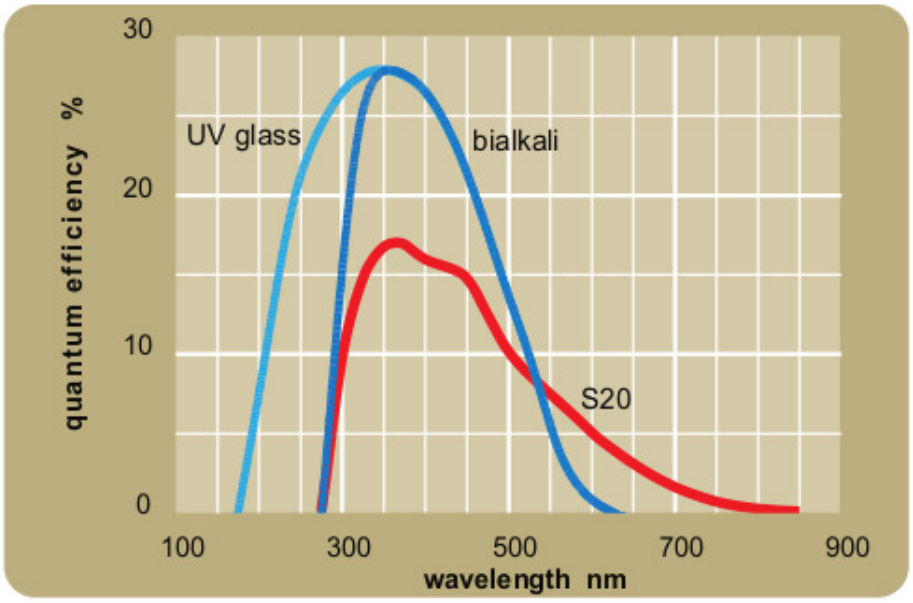

Figure A.1: PMT efficiency [38].

A.3 Error Measurement

The errors reported in the Chapters 6, 7, and 8 were measured as described in this section.

General formula for error propagation

We have a function f with a number n of variables x_i, its associated error is

$$\Delta f = \sqrt{\sum_{i=1}^{n} \left[\left(\frac{\partial f}{\partial x_i} \right) (\Delta x_i) \right]^2}. \tag{A.1}$$

With A.1, we can observe that the total error of this function f depends on partial derivatives of itself with respect to each of the variables on which it depends. It's important to note that for each one of the variables on which f depends we must know the error associated with each one of them. In the end, each variable error will contribute to the total error of f [39].

Errors in measuring lenghts

All length measurements were made using a ruler with resolution of 1 mm. Thus, all errors associated with length measurements in this work are $\pm$ 0.5 mm.

Error in the estimated number of photons produced in calibration process

Method 1

The expression for estimating the number of produced photons in a LED is

$$n_P = \frac{(\Delta V - IR)I\Delta t}{h\nu}. \tag{A.2}$$

where Δv is the voltage applied to the LED-resistor simple circuit, I is the electric current through the simple circuit, Δt is the time we turn the LED on, h is the Plank constant, ν is the frequency of the emitted light, and R is the value of the resistor connected to the circuit. h, ν, and R are constants.

For the moment, we will assume that only the quantities h and ν have no error, so dh and $d\nu$ are equal to 0 and we only need to consider variations of n_P due to the other parameters, that have an associated error.

So,

$$dn_P = \sqrt{\left(\frac{\partial n_P}{\partial \Delta V}\right)^2 (d\Delta V)^2 + \left(\frac{\partial n_P}{\partial I}\right)^2 (dI)^2 + \left(\frac{\partial n_P}{\partial \Delta t}\right)^2 (d\Delta t)^2 + \left(\frac{\partial n_P}{\partial R}\right)^2 (dR)^2}$$

We derive and simplify the result to obtain

$$dn_P = n_P^2 \left(\frac{d\Delta t}{\Delta t}\right)^2 + \left(\frac{\Delta t}{h\nu}\right)^2 [I^4(dR)^2 + I^2(d\Delta V)^2 + (\Delta V - 2IR)^2(dI)^2] \tag{A.3}$$

Method 2

The expression to estimate the number of produced photons in a LED is

$$n_P = \frac{I\Delta t}{q}. \tag{A.4}$$

where I is the electric current through the simple circuit, Δt is the time we turn on the LED, and q is the charge of an electron. In this case, only q is constant, so we will assume that it has no error. So, dq is equal to 0 and we only need to consider variations of n_P due to the other parameters, that have an associated error.

So,

$$dn_P = \sqrt{\left(\frac{\partial n_P}{\partial I}\right)^2 (dI)^2 + \left(\frac{\partial n_P}{\partial \Delta t}\right)^2 (d\Delta t)^2}$$

We derive and simplify the result to obtain

$$dn_P = n_P^2 \left(\frac{d\Delta t}{\Delta t}\right)^2 + \left(\frac{\Delta t}{q}\right)^2 (dI)^2 \tag{A.5}$$

A.3.1 Error in Average Amplitudes and Normalized graphs

When taking data, the error ϵ depends on the number n of data taken, since

$$\epsilon \sim \frac{1}{\sqrt{n}}.$$

ϵ is a percentage, by fixing it we can determine how much data we need to take to have this associated error. We decided to set ϵ to 10%, so we needed to collect 100 signals to have this error in the measurement.

In summary, the error in the average amplitudes is 10% of the measured value.

If we normalize the bin values A, we must also normalize the error as follows

$$\epsilon_n = \sqrt{A}/n$$

where again, n is the total number of data taken.

A.4 Voltage Sources

Gw Instek GPE-4323 Power supply

This power supply has 4 channels, the first two of which can supply voltage in the range of 0-32 V, the third channel only from 0 to 5 V (approximately), and the fourth from 0 to approximately 15 V. The first two channels can supply a maximum current of 3 A, and the last two can supply a maximum current of 1 A. We show the device in Figure A.2.

Figure A.2: Gw Instek Voltage Supply.

With this device, we can make internal connections between the 4 channels, so we can connect them in series, in parallel, or treat them as independent sources. For the purposes of this project, we will treat all the channels as independent sources and connect all of the negative pins to direct ground from the outside.

For the test we performed with the veto detectors, we operated only channels 1 and 2 between +5 V and +8 V for the PMT voltage input; and channels 3 and 4 were operated only in a range of +0.5 V to + 1.8 V for the control voltage input,which allows us to adjust the detection sensitivity of the PMTs.

This unit was used to operate both veto detectors when we took data with all 3 detectors.
More information can be found on the official website of the manufacturer [40].

B&K Precision 9129B Power Supply

Is a three-output linear programmable DC power supply with isolated outputs that can be set independently or combined in series or parallel to output higher voltage or current. We used only two of the channels independently, one for the input voltage of the sphere's PMT and the other to apply the control voltage of that PMT.

We can use the keyboards to select the voltage we want to apply, so there's no need to turn the knob to increase the applied voltage. The knob can be used to increase the voltage or electric current if we are making small variations of them, otherwise, we can only use the keyboard.

We used the same voltage range in this PMT as in the vetoes for the characterization process.

More information available on the official website [41].

A.5 Measuring and diagnostic instruments

Tektronik DMM-4050 6-1/2 Digital Precision Multímeter

This multimeter has a resolution of 6.5-digits, so it's very accurate when measuring volts, ohms, and amps.

Because of its resolution, we used it to measure amps, it can measure them in a range from 100 μA to 10 A. Let's remember that low amplitude signals in the calibration process are very small, so this is the best device we had to measure these small quantities.

More information can be found in the data sheet of the multimeter [42].

Tektronix TDS2022C Oscilloscope

It's a two-channel oscilloscope that we use to observe the characteristics of the signals produced in the PMT by the passing of cosmic rays. It was used during the test to observe the shape of the signals as well as their amplitudes and durations. It was also used to measure the noise in order to determine the appropriate trigger value to validate the signals as cosmic rays.

In the data sheet of the device, we can read all the specifications of this product [43].

Tektronix TDS5104B Oscilloscope

In Figure A.3 we observe the oscilloscope. This is a 4-channel oscilloscope, which allows us not only to see the characteristics of the PMT signals, but also to perform a coincidence validation for cosmic rays in two or more channels.

Figure A.3: Tektronik Osciloscope.

Due to the number of detectors in our experimental setup, we only used three of the four available channels. We had the ability to monitor the channels individually or all at once, depending on the test we were running.

We could set trigger levels individually and measure different parameters. In our case, we only needed to measure the amplitudes of the signals and the delay times between the channels, which is how we could use the coincidence method. The main advantage of this device is the time resolution, it can measure delay times on the order of picoseconds.

We collected data manually by taking screenshots whenever the implemented condition was met.

For more information, read the datasheet of the device [44].

Functions Generator Tektronix AFG 3101

It's a two-channel function generator that we first used to test the performance of the sphere PMT by turning on the LED at a certain frequency and observing the same

frequency on the signals emitted by the PMT.

We also used this device in the calibration process, where we again turned on the LED at a certain frequency and then measured the average amplitude of the signals. This frequency of the signals was one of the parameters used to determine the relationship between the number of photons and the amplitude of the signals emitted by the PMT.

To know more about the specifications of the handling and care of this device we can consult the data sheet of this model [45].

Bibliography

[1] Félix, Julián. Elemental Particles International Laboratory, DCI of University of Guanajuato. León, Guanajuato, México. Website: http://laboratoriodeparticulaselementales.blogspot.com/

[2] Hess, Victor F. (1936). *Unsolved Problems in Physics: Tasks for the Immediate Future in Cosmic Ray Studies*. Nobel Lecture. NobelPrize.org. Nobel Media AB 2020. Website: https://www.nobelprize.org/prizes/physics/1936/hess/biographical/

[3] Mewaldt, R. A. (1996) *Cosmic Rays*. California Institute of Technology. Recovered from https://www.dartmouth.edu/~sshepherd/research/Shielding/docs/Mewaldt_96.pdf

[4] Beatty, J.J. (Ohio State Univ.), Matthews, J. (Louisiana StateUniv.) & Wakely, S.P. (Univ. of Chicago) (2017). *Cosmic Rays*. Particle Data Group. United States. Website: http://pdg.lbl.gov/2019/reviews/rpp2018-rev-cosmic-rays.pdf

[5] CERN (2020). *Cosmic Rays: particles from outer space*. Website: https://home.cern/science/physics/cosmic-rays-particles-outer-space

[6] Nasa (2017). *Cosmic Rays*.
Website: https://imagine.gsfc.nasa.gov/science/toolbox/cosmic_rays1.html

[7] Oh, Peng (UC Santa Barbara) & Quataert, Eliot (UC Berkeley) (2015). *The Physics and Astrophysics of Cosmic Rays*. Mayacamas. http://w.astro.berkeley.edu/~eliot/cosmic-rays.pdf

[8] Encyclopædia Britannica (2023). *Ionization Energy*. Recovered from: https://www.britannica.com/science/electron-affinity

[9] Lezama, A., Moreno, N., Aguilar, R., Juárez, R., Moreno, A. & Fonseca, M (2019). *Detección y estudio de Rayos cósmicos incidentes en diferentes materiales*. University of Guanajuato. México. Recovered from https://www.youtube.com/watch?v=aOEEzlh1GNI&t=3s

[10] Frass, William (1996). *C4: Particle Physics Major Option. Particle Detectors*. Oxford Physics.
Website: https://www2.physics.ox.ac.uk/sites/default/files/Detectors.pdf

[11] Walther Bothe (1954). *The Coincidence Method*. Nobel Lecture. NobelPrize.org. Nobel Media AB 2020.
Website: https://www.nobelprize.org/prizes/physics/1954/bothe/lecture/

[12] Stacy, J. Gregory & Vestrand, W. Thomas (2003). *Gamma-Ray Astronomy*. Louisiana State University and Southern University, Los Alamos National Laboratory.

[13] Nuclear Power (2022). *Interaction of Gamma Radiation with Matter*. Recovered from https://www.nuclear-power.com/nuclear-power/reactor-physics/interaction-radiation-matter/interaction-gamma-radiation-matter/

[14] Gregersen, Erik (2023). *Compton effect*. Encyclopaedia brittanica. Website: https://www.britannica.com/science/nuclear-reaction

[15] Cherenkov, Pavel A. (1958).*Radiation of Particles Moving at a Velocity Exceeding That of Light, and Some of the Possibilities for Their Use in Experimental Physics*. Nobel Lecture. Recovered from https://www.nobelprize.org/uploads/2018/06/cerenkov-lecture.pdf

[16] Romalis, Michael (2023). *Photoelectric effect*. Princeton University. Recovered from: https://www.princeton.edu/~romalis/PHYS312/Photoelectric.pdf

[17] Chupp, E.L.; Lavakare, P.J. & Sarkady, A.A. (1967). *Limit on the Continuous Solar Flux of the 2.22-MeV Neutron-Proton Capture Gamma Ray*. Department of Physics, University of New Hampshire, Durham, New Hampshire.

[18] Kamioka Observatory. *Super-Kamiokande*. Japan. Official Website: https://www-sk.icrr.u-tokyo.ac.jp/en/sk/

[19] Nasa (2021). *What Is the Solar Cycle?*. United States. Website: https://spaceplace.nasa.gov/solar-cycles/

[20] Nasa (2021). *Sunspots and Solar Flares*. United States. Website: https://spaceplace.nasa.gov/solar-activity/

[21] Space Weather Live (2003 - 2023).*Real-Time Auroral and Solar Activity*. Parsec vzw. Website: https://www.spaceweatherlive.com/

[22] Holly Zell (2017). *Earth's Magnetosphere*. NASA. United States. Website: https://www.nasa.gov/mission_pages/sunearth/multimedia/magnetosphere.html

[23] Breeze, Paul (2017). *Chapter 8 - Nuclear Fission*. Editor(s): Paul Breeze,Nuclear Power, Academic Press, Pages 75-83.

[24] Prince , T. A., Forrest, D. J., Chupp, E.L., Kanbach, G. & Share, G.H. (1983) *The Time Hystory of 2.22 MeV Line Emision in Solar Flares*. California Institute of Technology, University of New Hampshire, Max Planck Institute for extraterrestrial Physics in Germany and Naval Research Laboratory in Washington, DC.

[25] von Rosenvinge, T.T., Ramaty, R. & Reames, D.V. (1981). *Interplanetary particle observations associated with solar flare gamma-ray line emission*. Laboratory for High Energy Astrophysics NASA/Goddart Space Flight Center.

[26] Prince, Thomas A., Ling, James C., Mahoney, William A., Riegler, Guenter R. & Jacobson, Allan S. (1982). *A High-Resolution Measurement of the 2.223 MeV Neutron Capture Line in a Solar Flare.* California Institute of Technology, United States.

[27] Yoshimori, Masato. (1985). *Ratios of the Fluence of 2.22 MeV Gamma-Ray Line to the Fluence of 4.44 MeV Gamma-Ray Line in Solar Flares.* Journal of the Physical Society of Japan Vol. 55, No.2, pp. 487-489. Japan.

[28] Harris, Michael J. & Share, Gerald H. (1991). *A Search for the 2.223 MeV Neutron Capture Gamma-Ray line from the Directions of Cygnus and the Galactic Center*. The Astrophysical Journal, 381:439-443. United States.

[29] Ramaty, Reuven; Mandzhavidze, Natalie; Kozlovsky, Benzion & Murphy, Ronald J. (1995). *Solar Atmospheric Abundances and Energy Content in Flare-Accelerated Ions from Gamma-Ray Spectroscopy*. The Astrophysical Journal, 455: L193–L196. United States.

[30] Troitskaia, E.V. & Kuzhevskij, B.M (1999). *Absorption of 2.22 MeV solar flare gamma-rays and determining of the solar plasma density altitude profile.* Institute of Nuclear Physics, Moscow State University, 119899 Moscow, Russia.

[31] Guessoum, N & Jean, P (2002). *Detectability and characteristics of the 2.223 MeV line emission from nearby X-ray binaries.* A&A 396, 157–169. The European Southern Observatory (ESO).

[32] Chupp, E., Forrest, D., Highbie, P. et al (1973). *Solar Gamma Ray Lines observed during the Solar Activity of August 2 to August 11, 1972*. Nature 241, 333–335. https://doi.org/10.1038/241333a0

[33] Hudson, H.S (1981). *X-ray and Gamma-ray observations of a White Light Flare.* Adv. Space Res. Vol.1, pp. 247—250. Great Britain.

[34] Sketch Up. 3D Design software. Website: https://www.sketchup.com/

[35] Geant4. A Simulation Toolkit. Website: https://geant4.web.cern.ch/

[36] Root. Data Analysis Framework. Website: https://root.cern/

[37] Acrylic (PMMA) sheets purchased from https://www.amazon.com.mx/uxcell-acr%C3%ADlico-transparente-proyectos-manualidades/dp/B092Q2Y598/ref=sr_1_3?__mk_es_MX=%C3%85M%C3%85%C5%BD%C3%95%C3%91&crid=1Q41PVW00YQKR&keywords=uxcell+2+hojas+de+acr%C3%ADlico+fundido+negro&qid=1684705481&sprefix=uxcell+2+hojas+de+acr%C3%ADlico+fundido+negro%2Caps%2C207&sr=8-3

[38] Sensor Technologies (2010). *Photodetector Module P30CW5 series.* United Kingdom. Recovered from http://sens-tech.com/pdf/P30CW5_iss01.pdf

[39] M. Palmer *Propagation of Uncertainty through Mathematical Operations.* MIT. Recovered from http://web.mit.edu/fluids-modules/www/exper_techniques/2.Propagation_of_Uncertaint.pdf

[40] GW Instek (2021). *GPE-x323 Series Multiple Output Linear D.C. Power Supply.* Datasheet recovered from: https://www.gwinstek.com/en-global/products/detail/GPE-X323

[41] BK Precision (2023). *Triple Output Programmable DC Power Supply.* Datasheet recovered from: https://www.testequipmentdepot.com/bk-precision/pdf/xln-series_datasheet.pdf

[42] Tektronix (2011). *Tektronix DMM4050 and DMM4040 Datasheet.* Datasheet recovered from: mouser.mx/datasheet/2/403/Tektronix_DMM4050_and_DMM4040_Digital_Multimeter_D-2308273.pdf

[43] Tektronix (2016). *Digital Storage Oscilloscope TDS2022C.* Datasheet recovered from: https://datasheet.octopart.com/TDS2022C-Tektronix-datasheet-78774299.pdf

[44] Tektronik (2001) *Digital Phosphor Oscilloscopes TDS5000B Series.* Datasheet recovered from https://www.valuetronics.com/pub/media/vti/datasheets/Tektronix%20TDS5032B,%20TDS5034B,%20TDS5052B,%20TDS5054B,%20TDS5104B,%20TDS5054BE.pdf

[45] Tektronix. *Generador de funciones/arbitrarios 3101.* Datasheet recovered from: https://www.cedesa.com.mx/pdf/tektronix/tektronix-AFG3000_series_sheet.pdf

UNIVERSIDAD DE GUANAJUATO

León Guanajuato. Agosto 6, 2023.

DR. DAVID YVES GHISLAIN DELEPINE
DIVISIÓN DE CIENCIAS E INGENIERÍAS
CAMPUS LEÓN, UNIVERSIDAD DE GUANAJUATO
DIRECTOR

Manifiesto que he leído y revisado la tesis de maestría **Detection and Study of the 2.22 MeV Emission Line in the Sun Deuterium Formation Process** realizada bajo mi supervisión, que presenta el C. **Omar Alejandro Lezama Gallegos,** estudiante de maestría en física en esta División de Ciencias e Ingenierías, para optar por el grado de Maestro en Física.

El mencionado trabajo fue realizado dentro del contexto de los proyectos de investigación que desarrollo en el laboratorio de partículas elementales de la Universidad de Guanajuato. El contenido tiene la calidad, profundidad, y originalidad, y representa un avance en el desarrollo del tema a nivel internacional, suficientes para optar por el grado de Maestro en Física.

El trabajo contribuye a entender la planeación, el diseño, la construcción, la caracterización y operación de pequeños detectores de rayos cósmicos; en particular la detección de rayos gammas de 2.22 MeV provenientes del sol, tema de interés internacional.

Sin otro particular,

Atentamente,

Dr. Julián Félix
felix@fisica.ugto.mx
Extensiones 8444, 8449, 8458
ASESOR

León, Guanajuato, 14 de septiembre de 2023

Dr. David Delepine

Director DCI

Presente

Por este conducto le informo que he leído la tesis titulada *"Detection and study of the 2.22 MeV emission line in the Sun deuterium formation process"* que para obtener el grado de Maestro en Física ha formulado el Lic. **Omar Alejandro Lezama Gallegos** bajo la dirección del Dr. Julián Félix Valdez.

En mi opinión, este trabajo reúne las características de calidad y forma para el grado al que se aspira, por lo cual no tengo inconveniente en que se realice la defensa correspondiente.

Sin otro particular, reciba un cordial saludo.

Atentamente

Dr. Mauro Napsuciale Mendivil

Profesor Titular C

Sinodal

c.c.p. archivo

DEPARTAMENTO DE FISICA, DIVISION DE CIENCIAS E INGENIERÍAS, CAMPUS LEÓN
Loma del Bosque 103, Fracc. Lomas del Campestre C.P. 37150 León, Gto., Ap. Postal E-143 C.P. 37000 Tel. (477) 788-5100, Fax: (477) 788-5100 ext. 8410, http://www.fisica.ugto.mx

León, Gto, 18 de septiembre de 2023

Asunto: Carta liberación Omar Alejandro Lezama Gallegos

Dr. David Delepinde
Director de la DCI

Como sinodal del estudiante de la Maestría en Física **Omar Alejandro Lezama Gallegos**, me permito comentar que he leído el manuscrito de su tesis *Detection and Study of the 2.22 MeV Emission Line in the Sun Deuterium Formation Process.*En este trabajo se hace mención sobre la planeación, diseño, construcción y la simulación, de un detector para rayos Gama, y dan evidencia de ello con está tesis.

Considero que el trabajo realizado está al nivel de una Maestría, por lo que me permito recomendar que haga los trámites administrativos correspondientes para que se presente lo más pronto posible.

"LA VERDAD OS HARA LIBRES"

Dr. José Socorro García Díaz
Sinodal

UNIVERSIDAD DE GUANAJUATO

Asunto: ***Carta de Aceptación***
León, Gto, Agosto 15, 2023

Dr. David Yves Ghislain Delepine
División De Ciencias E Ingenierías
Campus León, Universidad De Guanajuato
Director

Comunico que he leído y revisado la tesis de Maestría titulada **“ Detection and Study of the 2.22 MeV Emission Line in the Sun Deuterium Formation Process ”** que presenta el Ing. **Omar Alejandro Lezama Gallegos**, estudiante de la Maestría en Física de la División de Ciencias e Ingenierías, para optar por el grado de Maestro en Física.

El trabajo es de calidad suficiente para optar por el mencionado grado. Por lo anterior, acepto en contenido, forma, y profundidad la mencionada tesis.

Sin otro particular,

Atentamente,

Dr. Edgar Valencia Rodríguez
e.valencia@ugto.mx
Tel. 472 737 3537